Ultrasound contrast agents : from spherical oscillations and buckling dynamics to swimming

Georges Chabouh

THÈSE

Pour obtenir le grade de

DOCTEUR DE L'UNIVERSITÉ GRENOBLE ALPES

Spécialité : MEP : Mécanique des fluides Energétique, Procédés

Arrêté ministériel : 25 mai 2016

Présentée par

Georges CHABOUH

Thèse dirigée par **Gwennou COUPIER**,Chargé de Recherche, Université Grenoble Alpes
et co-encadrée par **Catherine QUILLIET**, Université Grenoble Alpes

préparée au sein du **Laboratoire Interdisciplinaire de Physique** dans **l'École Doctorale I-MEP2 - Ingénierie - Matériaux, Mécanique, Environnement, Energétique, Procédés, Production**

Agents de contraste ultrasonores : des oscillations sphériques et de la dynamique de flambage à la nage

Ultrasound contrast agents: from spherical oscillations and buckling dynamics to swimming

Thèse soutenue publiquement le **9 mars 2022**,
devant le jury composé de :

Monsieur Gwennou COUPIER
CHARGE DE RECHERCHE HDR, CNRS délégation Alpes, Directeur de thèse
Monsieur Sébastien MICHELIN
PROFESSEUR DES UNIVERSITES, Ecole Polytechnique , Rapporteur
Monsieur Hendrick VOS
PROFESSEUR ASSOCIE, Erasmus Universiteit Rotterdam, Rapporteur
Madame Camille DUPRAT
PROFESSEUR DES UNIVERSITES, Ecole Polytechnique, Examinatrice
Monsieur Emmanuel BOSSY
PROFESSEUR DES UNIVERSITES, Université Grenoble Alpes, Examinateur
Monsieur Ayache BOUAKAZ
DIRECTEUR DE RECHERCHE, INSERM délégation Grand Ouest, Président

Abstract

Cleverly engineered microswimmers have been of increasing scientific interest, as they show great promise in various biomedical applications.

In this study, we propose a novel mechanism of propulsion in fluids at the microscale, using a buckling mechanism activated by pressure waves. We considered an in vivo-friendly hollow elastic shell of micrometric size composed of a lipidic membrane enclosing a gas bubble. Such microbubbles are approved for clinical use as diagnostic ultrasound contrast agents (UCAs).

We experimentally investigate the buckling dynamics of microbubbles upon an increase of the external pressure. The effect of the driving frequency is studied as well as that of the size and mechanical properties of the microbubbles. We confront the results to existing theories on buckling dynamics that consider shells made out of an isotropic and incompressible material.

In parallel, we highlight that such hypothesis are too restrictive to account accurately for the dynamics of such UCAs with lipidic shells. Considering these shortcomings, we observe the spherical oscillations of these shells. In this simpler configuration, we derive a new theoretical model that includes the compressibility of the shell and its elastic anisotropy in the radial direction. We thus offer a better description of the spherical oscillations that have been widely studied theoretically and experimentally in the past three decades.

Finally, we evidence, a non-zero displacement upon a complete cycle of deflation and re-inflation of the microbubbles, that includes buckling events.

The proposed propulsion mechanism whose direction is controlled in the shell reference frame can be an answer to the problem of directivity accounted in the acoustic radiation force technique used in ultrasound molecular imaging and drug delivery.

Abstract in French

Les micro-nageurs intelligemment conçus suscitent une attention croissante et se sont révélés très prometteurs pour diverses applications biomédicales.

Dans cette étude, nous proposons un nouveau mécanisme de propulsion dans les fluides à l'échelle microscopique, en utilisant un mécanisme de flambage activé par des ondes de pression. Nous avons considéré une coque élastique creuse de taille micrométrique composée d'une enveloppe lipidique renfermant une bulle de gaz. De telles micro coques sont approuvées pour une utilisation clinique comme agents de contraste ultrasonores (UCA).

Nous étudions, de manière expérimentale, la dynamique de flambage des micro-enveloppes lors d'une augmentation de la pression externe. L'effet de la fréquence d'excitation est étudié, ainsi que celui de la taille et des propriétés mécaniques des micro-coques. Nous confrontons les résultats aux théories existantes sur la dynamique de flambage qui considèrent des coques constituées d'un matériau isotrope et incompressible.

En parallèle, nous mettons en évidence que de telles hypothèses sont trop restrictives pour rendre compte avec précision de la dynamique de tels UCAs à coques lipidiques. Pour ce faire, nous considérons les oscillations sphériques de ces coques. Dans cette configuration plus simple, nous dérivons un nouveau modèle théorique qui inclut la compressibilité de la coque et son anisotropie élastique dans la direction radiale. Nous offrons ainsi une meilleure description des oscillations sphériques qui ont été largement étudiées théoriquement et expérimentalement au cours des trois dernières décennies.

Enfin, nous mettons en évidence un déplacement non nul lors d'un cycle complet de dégonflage et de regonflage des micro-coques, qui inclut des événements de flambage.

Ce mécanisme de propulsion dont la direction est contrôlée dans le cadre de référence de la coque peut être une réponse au problème de la directivité intervenant dans la technique de force de rayonnement acoustique utilisée dans l'imagerie moléculaire ultrasonore et l'administration ciblé de médicaments.

Contents

Appendices

x

x

List of symbols

$\mathbf{A}$	internal relaxation term
A_1	amplitude of first cosine wave
A_2	amplitude of second cosine wave
$\mathbf{B}$	bending energy
d_0	initial thickness
d_{eq}	equivalent thickness
D_0^r	rotational diffusion coefficient
$\mathbf{E}$	Young modulus
E'_r	radial Young modulus
$E'_\mid$	planar Young modulus
$\mathbf{f}$	acoustic frequency
$\mathbf{g}$	acceleration of gravity
G'	3D shear modulus
$\tilde{h}$	projected height
$\mathbf{I}$	light intensity
I_0	Gaussian amplitude
k_B	Boltzmann constant
K'	3D compression modulus
$\mathbf{N}$	number of trajectory
$\mathbf{p}$	pressure
P_G	gas pressure
P_f	fluid pressure
P_{in}	input pressure
P_c	critical buckling pressure
P_{meas}	measured pressure

P_{hydro}	hydrostatic pressure
P_{ac}	acoustic pressure
$\mathbf{r}$	radial distance
R_{10}	internal initial radius
R_{20}	external initial radius
R_{1e}	internal unstrained radius
R_{2e}	external unstrained radius
R_1	internal radius
R_2	external radius
S_p	ad hoc elastic constant
S_f	ad hoc viscous constant
$\mathbf{t}$	time
$\mathbf{T}$	period
T_{pb}	postbuckling period
$\mathbf{u}$	displacement
$\dot{u}$	rate of displacement
U_1	internal radial velocity
U_2	external radial velocity
v_b	sedimentation velocity
v_p	perturbation velocity
v_s	swimming velocity
$\mathbf{V}$	microshell volume
$\hat{V}_S$	non-dimensional microshell volume
V_0	initial microshell volume
V_f	final microshell volume
$\tilde{w}$	projected width
Z_1	internal unstrained constant
Z_2	external unstrained constant
α	corrected gravity angle
γ_1	internal surface tension
γ_2	external surface tension

δ	viscous damping parameter
δz	microshell position
ΔP	internal-external pressure difference
ΔP_{pl}	plateau pressure
ΔV	internal-external volume difference
Δz	pressure controller-sensor height difference
ϵ	strain displacement
ζ	acoustical viscous depth
η	dynamic viscosity
θ	fitting angle
κ	polytropic component
λ	aspect ratio
μ	dynamic viscosity
μ_G	shear viscosity of the shell
μ_K	compression viscosity of the shell
ν	Poisson coefficient
$\nu_\vert$	planar Poisson coefficient
$\nu_{\theta r}$	transverse Poisson coefficient
ξ	amplitude of cosine wave
ρ_f	fluid density
σ	stress tensor
σ'_x	standard deviation of x
σ'_y	standard deviation of y
τ_1	buckling phase period
τ_2	buckled sedimentation phase period
τ_3	debuckling phase period
τ_4	spherical phase period
τ_S	relaxation time of the shell
ϕ	phase shift
χ_{2D}	2D compression modulus
ω_-	non-dimensional spherical pulsation
ω_+	non-dimensional bending pulsation
ω_0	spherical pulsation
ω_1	bending pulsation

List of Figures

List of Tables

Acknowledgements

First and foremost I would like to thank my supervisor Gwennou Coupier for the support throughout these three years, particularly during the ongoing global pandemic of coronavirus disease. I appreciated his supervision that was a great balance between enough freedom to explore my scientific curiosity and enough guidance to keep me on the right track. I would like to acknowledge my co-supervisor Catherine Quilliet for her constant help and friendship, thanks to her scientific eagle view, I have managed to connect all the dots between several parts of my Ph.D. Special thanks to our collaborators at the University of Twente (The Netherlands) for the fabrication of homemade monodisperse microbubbles (Prof. Michel Versluis, Assis.Prof. Tim Segers, Assis. Prof. Guillaume Lajoinie and Ph.D. student Benjamin Van Elburg). Also our collaborators in the University of Freiburg, for the numerical simulations (Prof. Sebastian Aland and Ph.D. student Marcel Mokbel).

I owe a huge debt of thanks is owed to Benjamin Dollet for his kindness and his help in my integration during the first few weeks, and for casting an expert eye over the developments of our new model. I would like to thank Philippe Marmottant for his generosity by allowing me to use his lab to conduct all my experiments and for proving invaluable assistance and advice over the course of the work . Many thanks to Bastien Arnal for the initiation in acoustics and his help in my attempts to develop an acoustical tweezer. I would like to thank Patrice Ballet, for his help when I struggled to build the 90° flipped microscope and to design a microscopic chamber with no leakage. I appreciated the help of Delphine Debarre and Marco Canepari for the help with the microscope. I am very thankful to Jochen Fick to offer me his lab in Institut Néel de Grenoble to develop an optical tweezer and for his help in the tracking algorithm. I appreciated many scientific discussions with Philippe Peyla, Salima Rafai and Chaouqi Misbah in my second team Move. I would like to thank my Ph.D. tutor Irene Wang for listening to all the management difficulties that I had during my PhD and for her tips. Many thanks to Elise Lorenceau and Lionel Bureau for lending me experimental equipment.

I would like to thank, Centre national de la recherche scientifique (CNRS) for a partial funding by choosing our project as PEPS laureate in innovative projects "La Mécanique du Future". Special thanks to the Acoustical Society of America for giving me the student travel subsidy to present the work of this thesis in the ASA 182nd Meeting (May 2022, Denver, USA).

I am thankful to former postdoc in Liphy, Celine Hadji for the help in developing my experimental apparatus. I would like to thank Lucia Stein-Montalvo (University of Princeton) in many important discussions on buckling fundamentals. I am extremely thankful to all my lab mates, specially Winfried Schmidt and Raj Kumar. Finally, I would like to thank Laila Blömer for maintaining my sanity especially in the last writing period.

1 Introduction

Contents

1.1 Background

A series of fluctuations of the pressure field in a medium is the scientific way to define "Sound". When an acoustic wave travels at frequencies ranging between 20 kHz and 20 MHz, it won't be perceivable by the human ear and it will be called an ultrasound wave. Many animals in the nature world, such as bats and dolphins, use ultrasound as a real-time locating system. Inspired by nature, [Richardson, 1913] received two patents within a month after the titanic tragedy, for an echo-ranging system under water to detect large objects. On the foot-steps of animals, humans used echo systems to develop ultrasound (US) imaging. US technique has many advantages: it is non-invasive and inexpensive, available at the point-of-care, and is a safe medical application. It is a widely used imaging technique especially in the prenatal screening of the fetus which is by far the best known application of ultrasound these days.

As for optics, the resolution of ultrasound is limited by its wavelength because of diffraction [Strutt, 1877]. The wavelength is inversely proportional to the frequency

by a factor of $\approx$ 1540 m/s which is the speed of sound in tissues. Hence, an increase of the frequency of the medical probe, one can enhance the resolution. Unfortunately, sound attenuation in human tissue increases exponentially with the frequency [Bamber, 1998] and causes a lower signal on the received part. A common approach to enhance the image is to use bio-compatible microbubbles or ultrasound contrast agents (UCAs).

1.2 Ultrasound Contrast Agents

By serendipity, during an echography of the aorta, [Gramiak and Shah, 1968] saw high peaks on the received signal. In turned out that the presence of air bubbles inside an injected hand-agitated saline solution was responsible for the opacification of the right ventricle. It was indeed, the first ultrasonic image enhancement technique. These air bubbles are known as the first generation of UCAs. As they dissolve rapidly in the liquid, a second generation of UCAs was developed, that are made of air bubbles encapsulated by a thin shell: galactose as in Echovist® (1991) or albumin (a human protein) as in Albunex®(1995) or galactose and palmitic acid as in Levovist®(1995). Finally, the third generation of UCAs includes microbubbles with higher life-time, air being simply replaced by a gas with higher molecular weight, responsible of decreased solubility: SF_6 as in Sonovue® (2001), C_3F_8 as in Definity®(2001) or C_4F_{10} as in Sonazoid®(2007). All of these gases are encapsulated by phospholipids. The resulting shells are known as soft-shell UCAs, while the ones made with polymers are known as hard-shell UCAs.

Commercial UCAs are intravenously administered, and circulate in the blood-stream for several minutes. They demonstrate good safety and are already in widespread clinical use, not only for imaging the heart, but also the liver, kidney and other organs [Barr et al., 2020]. The physics behind the enhancement is the following: UCAs are highly compressible which makes them an efficient acoustic reflectors. They can create a acoustic impedance mismatch between the biological tissues and the fluid [Goldberg, 1997]. The acoustic response of UCAs is dependent on the particle size, shell design, and shape of the applied ultrasound waveform [De Jong et al., 2009]. As it will be discussed in the next chapter, microbubbles resonates in the MHz range. When excited at a centre frequency f_0, microbubbles oscillate non-linearly and generates echoes at different harmonics including subharmonics [Sijl et al., 2011] $f_0/2$, or ultrahamonics $3f_0/2$ and even higher harmonics ($2f_0, 3f_0$...) [Sojahrood et al., 2021]. Using the non-linear nature of UCAs, various contrast-enhanced ultrasound imaging techniques were conducted to enhance the signal coming from UCAs specially in the small capillaries and near the tissues, like harmonic imaging, pulse inversion, amplitude modulation and contrast pulse sequence [Caskey et al., 2011].

Even in presence of such agents, axial and lateral resolutions of ultrasonic devices used in clinical applications are still diffraction-limited. To image beyond this limit, [Desailly et al., 2013, Errico et al., 2015, Couture et al., 2018] discovered a new technique called ultrasound localization microscopy (ULM). It consists in using microbubbles as isolated punctual sources of acoustic echoes. These signals can

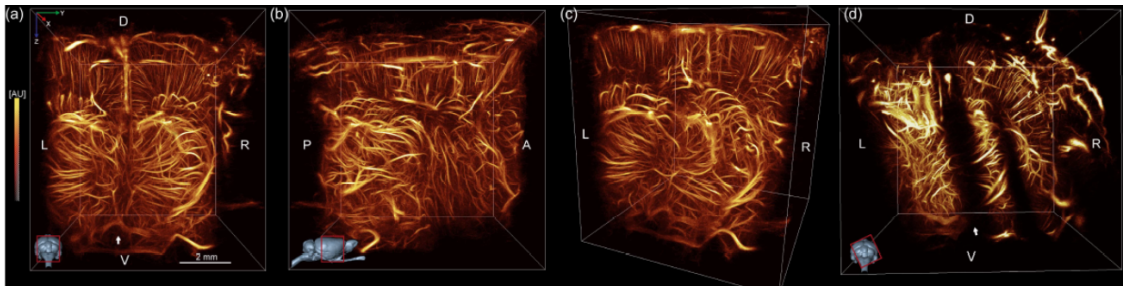

Figure 1.1: (a-b-c) 3D reconstructed microvasculature of the brain: (a) coronal view, (b) sagittal view. Intensity reflects the count of microbubbles. (d) 3D rendering with tilted ultrasound probe on another rat to observe the cortex in the right hemisphere. Images from [Chavignon et al., 2021].

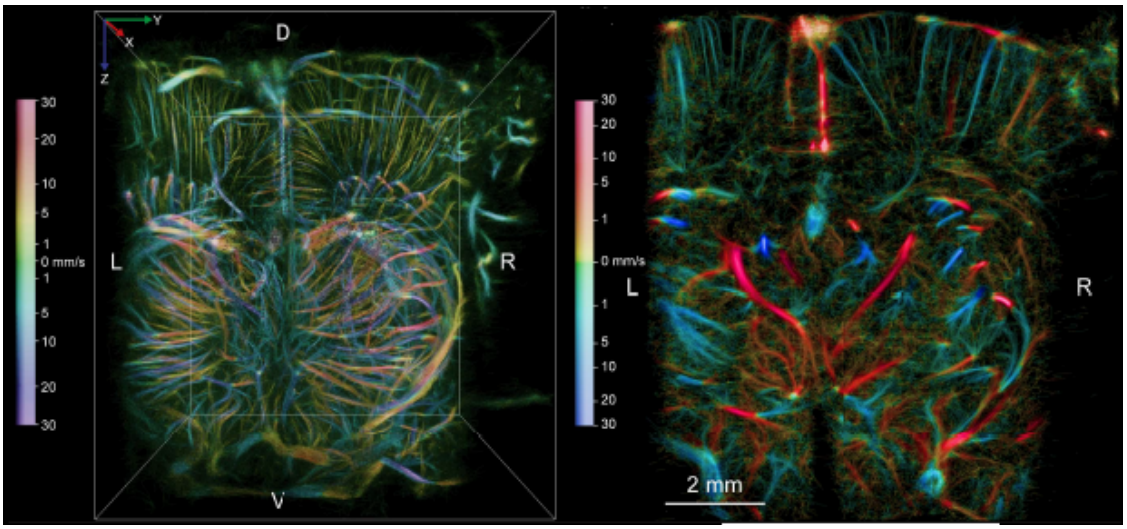

Figure 1.2: Left: 3D rendering of the flow velocity. Right: 600 µm coronal slice at bregma -1.5mm of the hemodynamic volume up to 30 mm/s. Flows are encoded yellow to red (positive) for upward flows, and green to blue (negative) for downward flows. Images from [Chavignon et al., 2021].

thus be localized far beyond the diffraction limit. The reason for crossing this limit is that a microbubble with a diameter ranging from 1 to 10 μm, send signals with a wavelength $\lambda \approx 100$ to 300 times its size. ULM technique is considered to be the ultrasound counterpart of other optical techniques, such as photo-activated localization microscopy (PALM) [Betzig et al., 2006] and stimulated emission depletion (STED) microscopy [Hell and Wichmann, 1994]. Both of them use fluorescent molecules as isolated sources of light. They are known as pioneering methods resulting in the advent of Nobel-prize winning. In a recent work [Chavignon et al., 2021], ULM technique was used together with the ultrafast ultrasound imaging technique [Tanter and Fink, 2014] to provide 3-D images of the microcirculation in a living rat brain (transcranial) (See Fig.1.1). And only 7 minutes acquisition revealed vessels down to 31 µm in diameter with flows from 4.3 mm/s to 28.4 mm/s as shown in Fig.1.2.

While commercial UCAs are quite polydisperse in size, narrowing the size

distribution of UCAs appears then as a way to match better the relatively narrow frequency bandwidth of ultrasonic devices with that of the UCAs, thus leading to better sensitivity of the whole detection process. Recently, monodisperse phospholipid-shelled microbubbles were produced [Segers et al., 2016] and showed 2-3 orders of magnitude higher acoustic sensitivity than that of polydisperse microbubbles in-vitro [Segers et al., 2018] and in-vivo [Helbert et al., 2020]. A cheaper way of production can be done using a 'sonofluidic' device [Carugo et al., 2021]. Finally, a new generation of UCAs is proposed by [Soysal et al., 2021], authors succeeded to prepare monodisperse microbubbles that can be freeze dried without apparent change of size or acoustic behaviour.

1.2.1 Diagnostics and Therapeutic Applications

In the past few decades, the use of microbubbles in medicine went far beyond the imaging. One way of cancer diagnosis can be done using ultrasound diffusion of microbubbles in the vasculature that can distinguish healthy tissues and tumors [Mohanty et al., 2019]. microbubbles can be functionalised by conjugating ligands to their surface that will bind to the target molecules. Targeted UCAs has shown to be very useful in the diagnosis of many life-threatening diseases [van Rooij et al., 2015]. UCAs can also be decorated with antibiotics [Kouijzer et al., 2021] to be used for the destruction of bacterial biofilms, phenomena recently introduced as 'sonobactericide' [Lattwein et al., 2020].

Drug delivery can be conducted mechanically in different modalities [Kooiman et al., 2014, Couture et al., 2014]. The 'traditional' way was pioneered by [Bao et al., 1997] in an in-vitro study termed sonoporation. It was recently translated to a clinical case study on human pancreatic cancer [Kotopoulis et al., 2013]. The idea is to do a co-administration of drugs with microbubbles with a target to produce sonoporation [Kooiman et al., 2011]. Under acoustic excitation, a stable cavitation regime can be reached, where the microbubble volumetrically oscillate and create microstreaming on the surrounding fluid which induces pore formation in the endothelial cells for drug uptake. Although under high acoustic excitations, current UCAs cannot stay long enough on the target and are rapidly destroyed, [Kwan et al., 2015] proposed nanocups that traps air bubble inside to perform stable cavitation for longer time in an in-vivo tumor model. Focused ultrasound drives the microbubbles to a cavitation regime and opens the brain blood barrier (BBB) [Aryal et al., 2014]. BBB opening-induced stable cavitation has also shown great promise after the successful deposit of antibody therapy for breast cancer that has metastized to the brain in a first-in-world clinical trial (Sunnybrook Health Sciences centre, Toronto, Canada) [Meng et al., 2021]. Another way to profit from the BBB opening, is to locate a brain cancer tumor which sends biomarkers into the bloodstream prior to the drug uptake [Pacia et al., 2022]. Fig.1.3 illustrates this novel technique called 'sonobiopsy'.

The second way for drug delivery is the use of UCAs as drug carriers. Either drugs can be linked/adsorbed to the shell, or an additional drug reservoir can be added into the core of the microbubbles [Hernot and Klibanov, 2008]. Followed by

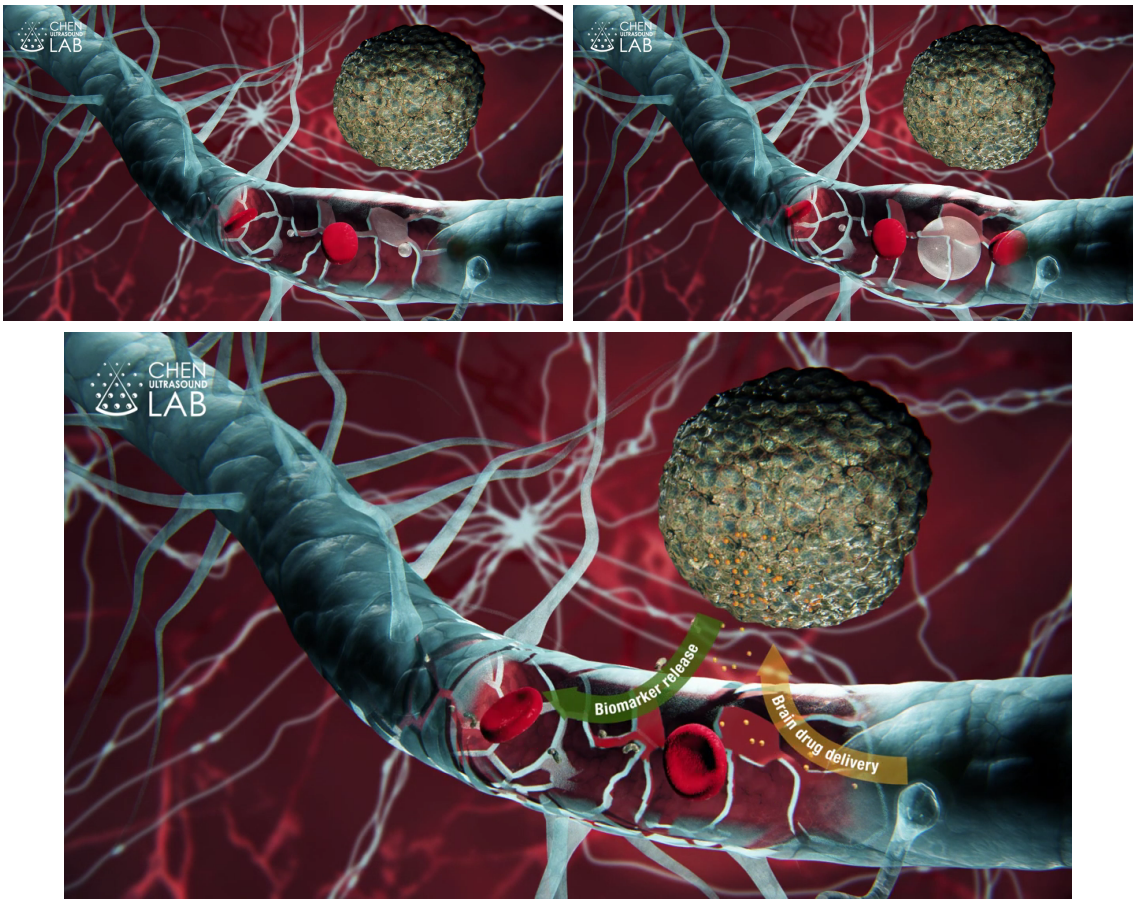

Figure 1.3: Schematic of the sonobiopsy of a brain tumor by BBBO with drug delivery by acoustic cavitation. Image adapted from Hong Chen page on McKelvey School of Engineering (Washington University, St.Louis) website.

higher-intensity ultrasound pulse at the target location,the drug can be released, thereby limiting side effects elsewhere.

A striking new technique for drug delivery used in pancreatic cancer was recently proposed by [Owen et al., 2021]. It relies on the sonodynamic therapy (SDT), defined by the activation of drugs by ultrasound. Authors fabricated oxygen filled microbubbles to fasten the activation process. Drug activation by light was initially created in photodynamic therapy (PDT). It turned out that the principle mechanism underlying the activation in SDT is the same as the one in PDT, in fact, microbubbles under high acoustic cavitation can emit light, phenomenon known as 'sonoluminescence' [Brenner et al., 2002].

1.3 Drug delivery assistance

Despite the huge advances in drug delivery systems and the progress achieved, the circulation of the drug carriers in the bloodstream is still not controlled which hinders

their translation to clinical practice. The absence of specificity and sensitivity with the passive circulating microbubbles jeopardizes the accurate delivery of drugs. Also, the number of microbubbles reaching their targets is low and thus generates weak echoes [Frinking et al., 2012]. One way to improve the number of cargoes is by using magnetic nanoparticles incorporated within the encapsulation coupled to a magnetic system around the organ. [Owen et al., 2015] showed the effectiveness of this approach in vitro. Same effect was shown in an organ transplantation setup by the same group in vivo [Crake et al., 2016].

Soft entities including microbubbles that circulates in confined geometries like capillaries exhibit a lateral migration toward the vessel axis, preventing them to stay in contact with the endothelium [Coupier et al., 2008]. So far, the only developed mechanical approach to assist drug delivery is the acoustic radiation force (ARF) [Rychak et al., 2007] that will be discussed in the following section.

1.3.1 Acoustic radiation force

When an air-bubble in a liquid is subjected to an acoustic pressure field, it can undergo volume pulsations. If the acoustic pressure gradient is non-zero, then it can couple with the bubble oscillations to produce a translational force on the bubble. This is the primary Bjerkness force [Bjerknes, 1906]. If the sound wave driving such motion is the secondary wave emitted by a neighboring pulsating bubble, a mutual interaction comes into effect and two bubbles pulsating in phase attract each other. The average force is then called secondary Bjerknes force.

The first use of ARF for enhancing drug delivery goes back to 1993 [Fowlkes et al., 1993]. Few years later, [Dayton et al., 1997] studied the displacement induced by AFR for different acoustic frequencies and pressures. Authors reported an induced velocity that can reach several tens of millimeters per second. [Vos et al., 2007] pioneered the use of the ARF for accurate measurement of shell elasticity and viscosity. A Doppler based approach to track free floating microbubbles is used and the experimental speed of the microbubbles is compared to theoretical models that couples the volumetric oscillations and the translational-induced AFR to extract the viscoelastic parameters.

Extensive work has been done to understand and optimize the translational motion induced by AFR. [Garbin et al., 2009, Acconcia et al., 2018] checked the effect of the history force, that is considered as an additional drag force, present when the phase velocity of the shell lags the one of the fluid. In contrast to previous studies, where the microbubbles were isolated using optical trap, in this recent study [Supponen et al., 2020], the effect of the size range of free floating microbubbles on their translation motion was discussed. A major drawback of the ARF technique is the directivity imposed by the ultrasound vector field. Unfortunately, a 1-D controlled motion is not enough to manoeuvre the drug carrier in 3-D regions with a complex network as blood stream.

1.4 Swimming in the bloodstream

Creation of microswimmers to perform important biomedical tasks has long been inspired by the science fiction movies, and have already attracted significant attention among researchers [Bunea and Taboryski, 2020, Llacer-Wintle et al., 2021].

If we consider microswimmer administrated intravenously, it will circulate passively in the bloodstream with different velocities ranging from several cm/s in the aorta to several mm/s in capillaries [Errico et al., 2015]. The velocity of the microswimmer v_s has to be in the order of 10 mm/s to swim against capillaries flows. For a microswimmer that propels itself by shape-change, the Reynold number [Reynolds, 1883] associated to the deformation is $Re_s = v_d R/\eta$, with v_d is the deformation speed, η being the kinetic viscosity in order of 10^{-6} m/s for plasma. If the deformation is fast such as Re exceeds unity, the regime is called inertial. On the other hand, if the deformation is slow and Re is less than unity, which is called the Stokes regime. In the former regime, the viscous forces of the fluid dominate the inertia force. In order to have a propulsion in a such regime, the swimmer has to create a time-irreversible displacement usually referred to the 'scallop theorem'. The historic talk of [Purcell, 1977] illustrates well the swimming in the Stokes regime with the metaphor comparison: a microswimmer in blood stream is equivalent to a human swimming in peanut butter.

1.4.1 Swimming by microstreaming

Microstreaming specifically refers to the streaming flow of fluid around an oscillating object such as a gas bubble [Lighthill, 1978]. Whenever the acoustic penetration depth [usually defined as $\zeta = (2\eta/\omega)^{1/2}$ where ω angular driving frequency] is in the same order of magnitude of the bubble radius, the microstreaming effect cannot be neglected. For instance for a bubble or radius 1 μm under acoustic excitation with $\omega = 20$ kHz, the ratio $\zeta/R \sim 4$. Rich variety of streaming patterns can be generated through different shape and volume oscillations modes. [Marmottant and Hilgenfeldt, 2003] studied the fluid streaming pattern around an oscillating bubble and the rupture of a lipid vesicles introduced in the vicinity of the created vortex. An important study to understand more complexed phenomenon as sonoporation. Recently, [Lajoinie et al., 2018] studied experimentally as well as theoretically how microstreaming can enhance drug release from targeted UCAs. Another beneficial way in the use of the microstreaming is the propulsion technique. The first millimetric bubble-swimmer proposed propelled by microstreaming is the "acoustic scallop" [Dijkink et al., 2006]. An air bubble is trapped inside a millimetric tube closed at one end actuated by piezoelectric transducer.

Swimming by micro-streaming requires only that the Reynolds number of the flow exiting the tube be large enough for inertia to be important which is referred to swimming by inertial effect. More recently, based on the same principle, a double-bubble based microswimmer was proposed [Luo and Wu, 2021]. Two air bubbles with different size are trapped into a 3D printed frame to enable steering since each bubble has a different resonance frequency [Minnaert, 1933].

1.4.2 Swimming by buckling

A thin rod under compression is perhaps the easiest example to define buckling. The relevant strain energies of this problem are the stretching energy $\mathcal{U}_s$ that accounts for the compression and the bending energy $\mathcal{U}_b$. The ratio of these two energies $\mathcal{U}_b/\mathcal{U}_s$ scales as: $\sim d^2(k/\epsilon)^2$ where d is the thickness of the rod, k is the average curvature induced by bending (units of reciprocal length) and ϵ is the averaged strain induced by stretching (unitless). As this quantity is very small for thin rods, it means that it is cheaper in terms of energy to bend the rod than to compress it. When speaking about buckling, in a classical definition [Euler, 1744], we imagine a catastrophic failure of a spherical tank full of oil. In the field of structural engineering, design were made to prevent instability events such as buckling, an approach that can be succinctly referred to as 'Buckliphobia' [Reis, 2015]. [Budiansky and Hutchinson, 1979] famously used to say "everyone loves a buckling problem", and this resonates these days with a tremendous amount of papers on how to leverage useful energy from buckling instability [Levin et al., 2016, Yan et al., 2021, Pal et al., 2021].

In the recent years, various buckling based mechanical swimmers have been proposed experimentally as well as numerically. [Chi et al., 2020] developed fast swimming Jelly-fish like soft robot. It consist in attaching swimming paddles on a bilayer elastomeric material that performs a snap-through bi-stability upon pressurization. [Nagarkar et al., 2021] showed that a pneumatically actuated sheet can crawl on land or swim in water by buckling instability.

A proof of concept of the buckling as propulsion mechanism for spherical shells has been introduced in [Djellouli et al., 2017]. An experimental study uses millimetric elastic spherical shell, where air was pumped in-and-out in a symmetrical way. A seeded defect was introduced in the shell to control buckling position and it was attached to a friction-less rail to circumvent its floating due to the buoyancy force. A net positive displacement was evidenced even in the Stokes regime. The deflation speed induced by buckling is very fast, in order of 1 m/s, which gives a deformation related Reynolds number: $Re_d = 100$ such as inertial propulsion is achieved.

1.5 Motivation

The general aim of this thesis is to show that buckling of microbubbles can be a promising propulsion mechanism for various medical applications notably in drug delivery systems. The approach is to study buckling dynamics of microbubbles for different sizes, visco-elastic properties and configurations. To highlight the importance of the composition of the shell, we investigate theoretically in chapter 2, the effect of shell viscoelastic compressibility as well as eventual anisotropy on the spherical oscillations. It is a first step before considering more complexed configuration as the buckled one. Chapter 3 is an experimental study of buckling dynamics of lipid coated commercial and homemade UCAs. We consider different viscoelastic parameters, polydisperse as well as monodisperse, in a near the wall and in a floating configuration. In chapter 4, we study the swimming induced by a full cycle of deflation and re-inflation for different applied pressures and frequencies. In

addition, we study the swimming in a very rare case where a SonoVue® microbubble got glued to two spherical beads and formed an object that sediments with gravity.

Note: Throughout the following thesis, the word 'microbubble' will be used, the reader has to keep in mind that it is implicitly meant the gas bubble and the encapsulating shell. It is an important point to mention, since a gas bubble only cannot buckle but it is the shell that undergoes buckling and debuckling events.

2

Spherical oscillations of UCAs: First investigation of shell compressibility and elastic anisotropy

Contents

2.1 Introduction

The behaviour of UCAs in an ultrasound field has been the subject of investigation for the past three decades. Loads of reviews every year are published to try and summarize the advances of the use of UCAs as well as their theoretical modeling [Helfield, 2019, Versluis et al., 2020, Frinking et al., 2020, Stride et al., 2020]. An accurate understanding of the fundamental behavior of UCAs is still of primordial importance. For instance, in the field of molecular imaging, the goal is to selectively detect and enhance echo signals derived from the molecularly adherent microbubbles via specific ligand–receptor bindings, while suppressing signals derived from the background tissues. An achievement of this goal can lead to fasten the diagnostics of Stroke [Hingot et al., 2020] instead of using current diagnostic imaging as MRI and CT, that require specialized centers and time.

In this theoretical study, we extend the models of ultrasound contrast agent coated microbubbles by accounting for two hitherto overlooked effects: the compressibility of the material constituting the shell, and its possible elastic anisotropy. Such anisotropy has been shown to greatly influence the buckling process of shells ([Munglani et al., 2019, Pitois et al., 2015, Quemeneur et al., 2012]. The importance of anisotropy will be shown in the next chapter where we study experimentally the buckling dynamics. It is therefore important to consider its effect on the spherical oscillations.

2.2 Previous models

Since the early work of [Besant, 1859] who was concerned by the time needed to fill up the empty space of a collapsed bubble and the pressure generated at any point in an incompressible liquid, forced vibrations of bubbles have attracted attention for decades. Giving a simpler derivation of Besant's results, Lord [Rayleigh, 1917] generalized the case to a cavity with nonzero pressure, i.e. to a gas-filled bubble. The surface tension and the viscosity of the surrounding fluid were taken into account (see [Plesset and Prosperetti, 1977] for a review), leading to the famous Rayleigh-Plesset equation.

In order to take into account the shell encapsulating the microbubble, a semi-empirical model was developed [de Jong et al., 1992, De Jong et al., 1994] by way of the introduction of two ad-hoc quantities, S_p and S_f, that account for the effective elastic and dissipative properties of the interface. Assuming a zero-thickness shell, which is motivated by the proximity between the shell thickness and the molecular scale, other models have introduced rheological constants that are explicitly related to the expected properties of the shell material. The first approach by [Chatterjee and Sarkar, 2003] was followed by the models of [Sarkar et al., 2005] and [Marmottant et al., 2005]. In the latter, a non-linear model is proposed, presenting the elasticity of the shell as an effective surface tension. Its linearized form is equivalent to the de Jong model.

In [Church, 1995], a finite thickness shell was considered. It was assumed to be made of a homogeneous, incompressible and isotropic material, that was described

by a Kelvin-Voigt model. This model was linearized relatively to the thickness to radius ratio in [Hoff et al., 2000], giving rise to the Church-Hoff model. In [Morgan et al., 2000], thin-shell UCAs were described by a constant thickness model using bulk elasticity and viscosity.

Following [Marmottant et al., 2005], other nonlinear models have been proposed, with a more complex rheological behavior like strain softening and strain hardening [Tsiglifis and Pelekasis, 2008, Paul et al., 2010], or shear thinning [Doinikov et al., 2009, Li et al., 2013].

2.3 Confrontation with experiments

Vibration experiments on UCAs should *a priori* allow to determine the rheological constants of the material, through the chosen model among those cited above, as long as they are not too numerous. The final goal is usually to choose the best fitting couple of one elastic and one viscous parameter to describe the observed damped signal. This couple is unique for the model selected, for instance, (S_p, S_f) in [de Jong et al., 1992] model, (G_S, μ_S) in [Church, 1995] model, and so on. Note that using finite thickness shell models requires to make assumptions, or additional measurements, to determine the value of the shell thickness. In all models, additional assumptions are generally made in order not to consider the inner gas pressure as an unknown to be determined.

Several techniques can be used to determine the shell oscillations. In [Gorce et al., 2000], a batch of encapsulated microbubbles are insonated at frequencies up to 30 MHz, and the viscoelastic parameters are deduced by measuring the attenuation expression. The spectroscopy approach relies on using a high speed camera to directly measure the radial displacement of the UCAs, which is fitted with the theoretical one [van der Meer et al., 2007]. Light scattering methods were also developed [Tu et al., 2009, Li et al., 2013], where the scattering cross section is related to the resonance frequency containing the viscoelastic properties using the Mie scattering theory. A photoacoustic measurement technique was developed in [Lum et al., 2016]. Readers can refer to [Helfield, 2019] and [Versluis et al., 2020] for recent reviews on linear models theory and experimental measuring methods.

All the existing linear models are virtually the same, with 2D moduli that can be expressed explicitly in terms of 3D moduli and thickness. Tables 2.1-2.5 summarize some experimental estimations of shell properties using the De Jong, Marmottant, Church-Hoff and Sarkar models respectively for different UCAs and using various techniques.

Such experiments may also be used to validate the model that is used to describe the results. This requires to determine by another means the rheological properties of the shell material. Such validations are scarce in the literature, and yield only accurate order of magnitude so far. The atomic force microscopy (AFM) is a direct approach used to estimate UCAs' properties. However, depending on the model used to extract elastic constants from the force-displacement curve of an AFM, very different values can be found [Abou-Saleh et al., 2013, Lytra et al., 2020, Buchner Santos et al., 2012, Shafi et al., 2019]. This makes the validation of

Table 2.1: Shell properties estimations using de Jong model [de Jong et al., 1992]. f and p are the characteristic frequencies and amplitudes of the acoustic waves used to excite the UCAs. S_p and S_f are the elastic and viscous ad-hoc parameters that are introduced in the model. The intervals for the viscoelastic parameters correspond to cases where dependency on the radius was reported.

UCA	R_{20} (μm)	f (MHz)	p (kPa)	S_p (N/m)	S_f (10^{-6} N/m.s)	Method
SonoVue®	$0.6-4.5$	$1-10$	<10	$0.35-2.61$	$0.46-3.42$	Attenuation [Gorce et al., 2000]
Albunex®	$2.5-6$	$0.7-12.5$	not known	8	4	Attenuation [de Jong and Hoff, 1993]
Definity®	$0.5-2.5$	$12-28$	25	1.71	0.015	Attenuation [Goertz et al., 2007]
	$1-3$	$7-15$	25	1.64	0.15	Attenuation [Faez et al., 2011]

spherical oscillation models a tricky task so far. As an example, in [Buchner Santos et al., 2012] and [Lytra et al., 2020], values between 8 and 38 MPa are found for the Young modulus E' of a Definity® UCA probed by an AFM. For an incompressible material the 2D compression modulus χ_{2D} is $E'd_0$, where d_0 is the shell thickness, estimated to be around 5 nm for such UCAs. This leads to $0.04 < \chi_{2D} < 0.2$ N/m, which is not in agreement with the values around 1 N/m found with the de Jong (Table 2.1) or Marmottant (Table 2.2) model. Note however, that static values of the shell may differ considerably from dynamic values measured in the MHz range.

In addition, experimental determinations have lead to unexpected dependencies of the viscoelastic parameters on shell radius, as also shown in Tables 2.1-2.4. [van der Meer et al., 2007] observed a dependence of the shell viscosity on the initial bubble radius using Marmottant model for BR-14®. [Chetty et al., 2008] measured an increase of the shear modulus G' with the radius using Church-Hoff model for Sonovue®. [Tu et al., 2009] and [Li et al., 2013] measured an increase of the elasticity and the viscosity parameters of the shell with the shell radius, using the linearized Marmottant model for Sonovue®. Identical observation where made in [Doinikov et al., 2009] (lipid encapsulated bubbles with De Jong model), [Helfield and Goertz, 2013] (Definity® with Marmottant model), and [Parrales et al., 2014] (home-made monodisperse encapsulated microbubbles with the linearized Marmottant model).

This dependence on radius of the material properties was not substantiated by physical arguments, suggesting that extra modeling was required.

So far, the models have not considered the possible compressibility or anisotropy of the material constituting the shell. The purpose of the present study is to include these effects in the model of bubble oscillations and to quantify their influence on the linearized oscillation properties, i.e. the eigenfrequency and the damping coefficient.

2.4 Model

We consider an encapsulated gas bubble immersed in an incompressible fluid with a density ρ_f and a shear viscosity μ_f. The effect of the liquid compressibility could

Table 2.2: Shell properties estimations using Marmottant model [Marmottant et al., 2005]. f and p are the characteristic frequencies and amplitudes of the acoustic waves used to excite the UCAs. Analysis of experiments through the model allow to determine the 2D compression modulus χ_{2D} and the surface dilatationnal viscosity κ_S. In the linearized version of the model, they are related to the constants introduced by de Jong through $S_p = 2\chi_{2D}$ and $S_f = 12\pi\kappa_S$. The intervals for the viscoelastic parameters correspond to cases where dependency on the radius was reported.

UCA	R_{20} (μm)	f (MHz)	p (kPa)	χ_{2D} (N/m)	κ_S (10^{-8} N/m.s)	Method
SonoVue®	0.975	2.9	130	1	1.5	Spectroscopy [Marmottant et al., 2005]
	$0.8 - 3.25$	2.5	150	$0.024 - 0.87$[1]	$0.1 - 3$	Light scattering [Tu et al., 2009]
	$0.75 - 3.25$	2.5	150	$0.39 - 0.55$	$0.05 - 2$	Light scattering [Tu et al., 2011]
	$0.8 - 3.25$	2.5	150	$0.4 - 0.55$	$0.1 - 3$	Light scattering [Li et al., 2013]
BR14®	1.9	$1.5 - 2.5$	< 40	0.54[1]	2.3	Spectroscopy [van der Meer et al., 2007]

Table 2.3: Follow-up of Table II for reviewer version (Table does not fit on one page).

UCA	R_{20} (μm)	f (MHz)	p (kPa)	χ_{2D} (N/m)	κ_S (10^{-8} N/m.s)	Method
Definity®	$0.72 - 1.4$	1	308	$0.5 - 0.97$	$0.01 - 0.9$	Light scattering [Tu et al., 2011]
	$1.4 - 2.8$	$4 - 13.5$	$6 - 25$	$0.5 - 2.5$	$0.02 - 0.6$	Spectroscopy [Helfield and Goertz, 2013]
Home-made lipid shell	$2.9 - 6.3$	$0.5 - 4$	–	$0.28 - 0.85$	$3 - 6$	Attenuation [Parrales et al., 2014]

be further included as described in the work of [Prosperetti, 1987]. The bubble shell is modeled as a visco-elastic solid of initial thickness d_e. Furthermore, it was shown according to thin shell theory that a shell made of an homogeneous material with Poisson ratio ν may sustain a maximum relative loss of volume

$$(\Delta V/V)_b = \sqrt{\frac{3(1-\nu)}{1+\nu}}\frac{d_0}{R_{20}}, \tag{2.1}$$

before it buckles [Hutchinson, 1967, Quilliet, 2012], where d_0 and R_{20} are the shell thickness and external radius at rest, respectively. The first fraction is of order 1, except for exotic values of ν close to -1. Even for shells happening to be thicker than the commercially available ones, $(\Delta V/V)_b$ is hence reasonably expected not to exceed 1/10. This point, plus recent experimental results having suggested that pressure-volume relationships obtained within the framework of thin shell theory apply also for thick shells [Coupier et al., 2019], indicates that we may safely consider, here and in the following, that linear elasticity framework is sufficient to describe the spherical behaviour of a wide range of UCAs in the unbuckled regime.

Table 2.4: Shell properties estimations using Church-Hoff model [Hoff et al., 2000]. The thickness d_0 is an estimation which is made in each paper. f and p are the characteristic frequencies and amplitudes of the acoustic waves used to excite the UCAs. The intervals for the viscoelastic parameters correspond to cases where dependency on the radius was reported.

UCA	R_{20} (μm)	d_0 (nm)	f (MHz)	p (kPa)	G' (MPa)	μ_G (Pa.s)	Method
SonoVue®	1.78	4	2.5	150	20	0.6	Light scattering [Tu et al., 2009]
	$3-5.5$	2.5	$6.8-7.3$	40	$1.9-105$	1	Microscopy [Chetty et al., 2008]
Sonazoid®	1.6	4	$2-6$	$300-800$	52	0.99	Attenuation [Sarkar et al., 2005]
Optison®	1.5	$5-10$	$3.6-4.3$	100	20.7	1.7	Attenuation [Chatterjee and Sarkar, 2003]

Table 2.5: Shell properties estimations using Sarkar model [Sarkar et al., 2005]. f and p are the characteristic frequencies and amplitudes of the acoustic waves used to excite the UCAs. E^S and κ^S are the surface dilatational elasticity and viscosity respectively introduced in the model.

UCA	R_{20} (μm)	f (MHz)	p (kPa)	E^S (N/m)	κ^S (10^{-8} N/m.s)	Method Method
Sonazoid®	3.2	$2-6$	$200-600$	0.51	1	Attenuation [Sarkar et al., 2005]
Home-made PLA shell	$0.7-1.5$	$2.5-3$	$100-150$	0.02	0.85	Attenuation [Paul et al., 2013]

2.4.1 Quasi-static approximation

In the absence of body forces, the equation of motion in the solid [Landau and Lifschitz, 1986] reads

$$\rho_S \frac{\partial^2 \boldsymbol{u}}{\partial t^2} - \boldsymbol{\nabla} \cdot \boldsymbol{\sigma} = 0, \tag{2.2}$$

where ρ_S is the initial density of the solid, $\boldsymbol{u}$ the displacement field, and $\boldsymbol{\sigma}$ is the Cauchy stress tensor calculated on the actual configuration.

If we consider only elastic contributions to the stress, the dimensional analysis of (2.2) shows that if the parameter $\varepsilon = \omega_0^2 d_e^2 \rho_s / E$, that compares the orders of magnitude of the first and second term in (2.2), is small, then acceleration can be neglected (see e.g. [Langtangen and Pedersen, 2016]). Here E is a typical elastic constant of the material, and ω_0 is the (unknown) shell pulsation. Physically, $\sqrt{\varepsilon}$ is the ratio of the typical time scale $\tau_0 = d_e\sqrt{\rho_s/E}$ needed for an elastic wave to travel across the shell thickness d_e over the time scale ω_0^{-1} of the motion of the boundary. In general, E is not smaller than 100 MPa for a polymeric material where $d_e \sim 100$ nm, but for lipid shells of thickness of order 5 nm which are made of the type of anisotropic material that we treat later on in this chapter, orders of magnitude as low as 100 kPa were proposed for an effective isotropic Young

modulus [Shafi et al., 2019]. Hence, with $\rho_S \sim 1000$ kg/m^3, τ_0 is expected to be smaller than 5×10^{-10} s. This implies that, with ω_0 usually measured or found according to previous models lower than 10 MHz, ε is lower than 10^{-4}.

The acceleration term can therefore be neglected for actual UCAs and will be so in the rest of this chapter. The resolution of Eq.(2.2) under this assumption will serve to determine the boundary conditions for the stress in the fluid, in order to determine its acceleration.

A problem similar to ours has been widely studied recently, that of a bubble oscillating in a liquid confined by a visco-elastic solid [Doinikov et al., 2018, Doinikov and Marmottant, 2018, Vincent and Marmottant, 2017, Wang, 2017]. A simplifying hypothesis, that is used in [Vincent and Marmottant, 2017] and [Wang, 2017] is to consider that the surrounding solid is not accelerated by the pressure waves. Here, we have shown that this hypothesis holds for our problem, due in particular to the thinness of the shells.

Note that the resonance frequency ω_0 is the unknown of this problem, so the validity of the hypothesis has to be checked a posteriori.

2.4.2 Stress-strain relation in the solid

We consider the shell as being made of a transverse isotropic material, i.e. whose properties in the orthoradial plane do not depend on the direction considered but can be different from that in the radial direction. The elastic properties of such a material are characterized by five independent elastic constants. The stress-strain relationship can be written as [Lubarda and Chen, 2008]:

$$\begin{aligned} \sigma_{ij}^{el} &= \lambda\,\epsilon_{kk}\delta_{ij} + 2\mu\,\epsilon_{ij} + 2(\mu_0-\mu)\,(\delta_{i_0i}\epsilon_{i_0j} + \delta_{i_0j}\epsilon_{i_0i}) \\ &+ \alpha\,(\epsilon_{i_0i_0}\delta_{ij} + \delta_{i_0i}\delta_{i_0j}\epsilon_{kk}) + \beta\,\delta_{i_0i}\delta_{i_0j}\epsilon_{i_0i_0}, \end{aligned} \tag{2.3}$$

where ϵ is the strain tensor, λ is the first Lamé coefficient, μ the shear modulus in the plane of isotropy, μ_0 the out-of-plane shear modulus, and α and β two other coefficients. The direction i_0 points the axis of transverse isotropy. For an isotropic material, $\alpha = \beta = 0$ and $\mu_0 = \mu$. For radial displacements, the elastic Cauchy stress tensor has only diagonal components given by

$$\begin{cases} \sigma_{rr}^{el} = (\lambda + 4\mu_0 - 2\mu + 2\alpha + \beta)\,\epsilon_{rr} + 2(\lambda+\alpha)\,\epsilon_{\theta\theta} \\ \sigma_{\theta\theta}^{el} = \sigma_{\phi\phi}^{el} = (\lambda+\alpha)\,\epsilon_{rr} + 2(\lambda+\mu)\,\epsilon_{\theta\theta} \end{cases}, \tag{2.4}$$

with $\epsilon_{rr} = \partial u/\partial r$ and $\epsilon_{\theta\theta} = \epsilon_{\phi\phi} = u/r$, where $u = u(r,t)$ is the Eulerian radial displacement in the shell.

The viscoelastic properties of the material are described by the generalized Kelvin-Voigt model [Thompson and Kelvin, 1865, Voigt, 1892] where the complete strain tensor reads $\boldsymbol{\sigma} = \boldsymbol{\sigma}^{el} + \boldsymbol{\sigma}^{visc}$, where $\boldsymbol{\sigma}^{visc}$ is the viscous stress. For a transverse anisotropic material, integrating a thermodynamical consistent model [Dalenbring, 2002] based on the augmented Hooke's law (AHL) [Dovstam, 1995] in this fluid-structure interaction problem requires finite elements implementation. Another approach may be to consider viscosity effect for only some components of the stress tensor [Lubarda and Asaro, 2014].

We will therefore consider two cases in this study, both going one step further compared to the model by [Church, 1995] that considers an isotropic and incompressible material:

1. A visco-elastic isotropic material, that can be compressible,

2. An anisotropic, purely elastic, material which is transversely isotropic and compressible.

In the case of an isotropic linear material, the elastic stress reads

$$\left\{ \begin{array}{c} \sigma_{rr}^{el} = (K' + \frac{4}{3}G')\,\epsilon_{rr} + 2(K' - \frac{2}{3}G')\,\epsilon_{\theta\theta} \\ \sigma_{\theta\theta}^{el} = \sigma_{\phi\phi}^{el} = (K' - \frac{2}{3}G')\,\epsilon_{rr} + 2(K' + \frac{1}{3}G')\,\epsilon_{\theta\theta} \end{array} \right. , \tag{2.5}$$

where we have introduced the shear modulus $G' = \mu$ and the bulk modulus $K' = \lambda + \frac{2}{3}\mu$. Both are *a-priori* functions of the oscillation frequency, which would call for the resolution of a self-consistency equation when the oscillation frequency will be eventually found as a function of, in particular, these elastic constants. We introduce the Kelvin-Voigt viscous stress $\boldsymbol{\sigma}^{visc}$ whose expression is similar to that of the elastic stress:

$$\left\{ \begin{array}{c} \sigma_{rr}^{visc} = (\mu_K + \frac{4}{3}\mu_G)\,\dot{\epsilon}_{rr} + 2(\mu_K - \frac{2}{3}\mu_G)\,\dot{\epsilon}_{\theta\theta} \\ \sigma_{\theta\theta}^{visc} = \sigma_{\phi\phi}^{visc} = (\mu_K - \frac{2}{3}\mu_G)\,\dot{\epsilon}_{rr} + 2(\mu_K + \frac{1}{3}\mu_G)\,\dot{\epsilon}_{\theta\theta} \end{array} \right. \tag{2.6}$$

The viscosities μ_K and μ_G describe the friction losses due to volume changes and shear, respectively. Little is known, in general, about the values of the loss moduli and, in particular, the "viscous Poisson ratio" whose definition may vary depending on the authors [Lakes and Wineman, 2006]. Its determination generally requires to perform two independent experiments aiming at determining, e.g., a shear loss modulus G'' and a traction loss modulus E'' (see, e.g. [Guillot and Trivett, 2011]). From a modelling perspective, one approach consists in following [Lemaitre and Chaboche, 1994] where it is assumed , with no explicit justification that the ratio μ_K/μ_G is equal to K'/G' which amounts to say that the viscous Poisson ratio that would characterize a ratio of strain rates is equal to the elastic Poisson ratio that characterises the ratio of strains [von Ende et al., 2011, Linn et al., 2013]. Without this assumption, and considering an AHL model as in [Tschoegl et al., 2002], [Pritz, 2009] have proposed bounds for the potential values of the loss moduli for materials with a positive Poisson ratio and a low enough shear loss factor. They show that $2/3 < K''/G'' < 1$ which, for a sinusoidal signal of given pulsation w_0, amounts to the tight inequalities $2/3 < \mu_K/\mu_G < 1$. We discuss these two assumptions in the discussion (Sec. 2.5.6), but one should keep in mind that the difficulties in characterizing accurately two dissipation constants in viscoelastic materials, whose properties are often frequency dependent, must lead to consider the aforementioned relationships as pure hypotheses as for now.

2.5 Isotropic compressible shell

2.5.1 Derivation

Deformation in the solid

The Eulerian radial displacement u within the shell is defined on the actual configuration as the variation from an unstrained position holding no stress within the shell:

$$u(r,t) = r - r_e, \tag{2.7}$$

where r is the actual position of a material particle located at r_e in the reference configuration.

The radial displacement $u(r,t)$ is then calculated by solving Eq. (2.2) in the quasi-static approximation:

$$[\boldsymbol{\nabla} \cdot (\boldsymbol{\sigma}^{el} + \boldsymbol{\sigma}^{visc})]_r = 0. \tag{2.8}$$

The ratio between the viscous and the elastic terms in the above equation is given by the ratio between the loss and storage moduli. Previous experimental studies on existing UCAs show that the ratio between the viscosity and the storage modulus is of order $10^{-8} - 10^{-9}$ s (see values in tables 2.1–2.5) therefore $\omega_0 \tau_S$ is often small, which we will take as a hypothesis in the following.

For an isotropic solid, from $[\boldsymbol{\nabla} \cdot \boldsymbol{\sigma}]_r = \frac{\partial \sigma_{rr}}{\partial r} + \frac{2}{r}(\sigma_{rr} - \sigma_{\theta\theta})$ and using Eqs. (2.5) and (2.6), we are lead to solve:

$$\left(\frac{\partial^2}{\partial r^2} + \frac{2}{r}\frac{\partial}{\partial r} - \frac{2}{r^2}\right)(u + \tau_S \dot{u}) = 0, \tag{2.9}$$

with:

$$\tau_S = \frac{\mu_M}{M'},\ M' = K' + \frac{4}{3}G',\ \mu_M = \mu_K + \frac{4}{3}\mu_G\ . \tag{2.10}$$

The solutions of Eq. (2.9) can be written:

$$u(r,t) = a(t)r + \frac{b(t)}{r^2} + A(r)e^{-t/\tau_S}, \tag{2.11}$$

where the term in $A(r)$ characterizes the internal relaxation within the shell. Note that since $\omega_0 \tau_S$ is small, this term will marginally contribute to the overall response of the shell, and we shall therefore place ourselves in the conditions where it is zero.

The two variables $a(t)$ and $b(t)$ depend on the long time $t \gg \tau_S$ associated with the variations of the boundary conditions. We first express them as functions of $R_1(t)$ and $R_2(t)$, respectively the internal and external radii of the shell, which are our variables of interest. This is achieved thanks to Eq.(2.7), which leads to $u(R_i) = R_i(t) - R_{ie}$, for $i = 1, 2$. R_{1e} and R_{2e} are the values of the radii in the unstrained case, and R_{10} and R_{20} their values at equilibrium in the fluid, which may differ from R_{1e} and R_{2e}, notably because of hydrostatic pressure. We find:

$$a(t) = \frac{R_2^2(t)[R_2(t) - R_{2e}] - R_1^2(t)[R_1(t) - R_{1e}]}{R_2^3(t) - R_1^3(t)}, \tag{2.12}$$

and:

$$b(t) = \frac{R_1^2(t)R_2^2(t)}{R_2^3(t) - R_1^3(t)} \times \{R_2(t)[R_1(t) - R_{1e}] - R_1(t)[R_2(t) - R_{2e}]\}. \tag{2.13}$$

Note that a and b are of order 1 relatively to the displacements at the boundaries, in agreement with the linear elastic theory used here to characterize the deformation tensor.

Velocity in the solid

The velocity field in the shell $\boldsymbol{v}_s$ is the material derivative of the Eulerian displacement $\boldsymbol{u}(r,t)$:

$$\boldsymbol{v}_s(r,t) = \frac{D\boldsymbol{u}}{Dt} = \frac{\partial \boldsymbol{u}}{\partial t} + \boldsymbol{\nabla u} \cdot \boldsymbol{v}_s(r,t). \tag{2.14}$$

For small deformations, $|\boldsymbol{\nabla u}| \ll 1$, the radial component of the velocity v_s thus can be approximated to

$$v_s \approx \frac{\partial u}{\partial t} = \dot{a}r + \frac{\dot{b}}{r^2}, \tag{2.15}$$

where $\dot{a}$ and $\dot{b}$ are the time derivative of the variables a and b. Direct calculation of $\dot{a}$ and $\dot{b}$, shown in Appendix, leads to expressions which violate the kinematic boundary conditions, i.e. $v_s(r = R_1) \neq U_1$ and $v_s(r = R_2) \neq U_2$, where we define $U_1 = \dot{R}_1$ and $U_2 = \dot{R}_2$. However, the deviations from the kinematic boundary conditions remain of order $|R_i - R_{ie}|/R_{ie}$, consistently with the assumption of small deformation and linear elastic behavior. Hence, we can restrict the velocity to its leading order expression, where R_{1e} coincides with R_1 and R_{2e} with R_2. This leads to an expression for v_s that can otherwise be obtained directly from Eq. (2.15) by applying continuity condition at R_1 and R_2:

$$v_s(r,t) \approx a_v r + \frac{b_v}{r^2}, \tag{2.16}$$

where

$$a_v = \frac{R_2^2(t)U_2 - R_1^2(t)U_1}{R_2^3(t) - R_1^3(t)}, \tag{2.17}$$

and

$$b_v = \frac{[R_2(t)U_1 - R_1(t)U_2]R_1^2(t)R_2^2(t)}{R_2^3(t) - R_1^3(t)}. \tag{2.18}$$

The above calculated displacement and velocity generalize the ones found in [Church, 1995] where an incompressible solid material is considered. Such materials are characterised by a traceless deformation tensor:

$$\epsilon_{rr} + \epsilon_{\theta\theta} + \epsilon_{\phi\phi} = 3a = 0, \tag{2.19}$$

leading to the following displacement in the solid:

$$u^{\text{inc}}(r,t) = \frac{R_1^2(t)[R_1(t) - R_{1e}]}{r^2}, \tag{2.20}$$

where we have also used the relation $a = 0$ to reformulate the expression of b. The velocity v_s given by Eq. (2.16) then becomes:

$$v_s^{\text{inc}}(r,t) = \frac{R_1^2(t)U_1}{r^2}. \tag{2.21}$$

Eqs. (2.20) and (2.21) are identical to the ones found in [Church, 1995] where the solid velocity was calculated directly from the law conservation of the mass for an incompressible fluid $\boldsymbol{\nabla} \cdot \boldsymbol{v_s} = 0$, while the displacement was deduced from volume conservation that reads, in the small deformation limit, $\boldsymbol{\nabla} \cdot \boldsymbol{u} = 0$. Note that the two approaches are cross-consistent only in the small deformation framework: then in this case $\boldsymbol{\nabla} \cdot \boldsymbol{u} = 0$, and moreover the $1/r^2$ behaviour of v_s is recovered only if Eq. (2.14) is approximated to Eq. (2.15).

Note finally that the displacement can also be defined on the reference configuration i.e. using Lagrangian formalism without significant difference [Altenbach et al., 2008].

Equations of motion in the liquid

The conservation of mass for an incompressible fluid in a spherical coordinate system gives:

$$\frac{1}{r^2}\frac{\partial}{\partial r}(r^2\mathbf{v}) = 0, \tag{2.22}$$

where $\mathbf{v} = (v_f(r), 0, 0)$ is the radial Eulerian velocity vector in the fluid. For $r = R_2$, $v_f(r = R_2) \equiv U_2$.

The velocity profile of the fluid is then:

$$v_f(r) = \frac{U_2 R_2^2}{r^2}. \tag{2.23}$$

The Navier-Stokes equation for an incompressible fluid and irrotational flow writes [Landau and Lifschitz, 1987]:

$$\rho_f \left(\frac{\partial v_f}{\partial t} + v_f \frac{\partial v_f}{\partial r} \right) = -\frac{\partial P}{\partial r}. \tag{2.24}$$

Integration of Eq. (2.24) between R_2 and $+\infty$, using Eq. (2.23), leads to:

$$\rho_f \left(R_2 \dot{U}_2 + \frac{3}{2} U_2^2 \right) = P_{f|_{r=R_2}} - P_\infty, \tag{2.25}$$

where $P_{f|_{r=R_2}}$ is the pressure in the fluid near the shell boundary, and P_∞ is the sum of the applied acoustic pressure $P_{ac}(t)$ and the ambient pressure P_0.

In addition, conservation of radial momentum at the external surfaces of the shell imposes:

$$-P_G(t) = (\sigma_{rr}^{el} + \sigma_{rr}^{visc})|_{r=R_1} - \frac{2\gamma_1}{R_1}, \tag{2.26}$$

and:

$$(\sigma_{rr}^{el} + \sigma_{rr}^{visc})|_{r=R_2} = -P_f|_{r=R_2} + \sigma_{rr}^{f}|_{r=R_2} - \frac{2\gamma_2}{R_2}, \tag{2.27}$$

where γ_1 and γ_2 are the surface tensions respectively at the internal and external boundaries of the shell, and $P_G(t)$ is the pressure of the gas inside the bubble. We assume the gas to obey a polytropic law, such that $P_G(t) = P_{g_0}(R_{10}/R_1)^{3\kappa}$, where P_{G_0} is the equilibrium gas pressure and κ is the polytropic exponent of the gas. The radial component σ_{rr}^f of the viscous stress equals:

$$\sigma_{rr}^{f} = 2\mu_f \frac{\partial v_f}{\partial r} = -4\mu_f \frac{U_2 R_2^2(t)}{r^3}. \tag{2.28}$$

The normal stresses in the shell are obtained from Eqs. (2.5), (2.6), (2.11) and (2.15), noting that as done for the velocity, the strain rate $\dot{\epsilon}$ is approximated in the linear elasticity limit to: $\dot{\epsilon} = \partial\epsilon/\partial t$, therefore the relation between $\dot{\epsilon}$ and v_s is similar to that between ϵ and u. We have then:

$$\sigma_{rr}^{el} = 3K'a - 4G'\frac{b}{r^3}, \tag{2.29}$$

$$\sigma_{rr}^{visc} = 3\mu_K a_v - 4\mu_G \frac{b_v}{r^3}. \tag{2.30}$$

Inserting (2.29) and (2.30) in the first boundary condition (2.26) leads to a first equation for R_1 and R_2:

$$-P_G + 2\frac{\gamma_1}{R_1} = 3K'a - 4G'\frac{b}{R_1^3} + 3\mu_K a_v - 4\mu_G \frac{b_v}{R_1^3}. \tag{2.31}$$

Replacing a, b, a_v and b_v by their values (2.12), (2.13), (2.17) and (2.18) in the above equation, one eventually gets:

$$\begin{aligned} -P_G + 2\frac{\gamma_1}{R_1} &= 3K'\frac{R_2^2(R_2 - R_{2e}) - R_1^2(R_1 - R_{1e})}{R_2^3 - R_1^3} \\ &- 4G'\frac{[R_2(R_1 - R_{1e}) - R_1(R_2 - R_{2e})]R_2^2}{(R_2^3 - R_1^3)R_1} \\ &+ 3\mu_K \frac{R_2^2 U_2 - R_1^2 U_1}{R_2^3 - R_1^3} - 4\mu_G \frac{(R_2 U_1 - R_1 U_2)\, R_2^2}{(R_2^3 - R_1^3)R_1}. \end{aligned} \tag{2.32}$$

We use the second boundary condition (2.27) to get rid of the unknown fluid pressure in Eq. (2.25), such that:

$$\begin{aligned} \rho_f \left(R_2 \dot{U}_2 + \frac{3}{2} U_2^2 \right) = &-\frac{2\gamma_2}{R_2} - P_\infty - 4\mu_f \frac{U_2}{R_2} \\ &- 3K'a + 4G'\frac{b}{R_2^3} - 3\mu_K a_v + 4\mu_G \frac{b_v}{R_2^3}. \end{aligned} \tag{2.33}$$

This equation can be rewritten in a form that resembles a Rayleigh-Plesset equation by replacing the term $R_2 - R_{2e}$ in a and b thanks to Eq. (2.32) :

$$\begin{aligned}
&\rho_f \left(R_2\dot{U}_2 + \frac{3}{2}U_2^2 \right) = -P_0 - P_{ac}(t) - 2\frac{\gamma_2}{R_2} - 4\mu_f \frac{U_2}{R_2} \\
&+ \left(P_G - 2\frac{\gamma_1}{R_1} \right) \left(1 - \frac{4G'}{3K' + 4G'} \frac{R_2^3 - R_1^3}{R_2^3} \right) \\
&- 4G' \frac{3K'}{3K' + 4G'} \frac{R_2^3 - R_1^3}{R_2^3} \frac{R_1 - R_{1e}}{R_1} \\
&+ 4\frac{U_2}{R_2} \left[\mu_G \left(1 - \frac{4G'}{3K' + 4G'} \right) - \mu_K \frac{3G'}{3K' + 4G'} \right] \\
&- 4\frac{U_1}{R_1} \left[\mu_G \left(1 - \frac{4G'}{3K' + 4G'} \right) - \mu_K \frac{3G'}{3K' + 4G'} \frac{R_1^3}{R_2^3} \right].
\end{aligned} \tag{2.34}$$

In this expression, it is interesting to observe that the elastic contribution of the internal gas is modulated by the intrinsic elastic properties of the shell. This feature will disappear in the incompressible limit. Eq. (2.32) and Eq. (2.34) constitute a system of differential equations for the two unknowns R_1 and R_2. For incompressible materials, the Rayleigh-Plesset equation is sufficient as R_1 and R_2 are simply linked through the incompressibility condition.

2.5.2 Unstrained Vs Initial Radii

As mentioned before, the unstrained radii may be different from the initial radii: $R_{ie} \neq R_{i0}$. The radius R_{ie} is defined by the unstrained state of the shell before it is plunged into the liquid, after what stresses within the shell take place, due to the surface tension at the interfaces, and the internal and external pressures.

Taking Eqs. (2.32) and (2.34) at equilibrium ($U_1 = U_2 = 0$, $P_\infty = P_0$), one can extract the displacements $R_{i0} - R_{ie}$. They can be written $R_{1e} = R_{10}(1 + Z_1)$ and $R_{2e} = R_{20}(1 + Z_2)$, with:

$$\begin{aligned}
Z_1 = &\frac{1}{3K'} \left[\frac{R_{20}^3}{\hat{V}_S} \left(P_0 + \frac{2\gamma_2}{R_{20}} \right) - \frac{R_{10}^3}{\hat{V}_S} \left(P_{G_0} - \frac{2\gamma_1}{R_{10}} \right) \right] \\
&\frac{1}{4G'} \left[\frac{R_{20}^3}{\hat{V}_S} \left(P_0 - P_{G_0} + \frac{2\gamma_2}{R_{20}} + \frac{2\gamma_1}{R_{10}} \right) \right],
\end{aligned} \tag{2.35}$$

$$\begin{aligned}
Z_2 = &\frac{1}{3K'} \left[\frac{R_{20}^3}{\hat{V}_S} \left(P_0 + \frac{2\gamma_2}{R_{20}} \right) - \frac{R_{10}^3}{\hat{V}_S} \left(P_{G_0} - \frac{2\gamma_1}{R_{10}} \right) \right] \\
&\frac{1}{4G'} \left[\frac{R_{10}^3}{\hat{V}_S} \left(P_0 - P_{G_0} + \frac{2\gamma_2}{R_{20}} + \frac{2\gamma_1}{R_{10}} \right) \right],
\end{aligned} \tag{2.36}$$

where $\hat{V}_S = R_{20}^3 - R_{10}^3$.

These formulations highlight the effect of compressibility, which is the same for the two radii.

If the shell is incompressible ($K' \gg P_{G_0}, P_0, \gamma_i/R_{10}$), one has:

$$Z_i^{inc} = \left(P_0 - P_{G_0} + \frac{2\gamma_1}{R_{10}} + \frac{2\gamma_2}{R_{20}}\right) \frac{R_{20}^3 + R_{10}^3 - R_{i0}^3}{4G'\hat{V}_S}, \tag{2.37}$$

which is identical to the expression found in [Church, 1995] when $P_{G_0} = P_0$, which was hypothesized in that paper.

In [Doinikov and Dayton, 2006], where incompressible shells are also considered, the authors find the same relation as Eq. (2.37), which is the first order of their Eq. (33). However in a second step they go further in the calculation using deformation profiles that are valid in the compressible case and find expressions (Eqs. (40) and (41) in their paper) that contradicts our findings, and the ones in [Church, 1995] and in [Sarkar et al., 2005] in that they find the counter-intuitive result that surface tension tends to increase the equilibrium radius. Here, we are satisfied with the observation that an increase of surface tension leads to a shrinkage of the shell. This altogether suggests that care must be taken not to mix expressions from the compressible case with expressions from the incompressible case.

It is worth emphasizing that in the incompressible case, the ratio of the volume in the unstressed configuration to that after the shell is plunged in the fluid, namely $[R_{20}^3(1+Z_2^{inc})^3 - R_{10}^3(1+Z_1^{inc})^3]/\left(R_{20}^3 - R_{10}^3\right)$, is equal to 1 in this model or in the other models [Church, 1995, Khismatullin and Nadim, 2002, Doinikov and Dayton, 2006] only to first order in Z_i^{inc}. This corresponds to the domain of validity of the linear elasticity framework. In the general case, one must therefore restrict the obtained expressions to the first order in Z_i for consistency.

2.5.3 Linear analysis

Assuming a small-amplitude oscillation, linear equations for the R_i can be obtained using the following relations:

$$\begin{aligned} R_1(t) &= R_{10}[1 + x(t)],\ |x(t)| \ll 1; \\ R_2(t) &= R_{20}[1 + y(t)],\ |y(t)| \ll 1; \\ U_1(t) &= R_{10}\dot{x}; \\ U_2(t) &= R_{20}\dot{y}; \end{aligned} \tag{2.38}$$

To the first order in x, y, Z_1 and Z_2, Eq. (2.32) becomes, after using Eqs (2.35) and (2.36):

$$\begin{aligned} -\left(3\kappa P_{G_0} - \frac{2\gamma_1}{R_{10}} + \frac{4G'R_{20}^3 + 3K'R_{10}^3}{R_{20}^3 - R_{10}^3}\right) x \\ + \frac{(4G' + 3K')R_{20}^3}{R_{20}^3 - R_{10}^3} y - \frac{4\mu_G R_{20}^3 + 3\mu_K R_{10}^3}{R_{20}^3 - R_{10}^3}\dot{x} \\ + \frac{(4\mu_G + 3\mu_K)R_{20}^3}{R_{20}^3 - R_{10}^3}\dot{y} = 0. \end{aligned} \tag{2.39}$$

Dividing this equation by K' and taking the limit $K' \to \infty$, one gets $x = yR_{20}^3/R_{10}^3$, which is the relationship obtained for an incompressible material as in [Church,

1995]. Eq. (2.39) is therefore a generalization of this relationship for the case of a viscoelastic compressible material.

Eq. (2.39) together with the linearized Rayleigh-Plesset-like equation obtained from Eq. (2.34) constitutes the following linear system:

$$M\ddot{X} + B\dot{X} + KX = F(t), \tag{2.40}$$

where:

$$X = \begin{pmatrix} x \\ y \end{pmatrix},\ F(t) = \begin{pmatrix} -P_{ac}(t) \\ 0 \end{pmatrix},\ M = \begin{bmatrix} 0 & \rho_f R_{20}^2 \\ 0 & 0 \end{bmatrix}$$

$$B = \begin{bmatrix} b_{11} & b_{12} \\ \frac{-4\mu_G R_{20}^3 - 3\mu_K R_{10}^3}{R_{20}^3 - R_{10}^3} & \frac{(4\mu_G + 3\mu_K) R_{20}^3}{R_{20}^3 - R_{10}^3} \end{bmatrix} \tag{2.41}$$

$$\text{with } b_{11} = 12\frac{K'\mu_G - G'\mu_K \frac{R_{10}^3}{R_{20}^3}}{3K' + 4G'},$$

$$b_{12} = 4\left(\mu_f + 3\frac{K'\mu_G - G'\mu_K}{3K' + 4G'}\right),$$

and

$$K = \begin{bmatrix} k_{11} & \frac{-2\gamma_2}{R_{20}} \\ k_{21} & \frac{(4G' + 3K') R_{20}^3}{R_{20}^3 - R_{10}^3} \end{bmatrix} \tag{2.42}$$

with

$$k_{11} = \left(3\kappa P_{G_0} - \frac{2\gamma_1}{R_{10}}\right)\left(1 - \frac{4G'}{3K' + 4G'}\frac{R_{20}^3 - R_{10}^3}{R_{20}^3}\right) + \frac{12G'K'}{3K' + 4G'}\frac{R_{20}^3 - R_{10}^3}{R_{20}^3},$$

$$k_{21} = -3\kappa P_{G_0} + \frac{2\gamma_1}{R_{10}} - \frac{4G'R_{20}^3 + 3K'R_{10}^3}{R_{20}^3 - R_{10}^3}.$$

The free oscillations of the shells ($P_{ac} = 0$) are described by non-trivial harmonic solutions of the above system $X = X_0 e^{\lambda t}$, where $\lambda = -\delta + i\omega$, that are obtained by setting $\det(\lambda^2 M + \lambda B + K) = 0$. This leads to a polynomial equation of order 3 for λ, which can be solved analytically (yet leading to very long expressions) or numerically. This equation reads

$$c_1\lambda^3 + c_2\lambda^2 + c_3\lambda + c_4 = 0, \tag{2.43}$$

where

$$c_1 = -b_{21}m_{12},\ c_2 = \det[B] - k_{21}m_{12}, \qquad (2.44)$$
$$c_3 = b_{11}k_{22} - b_{12}k_{21} - b_{21}k_{12} + b_{22}k_{11},\ c_4 = \det[K].$$

For sake of comparison with the literature, and making use of the observation that damping coefficient is usually small, we present the leading order approximation and the first-order correction with respect to this damping coefficient in the following. Note that this is a second and independent approximation, based on the usual values of dissipation factors, that is added to that of small deformation.

Leading order approximation

For $B = 0$, Eq. (2.43) becomes $\det[K] - k_{21}m_{12}\lambda^2 = 0$, therefore $\lambda = i\omega_0$ where the undamped resonance frequency ω_0 is given by:

$$\omega_0^2 = \frac{3K' + 4G'}{\rho_f R_{20}^2}$$
$$\left[4G'\,\frac{3K'}{3K'+4G'}\frac{R_{20}^3 - R_{10}^3}{R_{20}^3} + \left(3\kappa P_{G0} - \frac{2\gamma_1}{R_{10}}\right)\left(1 - \frac{4G'}{3K'+4G'}\frac{R_{20}^3 - R_{10}^3}{R_{20}^3}\right)\right]$$
$$\times \left[\left(3\kappa P_{G0} - \frac{2\gamma_1}{R_{10}}\right)\frac{R_{20}^3 - R_{10}^3}{R_{20}^3} + 4G' + 3K'\frac{R_{10}^3}{R_{20}^3}\right]^{-1} - \frac{2\gamma_2}{\rho_f R_{20}^3}. \qquad (2.45)$$

This constitutes the central result of this study. The last term in the above expression is the classical contribution of the surface tension of the outer surface, which acts against an effective mass of fluid whose scale is given by the shell size. By contrast, the contribution of the shell elasticity and of the elastic forces acting on the inner side of the shell (the gas pressure and the surface tension) are strongly coupled. As discussed later on, this coupling disappears in the incompressibility limit. As in the Rayleigh-Plesset expression for a free bubble — $\omega_0^{RP} = \left[\frac{1}{\rho_f R_{20}^2}\left(3\kappa P_{G0} - \frac{2\gamma_1}{R_{20}} - \frac{2\gamma_2}{R_{20}}\right)\right]^{1/2}$, that is recovered here with Eq. (2.45) taken in the limit of vanishing shell volume ($R_{10} \to R_{20}$) — adding surface tension makes the shell pulsation decrease, at *fixed* P_{G0}. In practice, P_{G0} is not known nor measurable and it would be preferable to express the pulsation as a function of the external pressure P_0. While this is easily done for a free bubble, leading to an increase of pulsation with surface tensions, this is more complex in the present situation: P_{G0} and P_0 also couple through the elastic stress within the shell, which depends on the reference configuration (R_{1e}, R_{2e}), which is not known in general.

In this context, measuring oscillation frequency cannot be sufficient to determine the elastic constants of the shell material. Even if surface tensions are assumed to be zero, and considering that the external radius is known, we are left with four unknowns which are the two elastic constants, the internal pressure and the internal radius. This is one more than in Church model and two more than in zero-thickness shell models. Even in these simpler model, and in all cases, one

needs to know more on the fabrication process of the shell to know their stress-free state or to make additional assumptions. In [Church, 1995], it is for instance assumed that permeability of the shell under study allows to consider that $P_{G0} = P_0$, which may be true for thin lipid shells, but not for thicker shells, as pointed out in [Doinikov and Dayton, 2006].

For an incompressible shell, the undamped natural frequency becomes:

$$\omega_0^{inc} = (\rho_S R_{10}^2 \alpha^{inc})^{-1/2} \left(3\kappa P_{G0} - \frac{2\gamma_1}{R_{10}} - \frac{2\gamma_2}{R_{20}} \frac{R_{10}^3}{R_{20}^3} + 4G' \frac{R_{20}^3 - R_{10}^3}{R_{20}^3} \right)^{1/2}, \text{with } \alpha^{inc} = \frac{\rho_f}{\rho_S} \frac{R_{10}}{R_{20}}. \tag{2.46}$$

This differs from the expression proposed in [Church, 1995]:

$$\omega_0^{Ch} = (\rho_S R_{10}^2 \alpha^{Ch})^{-1/2} \left\{ 3\kappa P_{G0} - \frac{2\gamma_1}{R_{10}} - \frac{2\gamma_2}{R_{20}} \frac{R_{10}^3}{R_{20}^3} + 4G' \frac{R_{20}^3 - R_{10}^3}{R_{20}^3} \left[1 + Z_1^{Ch} \left(1 + \frac{3R_{10}^3}{R_{20}^3} \right) \right] \right\}^{1/2}, \tag{2.47}$$

with

$$\alpha^{Ch} = \frac{\rho_f}{\rho_S} \frac{R_{10}}{R_{20}} + 1 - \frac{R_{10}}{R_{20}}. \tag{2.48}$$

A first difference lies in the effective mass characterized by the coefficient α, since we neglected the inertia of the shell. Note that it introduces a correction on ω_0^2 of order d_0/R_{20}, where $d_0 = R_{20} - R_{10}$, that is of at most a few percent for actual UCAs.

The other difference lies in the presence of a Z_1^{Ch} term in [Church, 1995]. This is due to a subtle inconsistency in the linearizing process: as discussed in Sec. 2.5.2, Z_1^{Ch} must be considered as a small parameter in order to keep the validity of linear elasticity framework. It characterizes the difference between the unstrained state and the equilibrium state, the same way as x and y in Eq. 2.38 characterize the difference between the actual and the equilibrium state. Terms like xZ_1 should therefore not be included in the linearized equation, contrary to what is done in [Church, 1995] between his Eqs. (12) and (17). Replacing Z_1^{Ch} by its value in ω_0^{Ch} one gets:

$$\omega_0^{Ch} = (\rho_S R_{10}^2 \alpha^{Ch})^{-1/2} \left[3\kappa P_{G0} + \frac{2\gamma_1}{R_{10}} \frac{3R_{10}^3}{R_{20}^3} + \frac{2\gamma_2}{R_{20}} \left(1 + \frac{2R_{10}^3}{R_{20}^3} \right) + 4G' \left(\frac{R_{20}^3 - R_{10}^3}{R_{20}^3} \right) \right]^{1/2}. \tag{2.49}$$

One can see that the contributions of the surface tension are incorrectly estimated with this contested expression by Church, as this expression does not converge to the Rayleigh-Plesset pulsation ω_0^{RP} in the vanishing volume limit.

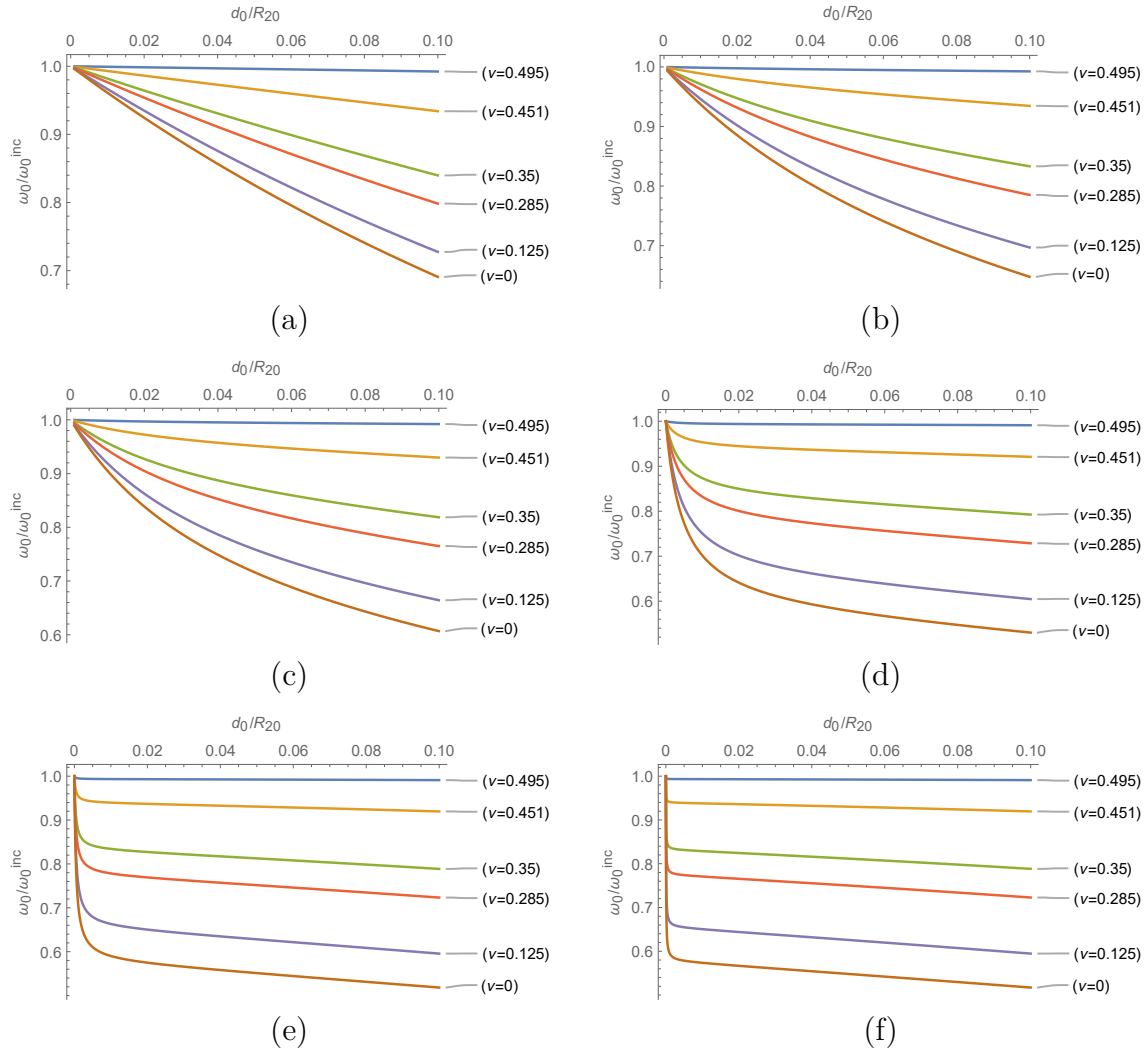

Figure 2.1: Ratio of the undamped resonance frequencies ω_0/ω_0^{inc} as a function of d_0/R_{20}, in the absence of external surface tension. G' is fixed to **a)** $G' = \tilde{P}$, **b)** $G' = 5\,\tilde{P}$, **c)** $G' = 10\,\tilde{P}$, **d)** $G' = 100\,\tilde{P}$, **e)** $G' = 1000\,\tilde{P}$, **f)** $G' = 10^4\,\tilde{P}$. $\tilde{P}$ is $P_{G_0} - \frac{2\gamma_1}{3\kappa R_{10}}$. We varied K' as $100\,G', 10\,G', 3\,G', 2\,G'$, G' and $\frac{2}{3}\,G'$, and the corresponding Poisson ratios $\nu = (3K' - 2G')/(6K' + 2G')$ are shown on each curve. Note that when $\nu = -1$, $\omega_0 \approx 0$.

First order approximation

If Eq. (2.43) is expanded to the first orders in b_{ij} and δ, one gets that $\omega = \omega_0$ and

$$\delta = -\frac{c_3 + b_{21} m_{12} \omega_0^2}{2 k_{21} m_{12}}, \tag{2.50}$$

which can be reformulated as:

$$\delta = \frac{1}{2m_{12}} \left[b_{12} - b_{11} \frac{k_{22}}{k_{21}} + \frac{k_{11}}{k_{21}^2} (b_{21} k_{22} - b_{22} k_{21}) \right]. \tag{2.51}$$

As seen in Eq. (2.40), the first term b_{12} in the above expression represents the damping directly affecting the motion of the external radius of the shell, through

the fluid viscosity and a contribution of the shell viscosity. The second term stems from the damping affecting the motion of the internal radius, which is weighted by the elastic contribution k_{22}/k_{21}. The third term stems from the coupling between dissipation and elastic deformation inside the shell.

For an incompressible shell, the damping ratio δ in Eq. (2.50) simply becomes:

$$\delta^{inc} = 2\frac{(R_{20}^3 - R_{10}^3)\mu_G + R_{10}^3\mu_f}{\rho_S R_{10}^2 R_{20}^3 \alpha^{inc}}. \tag{2.52}$$

In [Church, 1995] it reads:

$$\delta^{Ch} = 2\frac{(R_{20}^3 - R_{10}^3)\mu_G + R_{10}^3\mu_f}{\rho_S R_{10}^2 R_{20}^3 \alpha^{Ch}}. \tag{2.53}$$

As for the pulsation a difference of a few percents remains, which is related to the absence of shell mass in our model.

2.5.4 Effect of compressibility on the resonance frequency

We discuss in this section to which extent the frequency is modified when the material is compressible. We first consider a reference configuration, denoted $\mathcal{R}$, which is considered in [Church, 1995]: $d_0 = 15$ nm, $P_{G_0} = 101.3$ kPa, $\rho_f = 1000$ kg/m^3, $\rho_S = 1100$ kg/m^3, $\mu_f = 0.001$ Pa.s, $G' = 88.8$ MPa, $\gamma_1 = 0.04$ N/m, $\gamma_2 = 0.005$ N/m and $\kappa = 7/5$. For such a shell whose external radius lies in the range $1 - 10\,\mu$m, we find that $0.99 < \omega_0^{inc}/\omega_0^{Ch} < 1$, which indicates that while our model has led us to neglect the inertia of the shell, this assumption will modify the final result by a negligible amount. Note that in this example, since $\gamma_i/R_{i0} \ll G'$, the inaccuracy that we exhibited in the [Church, 1995] model has no quantitative consequence. In the following, we consider ω_0^{inc} as the reference value for discussion.

We now discuss the effect of compressibility together with an evaluation on the impact of the contribution of gas compressibility. For most commercial shells, G' is actually 10 to 1000 times the ambient pressure (see e.g. Table 2.4). Since the G' contribution is weighted by d/R (which is roughly the ratio of the shell material volume over the volume of gas), both contributions are likely to contribute with comparable weight.

As the contribution of the external surface tension is purely additive, for simplicity we set $\gamma_2 = 0$ and consider several values of $\tilde{P} = P_{G_0} - \frac{2\gamma_1}{3\kappa R_{10}}$, that characterizes the contribution of the inner gas to UCA oscillations. In this case, regarding space variables, $R_{20} \times \omega_0$ depends only on d_0/R_{20}.

In Fig. 2.1, the ratio ω_0/ω_0^{inc} is calculated for different values of G' and K', that are set relatively to $\tilde{P}$.

The influence of compressibility is significant: it reduces the resonance frequency, all the more that the relative thickness d_0/R_{20} increases, the Poisson ratio decreases, and the shear modulus increases. In particular, when the bubble radius decreases at fixed thickness, this effect of compressibility will become relatively more important. Compressibility thus introduces a dependency of the frequency on the shell radius

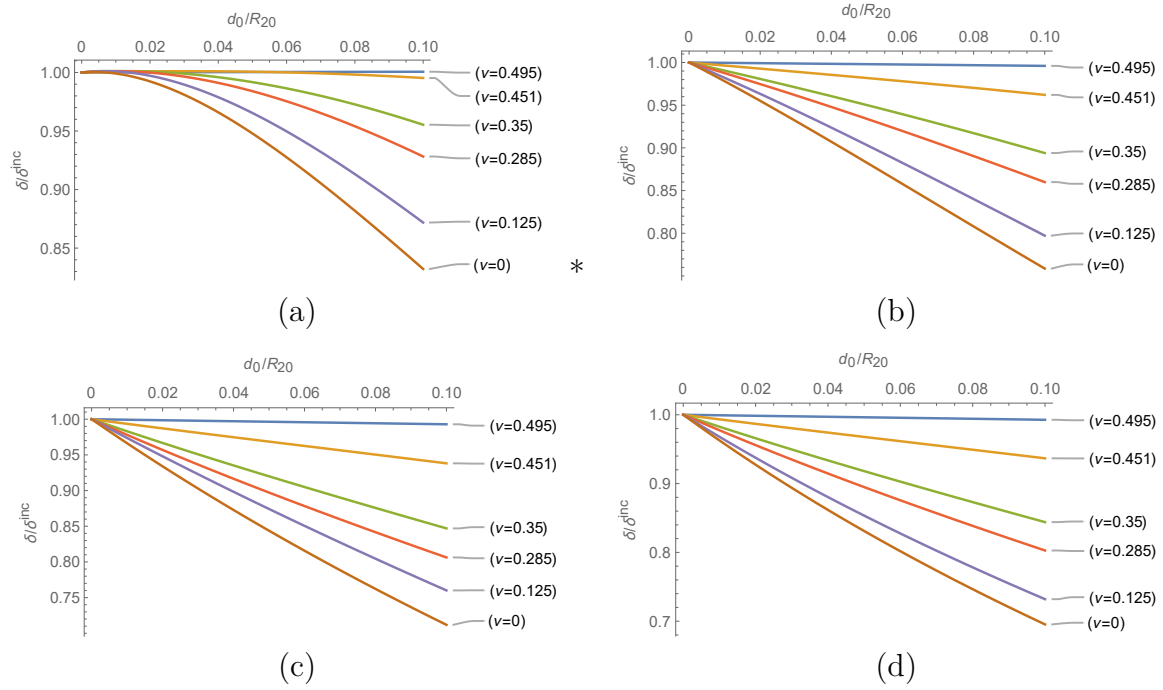

Figure 2.2: Ratio of the damping ratios δ/δ^{inc} as a function of d_0/R_{20}, in the absence of external surface tension. G' is fixed to **a)** $G' = \tilde{P}$, **b)** $G' = 1.5\,\tilde{P}$, **c)** $G' = 4\,\tilde{P}$, **d)** $G' = 5\,\tilde{P}$.$\tilde{P}$ is $P_{G_0} - \frac{2\gamma_1}{3\kappa R_{10}}$. We varied K' as $100\,G', 10\,G', 3\,G', 2\,G'$, G' and $\frac{2}{3}\,G'$, and the corresponding Poisson ratios $\nu = (3K' - 2G')/(6K' + 2G') = (3\mu_K - 2\mu_G)/(6\mu_K + 2\mu_G)$ are shown on each curve. Note that curves do not vary by more than 1% for $G' \geq 5\,\tilde{P}$.

that is more complex than in the incompressible case, where $\omega_0 \propto 1/R_{20}$ in the thin shell limit.

For large values of G', Eq. (2.45) yields, after setting $K' = \frac{2(1+\nu)}{3(1-2\nu)}G' \equiv f(\nu)G'$,

$$\omega^2_{0,G'\gg\hat{P}} = \frac{1}{\rho_f R^2_{20}}\left(4G'\,\frac{R^3_{20} - R^3_{10}}{R^3_{20}}\right)\frac{3f(\nu)}{4 + 3f(\nu)\frac{R^3_{10}}{R^3_{20}}}. \tag{2.54}$$

Then,

$$\left(\frac{\omega_{0,G'\gg\hat{P}}}{\omega^{inc}_{0,G'\gg\hat{P}}}\right)^2 = \frac{3f(\nu)(1-\frac{d_0}{R_{20}})^3}{4 + 3f(\nu)(1-\frac{d_0}{R_{20}})^3} \equiv g(\nu, d_0, R_{20}). \tag{2.55}$$

In the thin shell limit, compressibility leads to a decrease of the pulsation squared by a factor $\sqrt{f(\nu)/[f(\nu) + 4/3]}$.

Eq. (2.54) can also be interpreted from the following practical viewpoint: if one measures a shell pulsation and deduces from this measurement a value G'_0 for the shell, assuming incompressibility, the same measurement can also be obtained with a shell of shear modulus G' and Poisson ratio ν obeying $G'_0 = G'g(\nu, d_0, R_{20})$.

The consequences are two-fold: as $g(\nu, d_0, R_{20})$ is significantly smaller than 1 as soon as $\nu < 1/2$, the existence of unforeseen compressibility will lead to

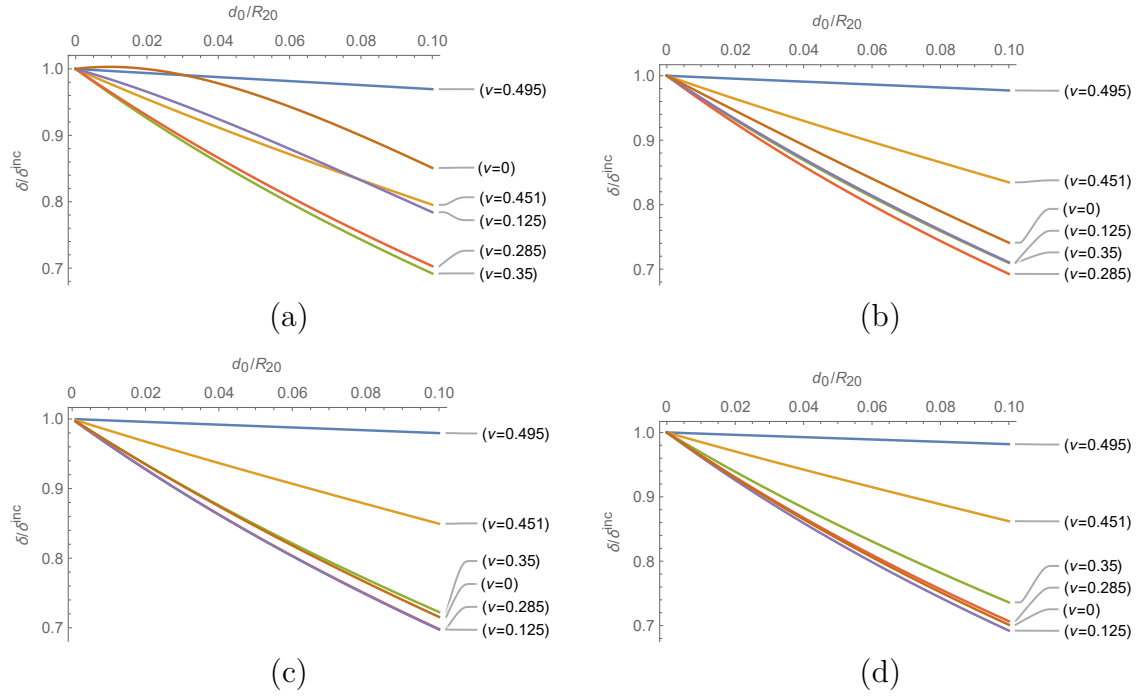

Figure 2.3: Ratio of the damping ratios δ/δ^{inc} as a function of d_0/R_{20}, in the absence of external surface tension. G' is fixed to **a)** $G' = \tilde{P}$, **b)** $G' = 2\,\tilde{P}$, **c)** $G' = 3\,\tilde{P}$, **d)** $G' = 5\,\tilde{P}$. $\tilde{P}$ is $P_{G_0} - \frac{2\gamma_1}{3\kappa R_{10}}$. We varied K' as $100\,G', 10\,G', 3\,G', 2\,G', G'$ and $\frac{2}{3}\,G'$, and the corresponding Poisson ratios $\nu = (3K' - 2G')/(6K' + 2G')$ are shown on each curve.Note that curves do not vary by more than 1% for $G' \geq 5\,\tilde{P}$. In all cases, $\mu_K = 0.7\mu_G$, following [Pritz, 2009].

an underestimation of the shear modulus. For instance, for a shell of estimated thickness 15 nm and external radius 2 μm, if ν happens to be 0.4 instead of 0.5, $g(\nu, d_0, R_{20}) = 0.77$, which means that the shear modulus will be underestimated by 23%. This value reaches 28% if $d_0 = 200$ nm.

Second, as g is an increasing function of R_{20}, using a model for incompressible material can lead to an artificial increase of the (apparent) shear modulus with the radius, a feature regularly pointed out in the literature.

These compressibility effects are more pronounced for thick shells, and we are not aware of oscillation measurements in the literature based on thick shells like polymeric shells. In addition, a more quantitative analysis of the impact of compressibility on the radius dependency of the frequency, by comparison with other suggestions like non-linear effects, requires to know more about the inner pressure inside the considered shells, which depends on their manufacturing process and also potentially on the allotted time for pressure equalization through transmembrane diffusion. This point becomes even more evident in the zero-thickness shell limit that is discussed in the following.

2.5.5 From finite thickness to zero-thickness shell

For vanishing thickness, considering the corresponding limit in our finite thickness model or in that of [Church, 1995] leads to models that can be compared to zero-thickness models. In particular, in [Hoff et al., 2000], the vanishing thickness limit of Church model is considered and the resulting frequency is shown to be similar with that obtained in [de Jong et al., 1992] or in the linearized version of [Marmottant et al., 2005]:

$$\omega_0^{0-\text{thickness}} = (\rho_f R_0^2)^{-1/2} \left(3\kappa P_{G0} + 4\frac{\chi_0}{R_0}\right)^{1/2}, \tag{2.56}$$

where R_0 is the shell radius and χ_0 has the dimension of a surface tension and includes in-plane elasticity effects as well as surface tension effects on both sides of the interface [de Jong et al., 1992, Hoff et al., 2000, Marmottant et al., 2005, Sarkar et al., 2005, van der Meer et al., 2007]. In [Hoff et al., 2000] when surface tension effects are neglected, χ_0 is shown to be equal to $\chi_{2D} = 3G'd_0$, the in-plane surface contraction modulus.

We examine here the small thickness limit of our model. We consider only the incompressibility limit, which is already an interesting source for discussion and allows direct comparison with the actual zero-thickness models.

Keeping only the 0^{th} and 1^{st} orders in d_0/R_{20} in Eq. (2.45), we find the following expansion:

$$\omega_0^{inc} = (\rho_f R_{20}^2)^{-1/2} \left[3\kappa P_{G0} - \frac{2\gamma_1}{R_{20}} - \frac{2\gamma_2}{R_{20}} + \left(12G' + 9\kappa P_{G0} - \frac{8\gamma_1}{R_{20}}\right)\frac{d_0}{R_{20}} + o\left(\frac{d_0}{R_{20}}\right)\right]^{1/2} \tag{2.57}$$

By comparison with Eq. (2.56), this introduces a correction that implies that pressure and inner surface tension have a more complex space-dependency than that proposed in the Church-Hoff model, where the 1^{st} order in d_0/R_{20} was neglected in the inertial term.

We attempt to discuss the implication of our modeling regarding the interpretation of experimental data. Authors generally consider a given experiment for a set of shells of different sizes, which they either watch (measuring thus the radius oscillation [van der Meer et al., 2007, Chetty et al., 2008, Li et al., 2013, Doinikov et al., 2009, Tu et al., 2009]) or listen (measuring thus the acoustic transmission [Parrales et al., 2014]). The obtained curves are then fitted according to the chosen model, which results in the determination of the corresponding elastic modulus for each shell radius. It is then generally observed that this constant increases with the radius, which highlights the limit of the chosen model. Other parameters are generally considered as known but they are not always given by the authors. In particular, the inner pressure P_{G0} is sometimes set to atmospheric pressure with not much justification [van der Meer et al., 2007, Li et al., 2013, Doinikov et al., 2009, Tu et al., 2009] but some authors do not specify their choice [Parrales et al., 2014]. On the other hand, the descriptions of fabrication processes of home-made microbubbles often mention initial gaz pressure larger than 1 bar [Segers et al.,

2016, Parrales et al., 2014], which questions the hypothesis of atmospheric pressure inside the shells. Though diffusion may favor this hypothesis, such a phenomenon will also induce stresses inside the shell reaching its new equilibrium, resulting in uncertainties on the exact state around which the oscillations take place.

Finally, it is generally observed in all papers that while the radius varies by a factor 2 to 3, the corresponding elastic modulus varies by a factor 3 to 4. In [Parrales et al., 2014] this is the case but contrary to most other papers where only the values of the elastic constants are given, the measured frequencies are also mentioned. We therefore use these raw data to make the following comments. In Fig. 2.4, the pulsations found in the experiments are plotted as a function of shell radius. Those shells are lipidic shells, therefore the small-thickness limit holds. The fit of their data by the usual zero-thickness law (Eq. 2.56), assuming $P_{G0} = 1$ bar and $\kappa = 1.4$, is not that good, which illustrates the conclusions of the authors who, considering each radius separately, showed that the elastic modulus must be an increasing function of the radius. We note however that the fit yields $\chi_0 = 0.21$ N/m, which is smaller than all the values reported by the author for the different shell radii, which questions the (implicit) choice of inner pressure or of polytropic constant they made. Interestingly, letting P_{G0} free leads to a better fit, with $P_{G0} = 1.6$ bar. This shows the importance of the knowledge of the inner pressure or, equivalently, of the polytropic coefficient that depends on the chosen gas and on the details of the thermodynamics process, as discussed in [Parrales et al., 2014].

In the expression for the zero-thickness limit that we established (Eq. 2.57), we show that the contribution of pressure is more complex and that it is important to decouple, in the elastic contribution of the interface, bulk effects from surface tension effects: they do not sum up in a simple χ_0 parameter. Using this expression we find an even better fit for the data of [Parrales et al., 2014], illustrating thus the complex interplay between all the parameters of these models. Note that we do not claim here that the parameters we find are those that actually characterize the considered shell. Our discussion simply highlights the need for a good knowledge of a maximum of parameters, if one wishes to extract one unknown parameter from the sole measurement of oscillation frequencies.

2.5.6 Effect of compressibility on the damping

Reminder: our model assumes that $\tau_S = \mu_M/M'$ is much smaller than ω_0^{-1}. In the following examples, we checked that $\tau_S\omega_0$ is always lower than 0.01. We set here the fluid viscosity $\mu_f = 0.001$ Pa.s and the shear viscosity $\mu_G = 0.002$ Pa.s.

As for the discussion on pulsation, we set $\gamma_2 = 0$ and consider several values of $\tilde{P} = P_{G_0} - \frac{2\gamma_1}{3\kappa R_{10}}$. In Fig. 2.2 we show the ratio of the damping constants δ/δ^{inc} under the hypothesis that μ_K varies with μ_G the same way K' varies with G' that is, the viscous and elastic Poisson ratio are equal [Lemaitre and Chaboche, 1994]. In Fig. 2.3 μ_K is chosen to be equal to $0.7\mu_G$ following [Pritz, 2009], where it is shown that $2/3 < \mu_K/\mu_G < 1$ for thermodynamic consistency.

Compressibility has the effect to make the damping constant decrease.As for the elastic constant determined through the frequency, this may lead to an

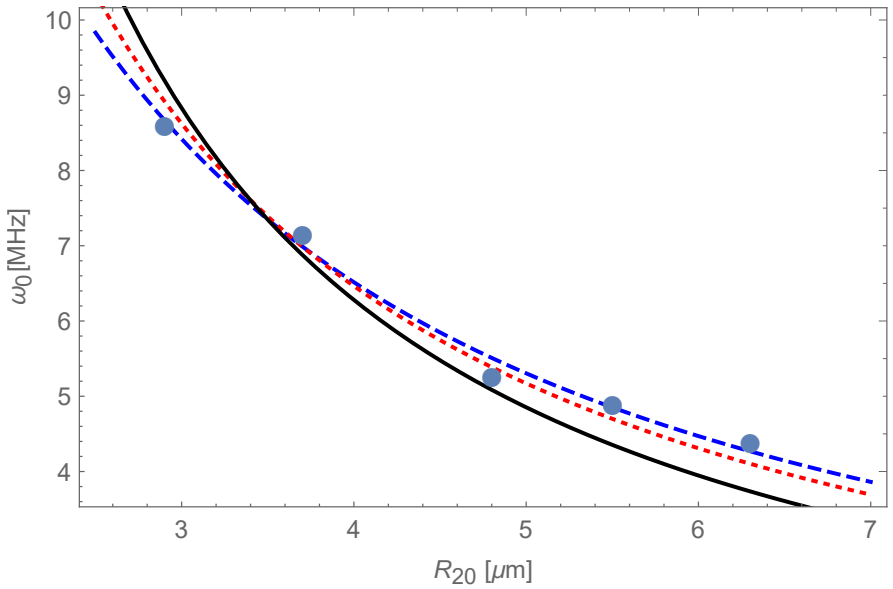

Figure 2.4: Dots: experimental pulsations found in [Parrales et al., 2014] as a function of shell radius. Full black line: fit with Eq. (2.56) with fixed inner pressure $P_{G0} = 1$ bar and χ_0 as a free parameter. Red dotted line: fit with the same equation but the pressure is also a free parameter. Blue dashed line: fit with Eq. (2.57) with also the surface tension being a free parameter. Using Eq. (2.57) allows to recover the full spatial dependency of the data, with a $1/R_0$ and a $1/R_0^{3/2}$ contribution.

underestimation of the shear viscosity if an incompressible model is used. For large values of G' and $K' = G'f(\nu)$ compared to $\tilde{P}$, as for the frequencies, the damping depends only on elastic properties through the Poisson ratio, as can be seen through Eqs. (2.41) and (2.42) taken in the limit $G', K' \gg \tilde{P}$. In practice, as seen in Figs. 2.2 and 2.3, this limit is reached as soon as $G' > 5\tilde{P}$, which is generally the case for actual commercial UCAs. Interestingly, the choice of the model for the viscous Poisson ratio has little impact on the final results: for high values of K', μ_K is not expected to contribute much for both models as its contribution vanishes in the incompressibility limit (see Eq. (2.52)), and for values of K' comparable G', μ_K is close to μ_G in both models. If the [Pritz, 2009] model is assumed though, the coupling between elastic and viscous terms is such that the damping is not a monotonous function of the Poisson ratio ν.

2.6 Transverse isotropic elastic shell

We now examine the effect of anisotropy in the properties of a purely elastic material. We reformulate Eq. (2.4) using elastic constants corresponding to

standard deformations [Lempriere, 1968, Itskov and Aksel, 2002]:

$$\left\{\begin{array}{c} \sigma_{rr}^{el} = \frac{(1-\nu_{\|})E'_r}{1-\nu_{\|}-2\frac{E'_{\|}}{E'_r}\nu_{\theta r}^2}\epsilon_{rr} + \frac{2\nu_{\theta r}E'_{\|}}{1-\nu_{\|}-2\frac{E'_{\|}}{E'_r}\nu_{\theta r}^2}\epsilon_{\theta\theta} \\ \sigma_{\theta\theta}^{el} = \sigma_{\phi\phi}^{el} = \frac{\nu_{\theta r}E'_{\|}}{1-\nu_{\|}-2\frac{E'_{\|}}{E'_r}\nu_{\theta r}^2}\epsilon_{rr} + \frac{E'_{\|}}{1-\nu_{\|}-2\frac{E'_{\|}}{E'_r}\nu_{\theta r}^2}\epsilon_{\theta\theta} \end{array}\right. , \tag{2.58}$$

where E'_r is the Young modulus for traction in the radial direction while $E'_{\|}$ is the Young modulus in the orthoradial plane. $\nu_{\|}$ is the Poisson ratio in this same plane, and $\nu_{\theta r}$ the Poisson ratio governing deformations in the orthoradial plane when there is a radial load [1].

Thermodynamical consistency imposes [Lempriere, 1968]:

$$\begin{array}{c} -1 \leq \nu_{\|} \leq 1 \\ -\sqrt{E'_r/E'_{\|}} \leq \nu_{\theta r} \leq \sqrt{E'_r/E'_{\|}} \\ \nu_{\|} \leq 1 - 2\nu_{\theta r}^2\frac{E'_{\|}}{E'_r} \end{array} . \tag{2.59}$$

For an isotropic material of Poisson ratio ν, these inequalities reduce to $-1 \leq \nu \leq 1/2$. The case $\nu = 1/2$ corresponds to incompressible material as considered in [Church, 1995].

2.6.1 Derivation

Displacement within the shell

Following the same steps as in Sec. 2.5.1, the displacement now obeys the following equation:

$$\frac{d^2u}{dr^2} + \frac{2}{r}\frac{du}{dr} - \frac{2ku}{r^2} = 0, \tag{2.60}$$

with:

$$k = \frac{E'_{\|}(1-\nu_{\theta r})}{E'_r(1-\nu_{\|})}, \tag{2.61}$$

which is the equivalent of Eq. (2.9) for this purely elastic case.

The solutions of Eq. (2.60) have the form

$$u^{Tr}(r) = a^{Tr}r^{\beta_+} + b^{Tr}r^{\beta_-}, \tag{2.62}$$

with $\beta_{\pm} = \frac{1}{2}(-1 \pm \sqrt{1+8k})$. Note that by virtue of Eqs. (2.59), it can be shown that $k \geq -1/8$ whatever the material properties and the exponents $\beta_{\pm}$ are real. The isotropic case corresponds to $k = 1$ then $\beta_- = -2$ and $\beta_+ = 1$. The variables a_T and b_T are related to the boundary conditions thanks to Eq. (2.7):

$$a^{Tr} = \frac{(R_2 - R_{2e})R_{10}^{\beta_-} - (R_1 - R_{1e})R_{20}^{\beta_-}}{R_{10}^{\beta_-}R_{20}^{\beta_+} - R_{10}^{\beta_+}R_{20}^{\beta_-}}, \tag{2.63}$$

[1] Note that $\nu_{r\theta}$ is used by some authors instead of $\nu_{\theta r}$ [Lempriere, 1968].

and

$$b^{Tr} = \frac{(R_1 - R_{1e})R_{20}^{\beta_+} - (R_2 - R_{2e})R_{10}^{\beta_+}}{R_{10}^{\beta_-}R_{20}^{\beta_+} - R_{10}^{\beta_+}R_{20}^{\beta_-}}. \tag{2.64}$$

The Rayleigh-Plesset-like equation can be derived following the same steps as in Sec. 2.5.1. For the sake of simplicity we calculate directly the resonance frequency in the following section.

2.6.2 Resonance frequency

Following the same steps as in Sec. 2.5.3, one gets the following system:

$$M\ddot{X} + KX = F(t), \tag{2.65}$$

where

$$X = \begin{pmatrix} x \\ y \end{pmatrix}, F(t) = \begin{pmatrix} -P_{ac}(t) \\ 0 \end{pmatrix}, M = \begin{bmatrix} 0 & \rho_f R_{20}^2 \\ 0 & 0 \end{bmatrix},$$

and

$$K^{Tr} = \begin{bmatrix} k_{11}^{Tr} & \frac{-2\gamma_2}{R_{20}} \\ k_{21}^{Tr} & k_{22}^{Tr} \end{bmatrix}, \text{where}$$

$$\begin{aligned} k_{11}^{Tr} &= \left(3\kappa P_{G_0} - \frac{2\gamma_1}{R_{10}}\right) \\ &\times \left\{1 - 2\frac{(R_{20}^{\beta_+-1} - R_{10}^{\beta_+-1})(\beta_+ - 1)^{-1}R_{10}^{\beta_-}A_+ - (R_{20}^{\beta_--1} - R_{10}^{\beta_--1})(\beta_- - 1)^{-1}R_{10}^{\beta_+}A_-}{E_r'(1-\nu_\parallel)(\beta_+ - \beta_-)}\right\} \\ &+ \frac{2(R_{20}^{\beta_+-1} - R_{10}^{\beta_+-1})(\beta_+ - 1)^{-1}R_{10}^{\beta_-}A_+[E_r'(1-\nu_\parallel)\beta_- + 2\nu_{\theta r}E_\parallel']}{\left(1 - \nu_\parallel - 2\frac{E_\parallel'}{E_r'}\nu_{\theta r}^2\right)E_r'(1-\nu_\parallel)(\beta_+ - \beta_-)} \\ &- \frac{2(R_{20}^{\beta_--1} - R_{10}^{\beta_--1})(\beta_- - 1)^{-1}R_{10}^{\beta_+}A_-[E_r'(1-\nu_\parallel)\beta_+ + 2\nu_{\theta r}E_\parallel']}{\left(1 - \nu_\parallel - 2\frac{E_\parallel'}{E_r'}\nu_{\theta r}^2\right)E_r'(1-\nu_\parallel)(\beta_+ - \beta_-)}, \end{aligned} \tag{2.66}$$

with:

$$A_+ = \beta^+(1-\nu_\parallel)E_r' - [1 - (2-\beta^+)\nu_{\theta r}]E_\parallel', \tag{2.67}$$

$$A_- = \beta^-(1-\nu_\parallel)E_r' - [1 - (2-\beta^-)\nu_{\theta r}]E_\parallel', \tag{2.68}$$

and:

$$\begin{aligned} k_{21}^{Tr} &= -3\kappa P_{G_0} + \frac{2\gamma_1}{R_{10}} + \frac{R_{20}^{\beta_+}R_{10}^{\beta_-}[E_r'(1-\nu_\parallel)\beta_- + 2\nu_{\theta r}E_\parallel']}{\left(1 - \nu_\parallel - 2\frac{E_\parallel'}{E_r'}\nu_{\theta r}^2\right)(R_{10}^{\beta_-}R_{20}^{\beta_+} - R_{10}^{\beta_+}R_{20}^{\beta_-})} \\ &- \frac{R_{20}^{\beta_-}R_{10}^{\beta_+}[E_r'(1-\nu_\parallel)\beta_+ + 2\nu_{\theta r}E_\parallel']}{\left(1 - \nu_\parallel - 2\frac{E_\parallel'}{E_r'}\nu_{\theta r}^2\right)(R_{10}^{\beta_-}R_{20}^{\beta_+} - R_{10}^{\beta_+}R_{20}^{\beta_-})}, \end{aligned} \tag{2.68}$$

$$k_{22}^{Tr} = \frac{R_{20}R_{10}^{\beta_-+\beta_+-1}\left[E'_r(1-\nu_\parallel)(\beta_+-\beta_-)\right]}{\left(1-\nu_\parallel-2\frac{E'_\parallel}{E'_r}\nu_{\theta r}^2\right)\left(R_{10}^{\beta_-}R_{20}^{\beta_+}-R_{10}^{\beta_+}R_{20}^{\beta_-}\right)}. \quad (2.69)$$

Then, the undamped resonance frequency is:

$$\omega_0^{Tr} = \left(\frac{\det[K^{Tr}]}{m_{12}k_{21}^{Tr}}\right)^{1/2}. \quad (2.70)$$

2.6.3 Effect of anisotropy

In what follows, the couple ($E' = 2G'(1+\nu)$,ν) will be used to describe the elastic properties of an isotropic solid for the sake of comparison with the elastic properties of a transversely isotropic material.

We first discuss what is the impact of anisotropy keeping the material incompressible. In such a situation, it is shown in [Itskov and Aksel, 2002] that $\nu_{\theta r} = 1/2$ while $\nu_\parallel = 1 - \frac{E'_\parallel}{2E'_r}$. Thermodynamics constraints (Eq. (2.59)) then impose $E'_r > E'_\parallel/4$.

We remark that Eq. (2.61) becomes $k = 1$ that is, the deformation function is the same as in the isotropic case. Second, the terms in the K^{Tr} matrix implying the shell elastic constants are all proportional to E'_r and do not depend on $E'_\parallel$. We conclude that incompressible shells oscillate exactly the same way whatever the value of their in-plane Young modulus that is, they oscillate like isotropic incompressible shells of Young modulus E'_r

For anisotropic compressible material, in general, hydrostatic stress does not necessarily induces a uniform dilatation in the three directions. It is interesting for comparison with the isotropic case to consider the situation where this is true. In such a situation of isotropic volumetric response, a bulk modulus can be defined as a material constant [Itskov and Aksel, 2002]. It is equal to $\varkappa = E'_r/[3(1-2\nu_{\theta r})]$. In addition, it can be shown that $\nu_\parallel$ is given by $1-\frac{E'_\parallel}{2}\left(\frac{1}{E'_r}+\frac{1}{3\varkappa}\right)$; the material properties are thus described, for the radial motion considered here, by 3 independent variables (e.g. $\varkappa$, E'_r and $E'_\parallel$) instead of 4 in the general case and 2 in the incompressible case. In this case also, the pulsation is that of the isotropic material of moduli $K' = \varkappa$ and $E' = E'_r$, though the deformation inside the shell is not the same: in Eq. (2.61), k is independent from $E'_\parallel$ (but not necessarily equal to 1) and because $\nu_\parallel$ appears only under the pattern $1-\nu_\parallel$ in K^{Tr}, it can be easily seen that the contribution of $E'_\parallel$ vanishes.

Finally, in Fig. 2.5, we consider a general (arbitrary) case, based on the test case the configuration $\mathcal{R}$ as it refers to a lipidic shell, which we may expect to exhibit transverse anisotropic properties. We have fixed $\nu_\parallel = \nu_{\theta r} = 0.35$ and varied $E'_\parallel$ as a function of E'_r, within the bounds allowed by thermodynamics. Here, $E'_\parallel$ also influences the frequency, which increases as $E'_\parallel$ increases.

In all cases, as for the isotropic case, these results show that for a given measure of pulsation frequency, several sets of elastic parameters can yield the same result. More complex dependency with the external radius is also expected.

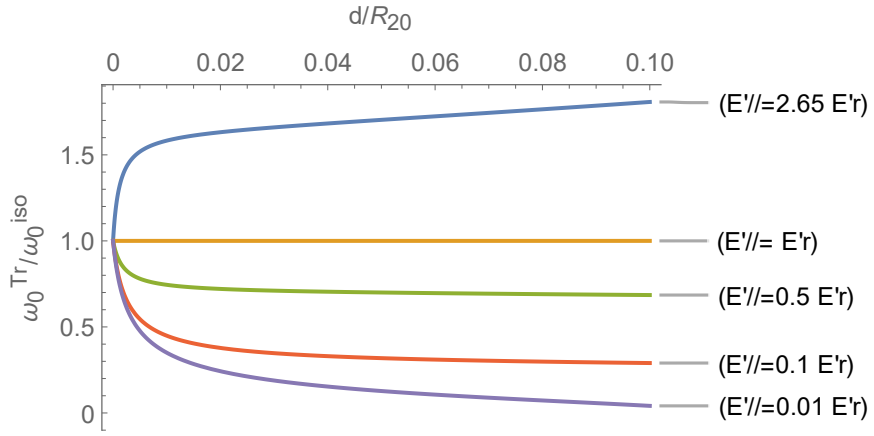

Figure 2.5: Ratio of the undamped resonance frequencies in the compressible case $\omega_0^{Tr}/\omega_0^{iso}$. The values for the in-plane and out-plane Poisson ratio are $\nu_{\parallel} = \nu_{\theta r} = 0.35$. We varied $E'_{\parallel}$ as $0.01\,E'_r$, $0.1\,E'_r$, $0.5\,E'_r$, E'_r and $2.65\,E'_r$, the isotropic constants $E' = E'_r$ and ν are set to 88.8 MPa and 0.35 respectively.

2.7 Conclusion & Perspectives

We have developed a finite thickness shell model for the oscillations of an encapsulated bubble whose material can be compressible and/or present different elastic properties in the radial and orthoradial directions. The main hypothesis is that we have neglected the mass of the shell, leading to infinite velocity for wave propagation in the material, in order to simplify the equations. The next step would be to consider the complete problem of wave propagation, as done for instance in [Doinikov et al., 2018, Doinikov and Marmottant, 2018] for a bubble oscillating in a liquid confined by a visco-elastic solid.

We have found exact expressions for the free pulsation of an encapsulated bubble, that could be used to interpret more accurately experimental characterization of UCAs. Our results suggest that neglecting compressibility will lead to underestimation of the shear modulus, and that adding some compressibility in the model may explain the apparent growth of the elastic moduli with the shell radius.

A correction of the widely used Church model [Church, 1995] is evidenced. Another correction of another model [Doinikov and Dayton, 2006] is shown, where an inconsistency in the calculation of the radii in the unstrained configuration was made.

Due to the growing interest in the development of new generation UCAs, made of various material and built with well defined radii, we expect that several opportunities to test our model will emerge in the near future. Our predictions can also be used to build more complete theories accounting for the response of the shells to external signals.

Finally, our model started to be used instead of pioneering models like in a very recent paper [Kikuchi and Kanagawa, 2021] where they study the effect of shell compressibility on the non-linear response of multiple microbubbles as well as in [Dash and Tamadapu, 2022, Sojahrood et al., 2021].

Note: Our paper [Chabouh et al., 2021] was chosen on the cover highlight

Figure 2.6: Cover highlight in JASA (biomedical acoustics), March 2021

in the Journal of Acoustical Society of America (JASA) for biomedical acoustics (see Fig.2.6).

3
Buckling Dynamics

Contents

3.1 State of the art

Buckling of UCAs has been reported in the literature numerous times. Since UCAs can be used as drug carriers [Kooiman et al., 2014], the study of their rupture mechanism has lead to evidence the buckling of microbubbles. In the work of [Bouakaz et al., 2005], they conducted a videomicroscopy experiment using a high

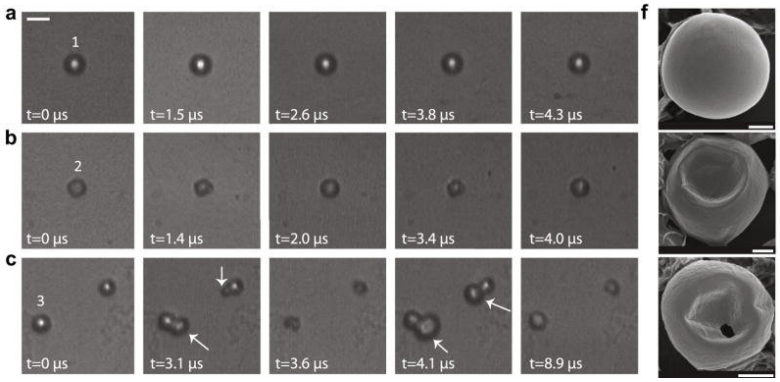

Figure 3.1: a) b) and c) Microbubbles under microscope reveals three different oscillation regimes upon acoustic excitation. f) evidence of buckling from SEM experiments. Adapted from [Helfield et al., 2017].

speed camera to observe polymer microbubbles (PB127) under different acoustic excitation. For a range of amplitudes and frequencies, microbubbles can exhibit distinct regimes of oscillation. Prior to the rupture, authors found a "transient regime" where the microbubbles are compressed without significant expansion. This transient regime was later referred to "compression-only" behavior [De Jong et al., 2007] and it is well described by the Marmottant model [Marmottant et al., 2005, Marmottant et al., 2011]. Inspired by the buckling of a lipid monolayer, this model adds an effective surface tension of the solid once the radius exceeds the buckling radius which corresponds to the spherical regime. Later, various high-speed optical observations of commercial UCAs under acoustic excitation mentioned the appearance of buckling [Chetty et al., 2008, Dollet et al., 2008, Helfield et al., 2017]. Fig.3.1, adapted from [Helfield et al., 2017], shows the above mentioned regimes for a polymeric microbubble under acoustic excitations.

'Listening' to the buckling was reported as well. In the work of [Renaud et al., 2015], the authors have noticed a decrease of the speed of sound in the medium containing microbubbles when the ambient pressure is increased above a certain threshold. This result hints for 'softening' of the medium due to microbubble buckling. An independent study has reached the same conclusion [Memoli et al., 2018]. There, the primary Bjerkness forces on commercial polymeric shells are measured; a strong rise of this force above a given amplitude of the applied acoustic field is interpreted again as a signature of the sudden 'softening' of the shell.

In a very recent work [Mokbel et al., 2021], the intrinsic dynamics of the buckled state is studied experimentally on centimetric shells and in three-dimensional axisymmetric simulations. The results are supported by a theoretical model that accurately describes the buckled shell as a two-variable-only oscillator. This study shows a potential in the understanding of this 'softening' effect reported in acoustics experiments on microbubbles.

Another approach in the study of the dynamics of rupture of UCAs is to measure the pressure at which rupture occurs during a quasi-static overpressure experiment. [Leong-Poi et al., 2002] measured the volumetric decrease resulting from an increase in static pressure and estimated the bulk modulus of polymeric UCAs by monitoring

multiple UCAs subjected to overpressure without mentioning buckling of shells.

Later on, in a similar work, [Chitnis et al., 2011] studied the rupture of polymer shells with 2 different shell-thickness-to-radius ratios ($7.5nm/\mu$m and $40nm/\mu$m). They used a linear buckling theory and a refined one that takes into account the shear component arising due to nonuniform shell thickness. They reported an agreement with this refined buckling theory to measure thickness of microbubble only for very stiff materials (Young modulus $\approx$ 1500 MPa).

Few years after, the same group [Koppolu et al., 2015] combined two different experiments, first one is a quasi-static linear increase of the hydrostatic pressure of a fluid containing microbubbles and seen under videomicroscopy. The second one is acoustic backscatter measurements. It is highlighted that the microbubbles that didn't experience buckling are the ones that had an order of magnitude higher subharmonic response. Same experiments for two different lipid microbubbles were conducted in [Thomas and Borden, 2017]. They observe a higher initial dilatational elasticity with the increase of the pressurization rate. They suppose that the stiffening of the microbubbles arises from their composition and microstructure. Another way to understand the observed stiffening is by introducing the creeping effect. When a viscoelastic structure buckles due to creep, it may be treated as an equivalent elastic structure with a lower critical load [Hayman, 1981]. Stated differently, the faster the loading, the more time needed to the instability to take place. This phenomena was studied in a very recent work [Stein-Montalvo et al., 2021]. A dynamic pressure buckling experiment was done on defect-seeded centimetric spherical shells. And the results are in great agreement with viscoelastic shell models.

Finally, in a very recent study [Yoo et al., 2022], an acoustical tweezer was used to trap a single glass microbubble and the rupture pressure is measured. Their measurements collapse well with the linear elastic buckling theory (discussed later in the present chapter)

So far, no investigation has been done on the buckling/unbuckling dynamics of UCAs and specifically before the rupture phase. The aim of the present chapter is to study this aspect experimentally on different microbubbles.

3.2 Methods

We have designed and assembled an experimental apparatus, that enables us to investigate the deformations of microbubbles in two different configurations:

- microbubbles floating against gravity far from walls.
- microbubbles stuck to the glass walls.

The advantage of the first configuration is twofold: firstly, it entitles the study of the dynamics of a free shell for a complete cycle of buckling and unbuckling. Secondly, it enables the study of the buckling-induced displacement as it will be discussed in details in Chapter 4.

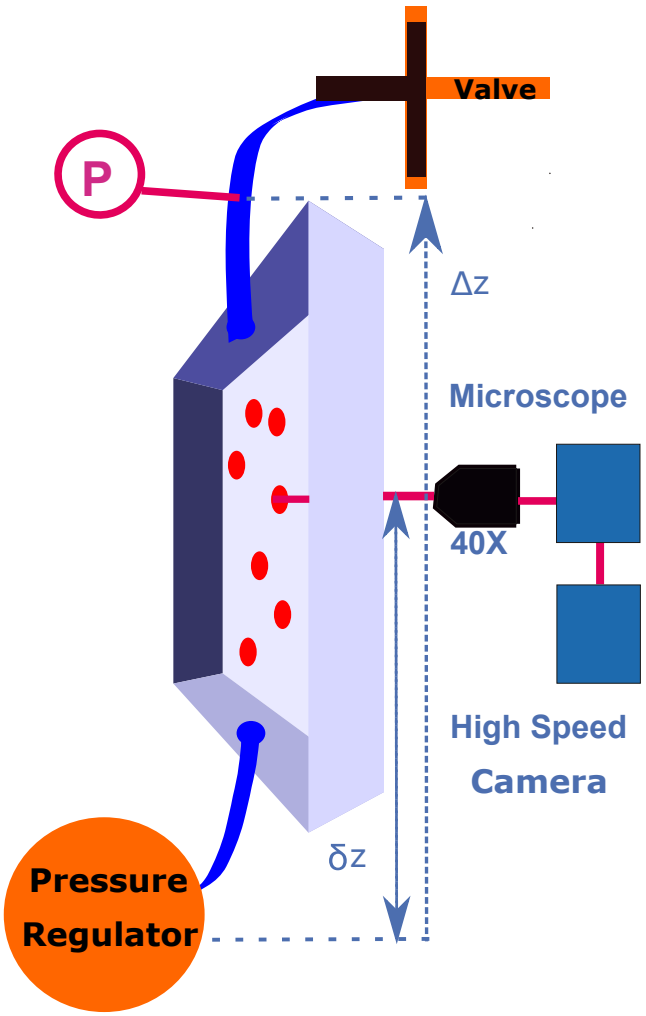

Figure 3.2: Schematic of the experimental apparatus

In the second configuration, different pressure loads can be applied, since the microbubble is contained for a very long time. For instance, a quasi-static loading i.e. a slow variation of the external pressure or a load with a step function, to study the intrinsic properties of the buckling dynamics.

3.2.1 Experimental apparatus

A schematic of the experimental apparatus is shown in Fig. 3.2. An inverted microscope (Olympus®, model IX70) is twisted 90° through three stabilizing aluminium legs. This configuration allows to have an observation axis perpendicular to gravity (z-axis). After the injection in to the chamber, which the focal plane is (xy), the microbubbles float up against gravity. With this experimental setup, their displacement and deformation can be recorded concomitantly.

A standard microfluidic system of Elveflow® is used to connect the pressure controller (Elvesys®, France) to the chamber.

A custom-built chamber used for the experiment was designed and fabricated in

our laboratory. Fig.3.3 shows a 3D-view and top-view of the piece designed using SolidWorks® (Dassault systèmes, France) software. Aluminium material is selected in order to avoid any deformation of the membrane upon pressurization owing to their high tensile strength (around 90 MPa). The chamber has a standard size of (75 mm ×25 mm) to be easily mounted on the microscope. The other dimensions are carefully selected to fit the standard size of the tubing and the microfluidic connections. The diameter of the sample medium is 25 mm with a thickness of 2 mm that gives a total fluid volume of $V \approx 980$ μL.

To close the chamber and ensure no leakage, two plain microscope slides (Corning®, USA) with a size (32 mm ×32 mm) and a thickness of 1mm were glued on the top and button surfaces using a blue epoxy adhesive Loctite® SI 5926. Note that the upper and lower surfaces need to be carefully cleaned to avoid any greasy particles to get stuck on it and prevent a perfect adhesion of the glass cover-slips. A 48 hours waiting time is required for a full adhesion before any use of the chamber. Finally, 8 aluminum bars (4 on each side) are screwed on the top and button surface to prevent any deformation of the adhesive upon pressurisation.

Since the behaviour of the microbubbles, is in general sensitive to temperature [Shekhar et al., 2018], all the experiments were conducted at room temperature. And to avoid any unwanted movement of the chamber that might alter the deformation and the displacement of the microbubbles, the whole setup is mounted on an optical table (Thorlabs®).

3.2.2 Pressure sensor calibration

A microfluidic pressure sensor (MPS1, Elvesys®, France) is mounted in series with the system. The pressure sensor is used to check if there is a time delay or amplitude shift between the measured the pressure inside the chamber (P_{meas}) and the input pressure (P_{in}) provided by the pressure controller. Following the instruction of the manufacturer, the calibration is made by connecting the pressure sensor directly to the outlet of the pressure controller. Once calibrated, the pressure sensor is inserted after the outlet of the chamber at a height $z_1 = 25$ cm. An example of pressure measurements is shown on Fig.3.4. It indicates the target pressure (P Target) that the system should follow, the input pressure (Pin), the measured pressure (P_{meas}) and the difference between them ($\Delta P = P_{in} - P_{meas}$) on one complete cycle of 40 seconds period ($T = 40$ s).

First, we see that the input pressure well respects the target pressure all the time except at the beginning, where a jump of 5 kPa is made to start and at the end of the cycle where the input pressure plateaus instead of following the sine curve. Second, the average difference between the input and the measured pressures is constant. It has a value of $\Delta P = 2.463 \pm 0.249$ kPa which corresponds to the hydrostatic pressure between the height of the pressure controller and the height of the pressure sensor. If we consider, $P_{hydro} = \rho g \Delta z$, assuming the water density, $\rho = 1000\ kg/m^3$, the acceleration of the gravity, $g = 9.81\ m/s^2$ and $\Delta z = 25 \pm 0.1$ cm gives $P_{hydro} = 2.45 \pm 0.1$ kPa ($\approx \Delta P$). We can thus conclude that the pressure inside the chamber is $P_{in} + \rho g \delta z$, where δz is the height difference between the

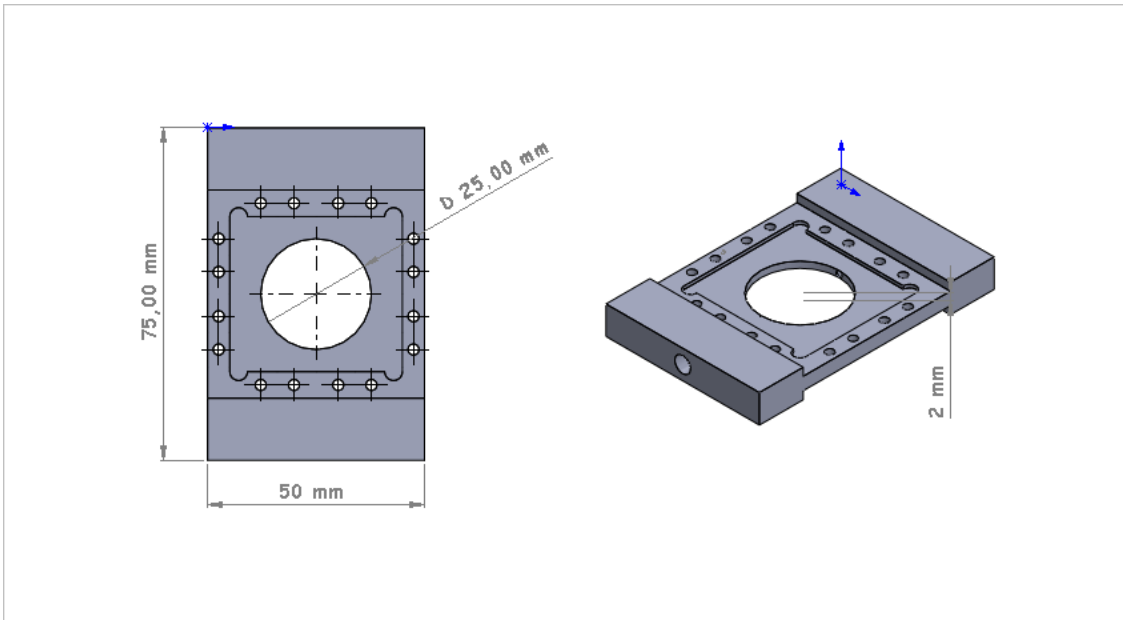

Figure 3.3: Top and 3D view of the designed chamber

considered microbubble and the pressure controller (See Fig.3.2).

3.2.3 microbubbles

All along the work presented in this thesis, we used two different UCAs. The first one, is a commercial contrast agent, SonoVue/Lumason® (Bracco Spa, Milan, Italy). It consist of a phospholipid shell encapsulating a sulfur hexafluoride gas core. Different measurements of their visco-elastic properties, obtained through various experimental techniques, can be found in the literature. As highlighted in the previous chapter and in our published work [Chabouh et al., 2021], those parameters are highly dependent on the theoretical model that is used to fit the experimental data. The elastic 2D compression modulus χ_{2D} ranges from 0.024 to 2.61 N/m, and the surface viscosity modulus κ_S from 0.1×10^{-8} to 3×10^{-8} $N/m.s$. In what follows we will use a value of 0.5 N/m for χ_{2D} and 0.5×10^{-8} $N/m.s$ for κ_S. To maintain good stability of the SonoVue® microbubbles according to the manufacturer's suggestions, they were freshly reconstituted prior to use through a mixture of the lyophilisate with 5 ml physiological saline solution, to form a suspension that contains approximately $2 - 5 \times 10^8$ shells per milliliter with diameters ranging from 2 to 7 μm.

The second population is a homemade monodisperse lipidic microbubbles, fabricated by our collaborators: PhD student Benjamin van Elburg under the supervision of Assis. Prof. Dr. Guillaume Lajoinie, Assis. Prof. Dr. Tim Segers and Prof. Dr. Michel Versluis (Physics of Fluids group, University of Twente, The Netherlands). The synthesis setup consists in a microfluidic flow-focusing device. It uses a feedback loop to control the size and monodispesity of the freshly formed microbubbles in [Van Elburg et al., 2021, Segers et al., 2020, Segers et al., 2016]. The encapsulating shell is made of phospholipid (mixture of DPPC, DPPA,

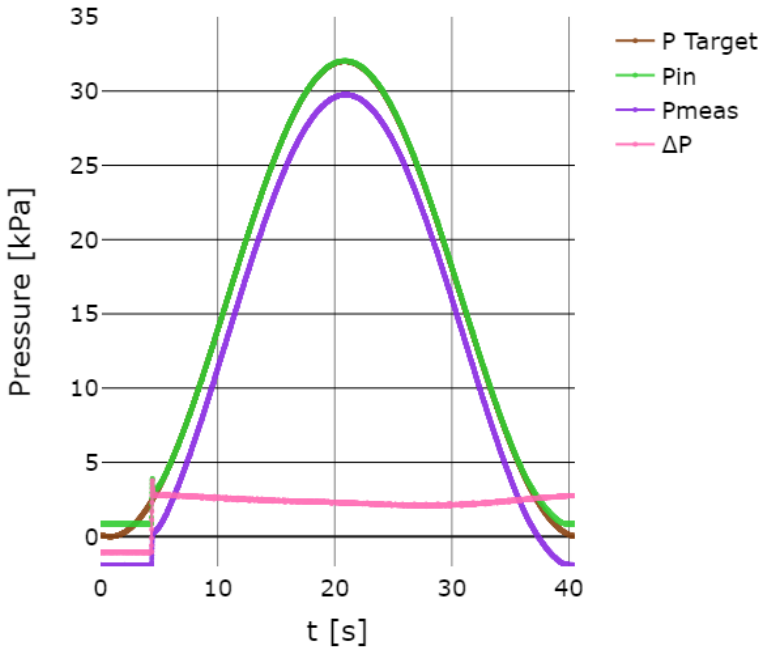

Figure 3.4: Plot of the target pressure, P_{in}, P_{meas} and the difference $\Delta P = P_{in} - P_{meas}$

and DPPE-PEG5000 in a 80:10:10 molar ratio). With this technique, χ_{2D} can be precisely tuned over one order of magnitude with values between 0.5 N/m to 4.5 N/m. We used two different batches with two different χ_{2D} : $\sim$ 0.55 and 2 N/m with average radius of 3 μm.

3.2.4 Experimental procedure

In order to avoid any air bubbles inside the medium, we first degas 500 ml of distilled water for a period of 15 minutes in a vacuum multi-staged pump. After switching the pump off, a tiny opening of the valve is done to slowly introduce ambient air to the medium at room temperature ($21 \pm 1°C$)

Second, a neat suspension of microbubbles was diluted by a factor 1000 in degassed saline (0.09% w/v) which gives an approximate concentration of $\approx 1 \times 10^5$ microbubbles per ml. The suspension is placed in a Falcon microfluidic reservoir for 15 mL (Fisher Scientific, USA). The microbubbles are injected into the chamber through application of a 30 mbar overpressure to the reservoir. The valve is closed once the chamber is full.

Microbubble deformations and motions are recorded using a fast camera (Miro 310, Vision Research) at a rate of 100 frame/s. An x,y,z automated stage (MS-2000, ASI, USA) is used to select a microbubble prior to the video acquisition.

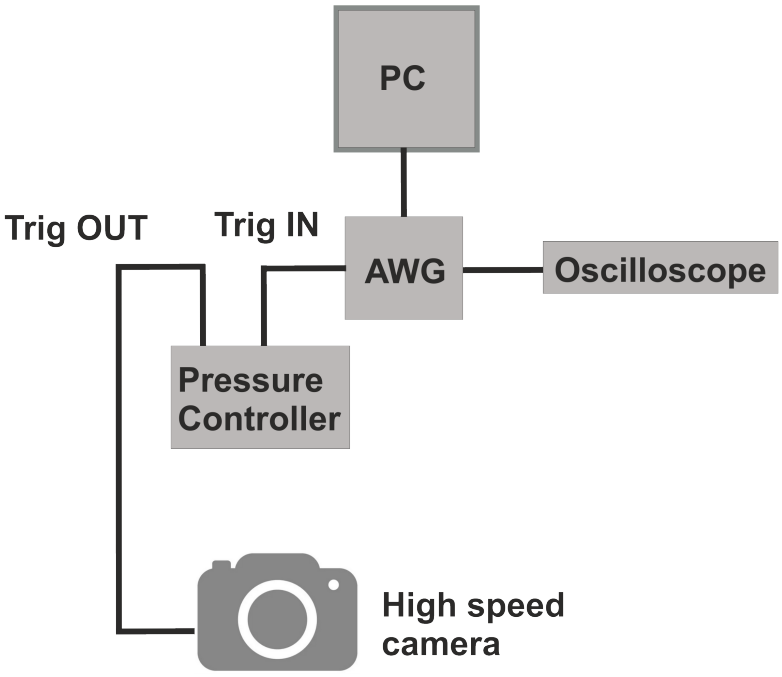

Figure 3.5: Schematic of the trigger system

3.2.5 External trigger

For the quasi-static experiments, we have developed a trigger system that is capable of setting on the pressure controller and the video acquisition at the same time by clicking one single button. This was made possible thanks to an algorithm written in the Elveflow® interface (See appendix.A.1).

Fig.3.5 shows a schematic of the system. Briefly, a square signal with an amplitude of 5V peak-to-peak and a period $T = 0.5$ ms is sent from a programmable arbitrary waveform generator AWG (33600A Series, Keysight). This signal enters the pressure controller and triggers it. At the same time an output signal leaves from the pressure controller to trigger the video acquisition. All signals are visualized using a oscilloscope (HDO 4024, Teledyne Lecroy).

At the beginning of every experiment, the amplitude of the pressure and the period can be changed and fed into the algorithm. The main purpose of this trigger, is the accurate measurement of the buckling time and the buckling pressure as it will be discussed later in this chapter.

Homemade tracking algorithm To track the microbubbles and get their deformation at every time step, we have developed a homemade tracking algorithm with sub-micron resolution.

The image of a single microbubble has a complex 2D intensity profile in the image plane. It can be well approximated by a two-dimensional (2D) elliptical Gaussian distributions of light intensity [Mann et al., 1999]. In our algorithm, we use a 2D elliptical Gaussian model with an angle θ. In the Gaussian model, the intensity is expressed as:

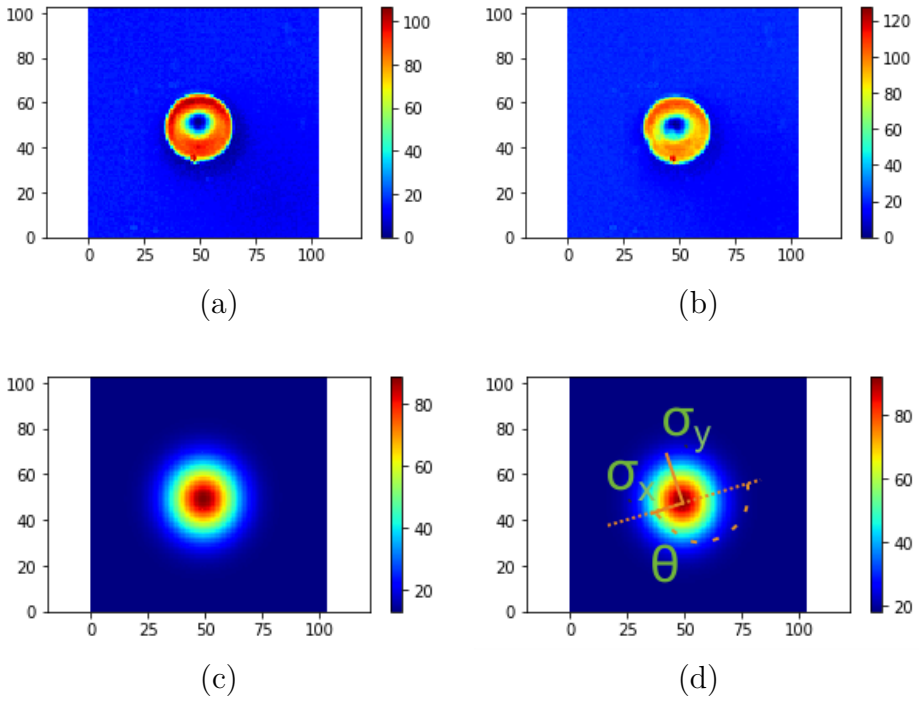

Figure 3.6: Light intensity distribution of a) raw image in , b) raw image in 'buckled' shape, c) fitted image in 'spherical' shape and d) fitted image in 'buckled' shape. In the spherical phase: $\sigma'_x = 5.11$ μm and $\sigma'_y = 5.38$, in the buckled phase: $\sigma'_x = 4.87$ μm and $\sigma'_y = 5.30$

$$I(x,y) = I_0 + A \times exp\left(-\frac{x'^2}{2\sigma'^2_x} - \frac{y'^2}{2\sigma'^2_y}\right), \tag{3.1}$$

$$\begin{cases} x' = (x - x_0)cos\theta - (y - y_0)sin\theta \\ y' = (x - x_0)sin\theta + (y - y_0)cos\theta \end{cases} \tag{3.2}$$

where (x_0, y_0) is the center coordinate of the Gaussian model, θ is the rotation angle, σ'_x and σ'_y are the standard deviation of x' and y' axis respectively, A is the Gaussian amplitude peak and I_0 is the background amplitude. The fitting parameters are estimated according to the least squares principle. After the fitting, data are processed such as θ is always the angle of the short axis i.e. $\min(\sigma'_x,\sigma'_y)$. θ is also chosen such as when the ratio σ'_x/σ'_y is minimal, the corresponding angle θ indicates the angle of the deflation as it will be later discussed. An example of the fitting is shown on Fig.3.6 where we show the initial raw and fitted image of the same shell in the unbuckled and buckled states respectively.

3.3 Buckling angle

3.3.1 Definition

If an ideal spherical shell would undergoes a buckling event, there would be no privileged orientation for the direction of buckling. For n successive cycles of buckling and unbuckling, the shell could a priori have n different buckling angles (i.e. orientation of the depression). Of course, shapes are not ideal or perfect in nature, which means that there is always a few weaker spots in the shell on which the instability could develop. Through the fabrication of seeded-defect in the shell, one can control the buckling location [Djellouli et al., 2017].

Current UCAs could have single or multiple buckling directions. Previous experimental observations of UCAs under static overpressure mentioned the 'wrinkling' of the coating surface [Kwan and Borden, 2012] and [Thomas and Borden, 2017]. Authors explain the collapse of the shell with several steps. First, a nucleation of microscopic folds takes place, which then leads to the aggregation of new folds and finally, ends up with macroscopic folding events. Those folds can be initiated anywhere on the surface with no privilege point or direction. The control of buckling direction on the micro-scale has not been reported yet. Owing to its thin lipidic encapsulation, ($\approx$ 5 nm) a microbubble submitted to uniform pressure buckles and manifest single or multiple facets, where a facet is defined as an inverted spherical cap. An example of single and multiple facet of homemade microbubbles is shown in Fig.3.7 where N is the number of facets. The pink arrow points at a microbubble with 6 facets. Similar zoology of shapes is seen in [Quemeneur et al., 2012]. They have studied the osmotic deflation of vesicles experimentally and numerically. The study supported by a simple elastic theoretical model. Authors reported a characteristic thickness for which the buckling occurs. It has a value three order of magnitude higher than the actual lipidic thickness. The same behaviour for our lipidic microbubbles is evidenced as it will be discussed in the next section. Considering the microbubbles in the floating configuration, a sinusoidal loading is applied with three different frequencies f = 1, 1.33 and 2Hz, and the amplitude P_{in}=20 kPa.

We define the aspect ratio λ as the ratio of σ'_x/σ'_y. In Fig.3.8a), we plot an example of the aspect λ (left y-axis) and the fitting angle θ (right y-axis) in function of time, for $f = 2Hz$. We can clearly see that λ varies from a value close to 1 in the spherical shape to a value around 0.88 with a sudden drop. The drop of λ refers to the buckled shape. It is thus used to define the buckling angle θ_b as seen on the inserted snapshots. The buckling spot did not change from cycle to cycle ($\theta_b \approx 120°$). But if we consider another example of the same experiment, Fig.3.8 b) shows a variation of the angle from 45 to 80 degrees. Note: the initial value of the aspect ratio is not equal to 1, even though the microbubble is in a spherical shape (no deformation). This is due to non-spherical distribution of the light intensity around the shell.

The evolution of the buckling angle from cycle to cycle will be studied in the next section.

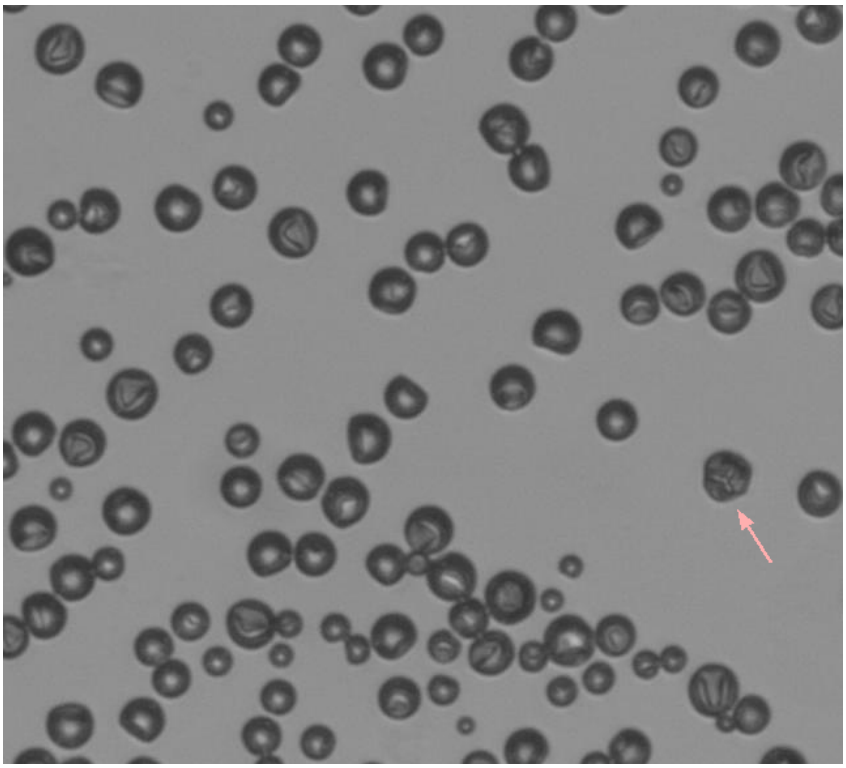

Figure 3.7: Zoology of shapes of homemade microbubbles experiencing one or multiple facets ($N = 6$ for the one shown next to the pink arrow).

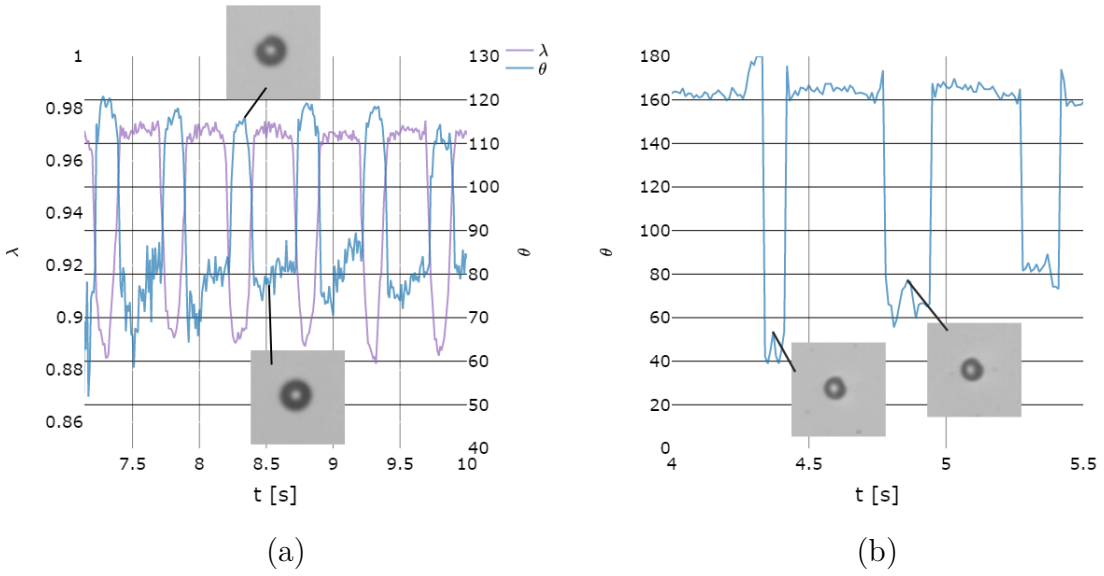

(a) (b)

Figure 3.8: Example of fitting angle θ for two different SonoVue® microbubbles of initial radius a) 2.5 μm and b) 2μm. To show clearly the measurement of the buckling angle, the minima and maxima of curve a) correspond to spherical and deflated shapes respectively, as highlighted by the inserted snapshots.

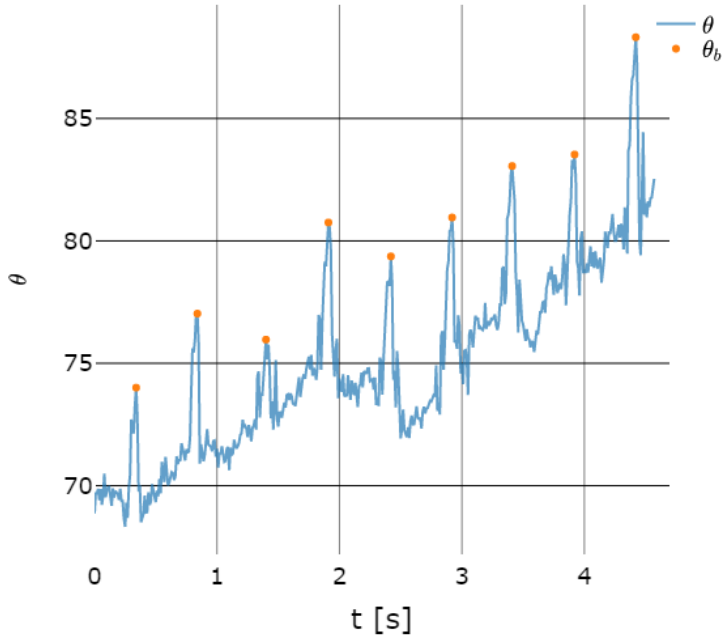

Figure 3.9: a)Plot of the evolution of the angle θ and of the buckling angle on each cycle θ_b as a function of time for a chosen microbubble.

3.3.2 Evolution per cycle

The physical question that we would like to answer is whether the shells exhibit single or multiple buckling spot. Fig.3.9 shows the evolution of the buckling angle θ_b of a chosen microbubble (θ_b being the local extremum per cycle).

As we cannot track material points on the shell, we use an indirect method to study the evolution of the buckling angle via the rotational diffusion coefficient D_r. Rotational diffusion is the counterpart of translational diffusion, which maintains or restores the equilibrium statistical distribution of particles' position in space. The rotational diffusion coefficient of a single colloidal sphere with radius R suspended in a solvent with shear viscosity μ is given by the familiar Stokes–Einstein–Debye (SED) relation ([Stokes, 1856, Einstein, 1906, Debye, 1929]):

$$D_0^r = \frac{k_B T}{f_0^r} = \frac{k_B T}{8\pi\mu R^3}, \tag{3.3}$$

with $k_B T$ the thermal energy and f_0^r the Stokesian friction factor. The mean-square angular deviation varies linearly with time and has D_0^r as a coefficient of proportionality. If there is only one buckling spot, we then have:

$$\langle \theta_b^2 \rangle = 2 D_0^r t \tag{3.4}$$

We assume that the buckled shell is a sphere with a reduced radius ≈ 0.96 the initial radius. Note that this assumption will be validated later on throughout the chapter. Applying Eq.3.3 for $k_BT = 4 \times 10^{-21}$ J, $\mu = 1$ mPa.s (water) and $R = 0.96 \times 3 = 2.88\ \mu m$, we get a theoretical rotational diffusion coefficient of $D_0^r = 6.52 \times 10^{-3}\ rad^2/s$. The pressure cycle has a period of t=0.5s, injecting this value in Eq.3.4 and taking the square root, one gets the following root mean square (RMS) of the buckled angle per period: $\theta_{b,RMS} = 0.081rad = 4.62°$.

The equation of the mean-square angular deviation as a function of time is given as:

$$\langle \theta_b^2(t) \rangle = \frac{1}{\sum_{i=1}^{N_T} N_i(t)} \sum_{i=1}^{N_T} \sum_{t_j=1}^{N_i(t)} \left[\theta_b(t_j + t) - \theta_b(t_j) \right]^2, \tag{3.5}$$

where N_T is the total number of trajectories, time t_j refers to the time for the jth image in the track and N_i is the number of images considered for the ith trajectory. We look at the variation of the angle between 2 cycles for 2 different frequencies $f = 1$ Hz and $f = 2$ Hz as plotted in Fig.3.10a) and b). Events of high $\Delta\theta$ are more probable to occur at low frequency which hints for multiple buckling spots. For $f = 2$Hz, 97.9% of microbubbles shows a changing of the buckling angle within ± 40 degrees. In contrast for $f = 1$ Hz, only 70.78% of microbubbles shows the same change. We exclude the data where $\Delta\theta$ exceeds ± 40 degrees in what it follows and we fit the distribution with a Gaussian function.

For the frequency of 2 Hz, in Fig.3.10c) we plot the standard deviation squared of the following times $(t = 0.5s, 1s, ...4s)$ which corresponds to cycle number $1, 2...8$. The variation of the average $\bar{m}$ in function of time is negligible $\bar{m} = 0.1 \pm 0.49$ hence $\sigma^2(t)$ can be approximated to $\langle \theta_b^2(t) \rangle$. Finally, $\sigma^2(t)$ is well fitted with a linear function of time $(A\sqrt{t})$ and we obtain a RMS of the buckled angle: $\theta_{b,RMS} = 3.64°$ in agreement with the theoretical prediction mentioned above. Similar value is measured with $f = 1$ Hz (not shown here).

This finding shows that the shells mostly have a unique buckling spot and this spot allows to check the rotation of the shell which is well approximated as a Brownian divisional rotation. An interesting consequence of this result is that upon high frequency, the shell does not have enough time to relax all the surface after every cycle, thus the weak point developed does not change. Similar results are seen in the literature [Luan et al., 2014] where they refer to buckling as "lipid shedding". The frequency used was 1 MHz and an acoustic pressure was varied from 50 to 425 kPa. Also in [Helfield et al., 2017] (See supplementary movies for more details).

3.4 Height & Width

A relevant parameter to look at when studying the buckling of spherical shells is the "height" of the folded envelope of the shell. A common method to study non-spherical oscillations of UCAs [Dollet et al., 2008] is the use of the quantity $R(\theta)$ which is the radius and different angles θ. Here instead, we define this height

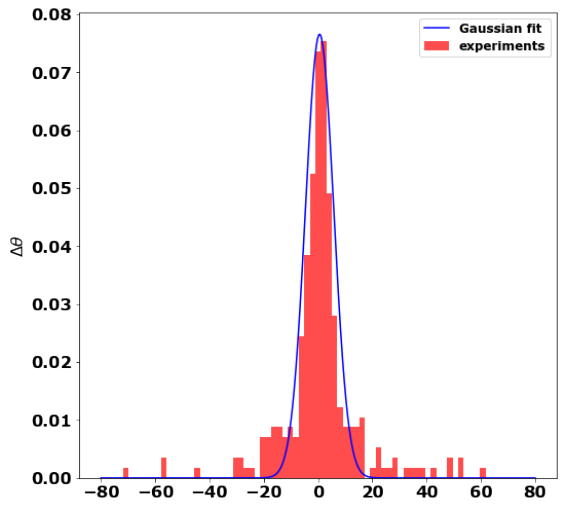

(a)

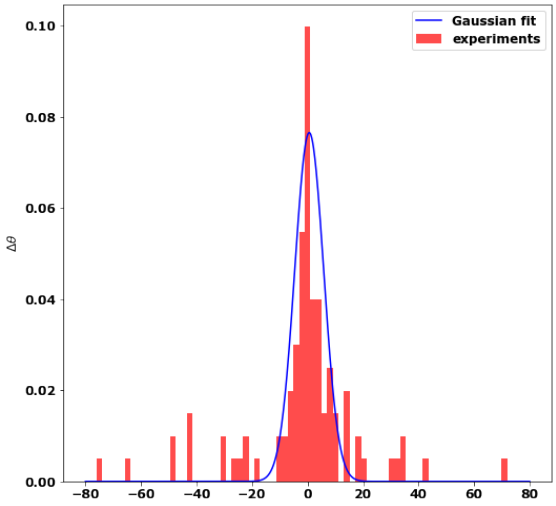

(b)

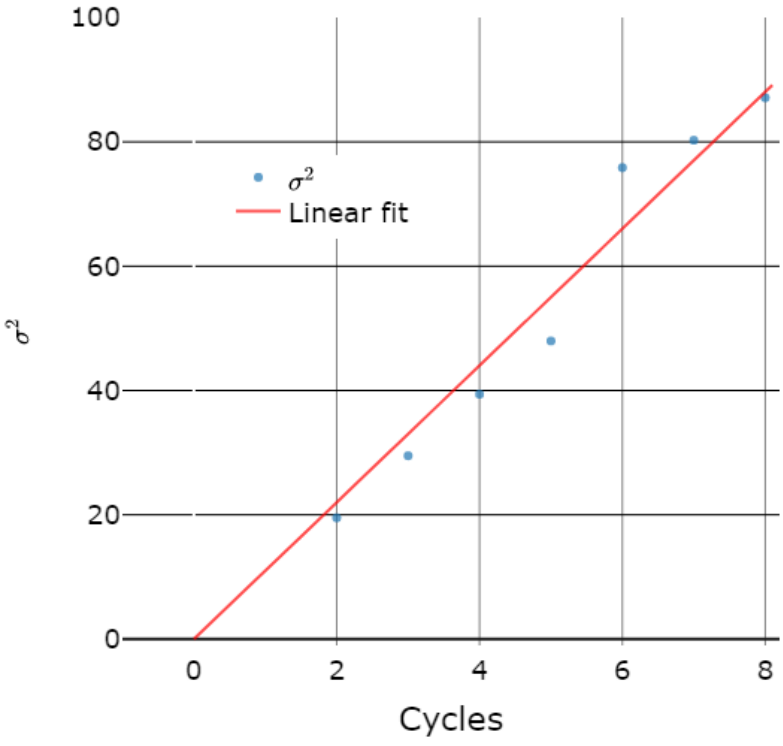

(c)

Figure 3.10: Histogram of $\Delta\theta$ for a duration of 1 cycle a) ($f = 2$Hz), b)($f = 1$Hz) and c) Standard deviation squared of the buckling angle in function of the cycle number for $f = 2$Hz.

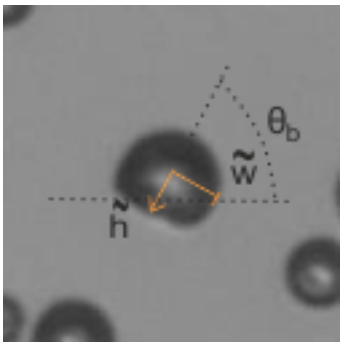

Figure 3.11: Illustration of $\tilde{h}$ and $\tilde{w}$ on a chosen buckled microbubble, a homemade UCA with $\chi_{2D} = 0.5$ N/m and an initial radius $R = 3$ μm.

$\tilde{h}$ (and $\tilde{w}$) as the standard deviation of the light intensity in the direction of the buckling (and normal to the buckling angle) as illustrated in Fig.3.11.

Derivation

We propose the determination of the value of the light intensity in the buckling direction, for that, x' is replaced by $rcos(\theta - \theta_b)$ and y' by $rsin(\theta - \theta_b)$ in Eq.3.1. The intensity profile becomes:

$$I(x,y) = I_0 + A \times exp\left[-\frac{\left(\sigma_y'^2 cos^2(\theta-\theta_b) + \sigma_x'^2 sin^2(\theta-\theta_b)\right) r^2}{2\sigma_x'^2\sigma_y'^2}\right], \tag{3.6}$$

Hence, the above equation can be written as:

$$I(x,y) = I_0 + A \times exp\left(-\frac{r^2}{2\tilde{h}^2}\right), \tag{3.7}$$

with,

$$\tilde{h}(t) = \frac{\sigma_x'\sigma_y'}{\sqrt{\sigma_x'^2 + (\sigma_y'^2 - \sigma_x'^2)cos^2(\theta-\theta_b)}} \tag{3.8}$$

In the direction perpendicular to θ_b, we can replace the angle by $\theta - \theta_b + \pi/2$ and get:

$$\tilde{w}(t) = \frac{\sigma_x'\sigma_y'}{\sqrt{\sigma_x'^2 + (\sigma_y'^2 - \sigma_x'^2)sin^2(\theta-\theta_b)}} \tag{3.9}$$

Throughout this chapter, we will study the evolution of these parameters θ_b, $\tilde{h}$, $\tilde{w}$ and λ as function of time and of the loading to get more insight about the complexity

of the buckling phenomena. It is important to note, that the choice of $\tilde{h}$ and $\tilde{w}$ is similar to earlier studies experimentally on a centimetric shells [Djellouli et al., 2017, Stein-Montalvo et al., 2021] and numerically on micrometric shells [Mokbel et al., 2021], except that herein the parameters are based on light intensity profiles.

3.5 Quasi-static load

The aim of this section is to study the behaviour of the shell with a very slow variation of the pressure. In general, it is interesting to use a slow input to create a fast or "strong" output which is exactly what an instability is good for, for instance, to achieve an artificial muscle actuation [Yang et al., 2016]. In a practical way, it is convenient to use the **near wall configuration** for this experiment since the microbubbles would not stay long enough in the frame due to the buoyancy. In fact, the floating speed of a microbubble of radius 3 μm is around 20μm/s. It means that in maximum 10 seconds, the microbubble disappears from the image frame. Thus, in this configuration, we can investigate the effect of slow pressurization. As mentioned before, the measurement of the pressure inside the chamber was done thanks to the pressure sensor introduced in series with the flow circulation.

3.5.1 Evolution in time

We applied a sinusoidal load with a 32 kPa amplitude and a period $T = 40$s. The considered shell is a homemade UCA with $\chi_{2D} = 2$ N/m. The evolution of the aspect ratio λ and the pressure are shown in Fig.3.12 a). First, the ratio begins to decrease slowly until a sudden drop, at a certain pressure, which indicates the buckling event. The inserted snapshot shows the non-spherical distribution of the light intensity around the shell as discussed in 3.3.1. The evolution of the corresponding $\tilde{h}(t)$ and $\tilde{w}(t)$ are shown in Fig.3.12 b). After the pressure starts to increase inside the chamber ($t = 4.3$s) both the height and the weight start to decrease in a linear manner; the slope is fitted with a linear curve that passes through (0,0) with a slope 0.91. It indicates the isotropic spherical compression. At $t \sim 13$s, the projected height $\tilde{h}$ decreases down to 2.3 μm while $\tilde{w}$ increases to a value even higher than the raw "width" of the spherical initial configuration. In the classical buckling behaviour of thin objects as discussed in [Holmes, 2019], it is known that when the outer pressure is still increasing, further volumetric compression requires a lot of energy. An energy-cheap way to react is to bend. This triggers the buckling instability. At $t = 21.5$s, the pressure begins to decrease and the shell starts to re-inflate until it becomes unstable again and another instability takes place, named debuckling: where the shell shifts back to the spherical compressed shape.

It is also important to mention that upon buckling, the shell undergoes post buckling oscillations as it will be discussed later in this chapter.

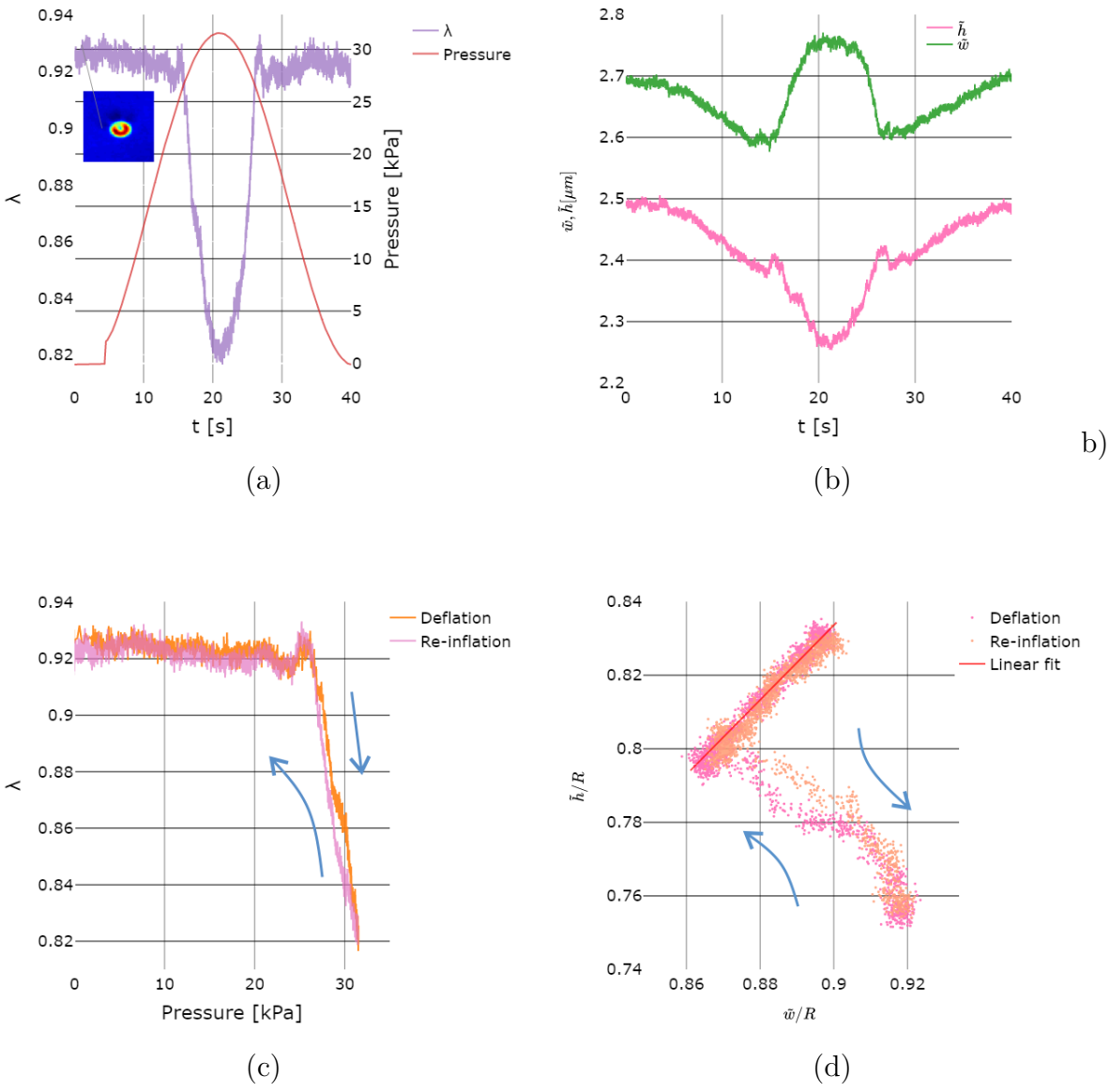

(a) (b) (c) (d)

Figure 3.12: Evolution in time of a) the aspect ratio of the microbubble and the pressure. b) the projected height $\tilde{h}$ and the projected width $\tilde{w}$. The inserted snapshot is the grey level intensity of the first frame image showing asymmetry. c) Evolution of λ in function of the pressure. The arrows shows the time direction (clockwise) and d) The projected height $\tilde{h}$ in function of the projected width $\tilde{w}$, both normalized with the initial radius $R = 3$ μm. The red curve is a fit with a linear curve passing through (0,0) with a slope 0.91 within an error 0.01% which indicates the linear decay.

3.5.2 Shape hysteresis

The deformation speed v_d can be measured as $max(|d\tilde{h}/dt|)$, it has a value $v_d = 30$ ± 0.14 mm/s. The associated Reynolds number is $Re_d = 0.15$. At low Re_d regime, the time of the deformation does not matter on the swimming [Purcell, 1977]. In order to apply the "Scallop theorem" the deformation of a swimmer should not be time-reversible. In the case of our shell, it is important to check if the deformation upon deflation follows the same path as the one upon the re-inflation. To answer these questions, we plot in Fig3.12 c) and d), the variation of $\tilde{h}/R$ in function of $\tilde{w}/R$ with $R = 3\mu$m being the initial radius, and the variation of λ in function of the measured pressure inside the chamber. In the later, we notice that when $\tilde{h}/R$ decrease, so does $\tilde{w}/R$ and it is in a linear fashion, which corresponds to the isotropic compression as stated before. The compression is followed by a sudden collapse of $\tilde{h}$.

In both plots, the deformation does not follow the same path during deflation and re-inflation. It manifests what we call a "shape hysteresis".

3.5.3 3D numerical simulation comparison

This result can be compared to a three-dimensional axisymmetric simulations done by our collaborators (PhD student Marcel Mokbel under the supervision of Prof. Dr. Sebastian Aland) in Dresden, Germany. (see [Mokbel et al., 2021] for more information). It is based on the Arbitrary Lagrangian Eulerian (ALE) method which couples between an Eulerian frame of reference for the fluid and a Lagrangian frame of reference for the elastic material. Briefly, it consists in solving the Navier-Stokes equation around a thin shell immersed in a fluid. A sinusoidal pressure loading with an amplitude of 177 kPa is applied over a period $T = 10$s. It has the same configuration mentioned in the paper i.e. a microbubble with a Yong modulus $E = 0.5$ MPa, atmospheric pressure $P_0 = 100$ kPa, water dynamic viscosity $\eta = 1$ mPa.s, initial radius $R_0 = 22.5\mu$m and shell thickness $d = 5\mu$m. The equivalent 2D compression modulus χ_{2D} is defined as $E/2(1-\nu)$ where ν is the Poisson coefficient. Assuming an incompressible material of the shell ($\nu = 0.5$) and we get a $\chi_{2D} = 2.5$ N/m. This value is close to the one measured on the homemade UCAs as mentioned in Sec.3.2.3.

For the sake of comparison with our experimental work, the exact same results are plot in Fig.3.13. First, in a) a drop of λ prior to buckling is also recovered as for the experiments. Second at $P = 140$ kPa, the buckling occurs and a more important drop of λ is seen followed by a more pronounced postbuckling oscillations. After this phase, the pressure goes even higher where the shell is squished until the re-inflation takes place at $t = 5$s. Two seconds later, the debuckling phase starts with a jump of lower amplitude compared to the buckling one. Contrary to the experimental result, in Fig.3.13b) the shape hysteresis is more pronounced in the numerical simulation. This might be due to the damping of the shell since the 3D simulations use an elastic membrane with no viscosity. More quantification of this effect will be discussed later in this chapter. Another interesting thing to note is the time-direction evolution of the parameters. For both experimental data and numerical simulations, the direction of time is clockwise for the evolution of the aspect ratio λ in function of

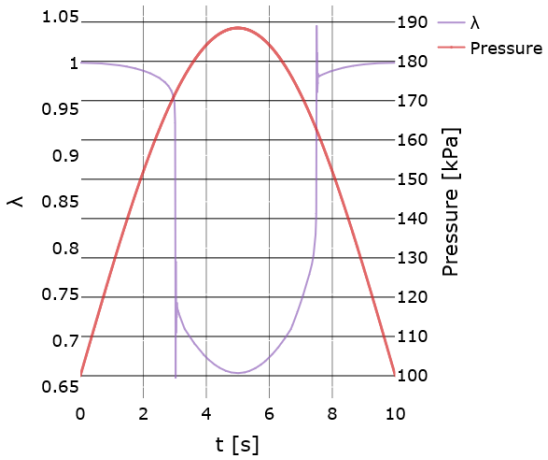

(a)

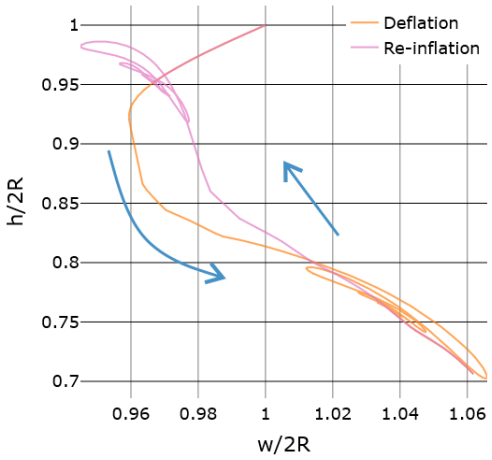

(b)

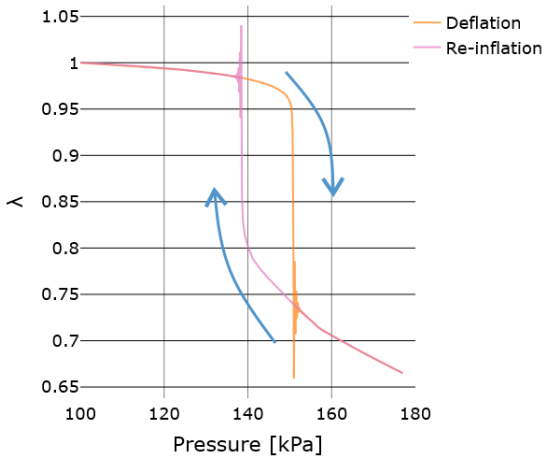

(c)

Figure 3.13: 3D axisymmetric numerical simulation showing the evolution in time of a) the aspect ratio and the pressure. b) the normalized height and width. c) The aspect ratio in function of the pressure. The arrows show the time direction (anti-clockwise for b) and clockwise for c)).

the pressure. On the other hand, the evolution of the height $\tilde{h}$ in function of $\tilde{w}$ is clockwise while the one of the numerical simulation is anti-clockwise. The reason is that for the numerical part, the amplitude of the collapse of the actual height $h(t)$ is higher than the one of the enlargement of the actual width $w(t)$ upon buckling. While for the experiment, both amplitudes are similar since the measurement of the projected height $\tilde{h}(t)$ is smaller than the actual height of the shell.

3.5.4 Buckling pressure

Back in 1915, [Zoelly, 1915] derived the first critical pressure prediction for which a thin walled spherical structure undergoes a catastrophic failure called "buckling". For a perfect sphere with no imperfections, the critical pressure is given by:

$$P_c = \frac{2E}{\sqrt{3(1-\nu^2)}}\left(\frac{d}{R}\right)^2, \tag{3.10}$$

with d the thickness of the shell and R the initial radius. As mentioned earlier, the 2D compression modulus is given by:

$$\chi_{2D} = \frac{Ed}{2(1-\nu)}, \tag{3.11}$$

Usually, engineers design their structures with a critical load smaller than the theoretical predicted one due to the imperfections of the material. In 1930, the space agency NASA and collaborators introduced a knockdown factor $k_d \equiv P_c^e/P_c$. It was later chosen to be ≈ 0.2 for a very safe design [SP, 1969].

In classical small strain theory of plates, the bending modulus B can be expressed as:

$$B = \frac{Ed^3}{12(1-\nu^2)} = \frac{\chi_{2D}d^2}{6(1+\nu)}, \tag{3.12}$$

Using the 2D compression modulus χ_{2D} and the bending modulus B, the critical buckling pressure can be written as:

$$P_c = \frac{8}{\sqrt{2}}\frac{\sqrt{B\chi_{2D}}}{R^2}\sqrt{1-\nu} \tag{3.13}$$

If we consider our homemade UCAs, χ_{2D} ranges between 0.5 to 2 N/m. For an initial radius of 3μm, assuming a thickness of the lipid monolayer $d = 5$ nm and an incompressible material $\nu = 0.5$, the theoretical critical pressure P_c ranges between 0.4 to 1.6 kPa.

Experimentally, we measure the buckling pressure by repeating twice the same loading on the same shell for 8 different shells of the same batch ($\chi_{2D} = 2$ N/m). Fig.3.14, shows an example on a shell where we plot the aspect ratio λ in function of the measured pressure. For every pressure cycle, the experiment is repeated twice. Interestingly, we notice the sudden change of λ for all the tries at a pressure $P_b = 24$ kPa. Same experiments done on 8 different shells reveals different values of P_b ranging from 18 to 25 kPa. These values are an order of magnitude higher than the theoretical predicted ones. This mismatch was already mentioned in the literature [Chitnis et al., 2011]. They used different polymeric UCAs with unknown shell properties under static overpressure. Using Eq.3.10 with the measured $P_{rupture}$

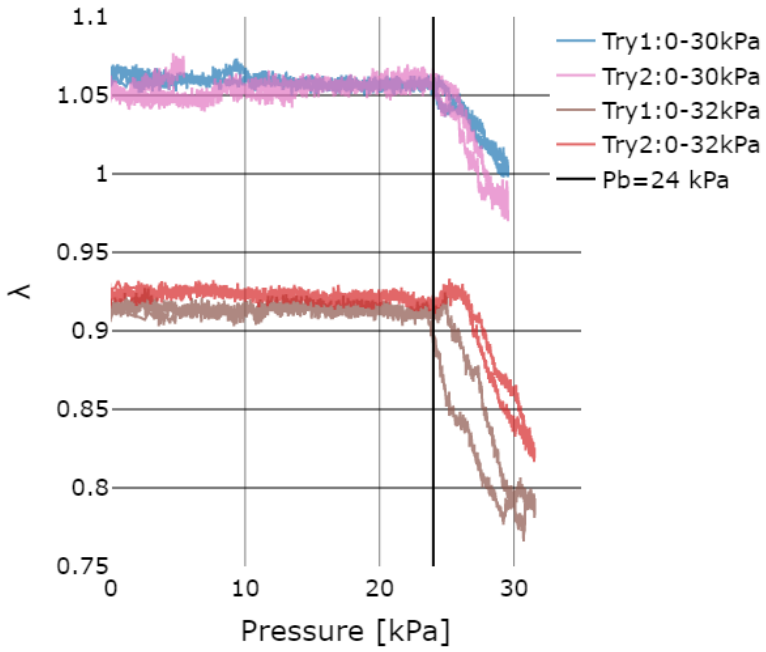

Figure 3.14: Experimental measurements of λ in function of the pressure for the same shell (initial radius $R = 3\mu$m) for 2 different amplitude loads.

and $d/R = 40nm/\mu m$, they got an equivalent 2D compression modulus of 25.2 N/m an order of magnitude higher the values reported in the literature using different techniques for polymer coated microbubbles (see Table 2.4 in Chap2). Using Eq.3.13, the bending modulus can be estimated and from Eq.3.12, an equivalent thickness can be derived $d_{eq} = \sqrt{6(1+\nu)B/\chi_{2D}}$. The physical meaning of the later quantity is an apparent thickness for which the buckling happens at the observed experimental buckling pressure. For an incompressible shell material ($\nu = 0.5$), and using the measured bending modulus we get $d_{eq} = 0.384 \pm 0.05$ μm which is 2 orders of magnitude greater than both bilayer thickness (~ 5 nm). The same effect was seen on the buckling of lipidic vesicles (lipid shell enclosing liquid) in [Quemeneur et al., 2012], which also, suggests the anisotropy in the material.

3.6 Dynamic buckling load

In the previous section, we studied the quasi-static buckling of the shells. If we ask ourselves, what is the behaviour of the shell after buckling it is hard to answer using quasi-static loading, since any change can be due to intrinsic properties of the shell but it can be also due to the pressure that is still varying. A way to deal with that is by using a "Dynamic buckling" experiment [Sieber et al., 2019]. Dynamic buckling is the study of deformation of spherical shells subject to a rapidly

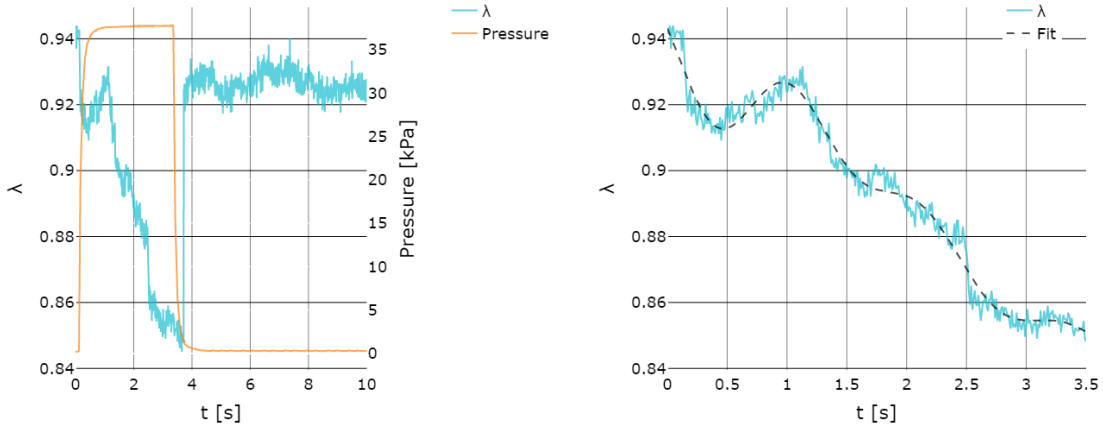

Figure 3.15: a) Recordings of the pressure and the associate deformation of the shell through the aspect ratio λ. b) Zoom on the buckled phase, the dashed black curve is the theoretical fit.

applied step in external pressure.

We performed a step function pressure loading on the homemade UCAs with $\chi_{2D} = 2$ N/m in the near-wall configuration. In Fig.3.15, we show an example of this experiment. The right vertical axis presents the evolution of the aspect ratio λ and the left one shows the variation of the measured pressure. The x-axis shows the time. The first drop of the aspect ratio corresponds to a pressure of 14 kPa. After the pressure plateaus at $t = 0.5$s the shell undergoes a postbuckling oscillations until $t = 4$s. Right after, the pressure is turned off and goes directly back to 0. At the same time, λ jumps up to a value close to the initial value indicating the debuckling phase. It is also clear how the deformation does not follow the same path during deflation and re-inflation which is the signature of the shape hysteresis as stated earlier.

Postbuckling oscillations

To discuss the postbuckling, in fig.3.15b), we zoom on the first 4 seconds to see how the shell reacts when the external pressure is stable. We fit our experimental data with a sum of two cosine waves with two frequencies ω_1 and ω_2. We obtain the following parameters: $\omega_1 = 5.2$ rad/s, $\omega_2 = 0.08$ rad/s, amplitudes $A_1 = 0.008$ rad/s, and $A_2 = 0.96$ with a phase shift of $\phi = 0.95$ rad. The second pulsation ω_2 is too small to be measured on such a short time interval. The associated term is basically a constant on this time interval. The same experiment is repeated on 16 different shells of the same batch and the corresponding average postbuckling oscillation period is: $T_{Pb} = 0.82 \pm 0.21$ s.

The Marmottant model is the well known model that is used to describe the oscillations of UCAs with taking into account the buckling of the shell [Marmottant

et al., 2005]. In this model, when the shell is buckled, the only contribution on the oscillation is the compressibility of the gas. Recently, [Mokbel et al., 2021] studied the postbuckling behaviour experimentally on centimetric elastic spherical shells and numerically. The study is supported with a theoretical model that is based on a two-variable-only harmonic oscillator. Two non-dimensional resonance pulsations were derived, one (ω_+) that accounts for the volume oscillations and the other one (ω_-) for the surface oscillations. Using equation (4.20) of this paper with the following microbubble parameters: $\chi_{2D} = 2$ N/m, ambient pressure $P_0 = 101.31$ kPa, $d_{eq} = 0.13$ μm, initial radius $R = 3$ μm, $\kappa = 1.4$, $\alpha_{1,2}$ and k_{VS} are taken from the paper we get: $\omega_1 = 7.84$ MHz and $\omega_2 = 1.27$ MHz. The post buckling and debuckling oscillations were several order of magnitudes smaller than the ones predicted in [Mokbel et al., 2021]. A reason for the mismatch can be that in the this model the bending energy is neglected which has a flattened landscape compared to the stretching energy. Another reason can be the high damping effect of the shell which was also neglected in the model.

3.7 Conclusions & perspectives

We have studied in this chapter, the buckling dynamics of two types of UCAs, commercial (SonoVue®) and monodisperse homemade shells. Two different configurations were used, a floating configuration and a near wall configuration. In the former one, we showed that at a frequency higher than 2Hz, the microbubbles are more likely to manifest one buckling spot. Through the mono-spot buckling we quantified the rotation of the shell while floating and we proved that it is only due to the Brownian rotational diffusion. In the later configuration, we studied the buckling dynamics of the homemade UCAs using two different loading pressure. The first one is a slow sinusoidal pressure load that enabled to measure the buckling pressure. A characteristic thickness for lipidic shells was measured thanks to the experimental buckling pressure and revealed the anisotropy of the material. A comparison with numerical simulation was made and is consistent with our findings. The second one is a ramp pressure load, that enabled to study the postbuckling oscillations. In both cases, the shape hysteresis was evidenced which might be a key factor for the swimming-induced motion through buckling mechanism. This will be subject of the next chapter.

4
Swimming

Contents

4.1 Introduction

In several biological systems [Farutin et al., 2013], as well as many artificial microswimmers [Degen, 2014] we can find the 'change of shape' as a swimming mechanism. When a microrobot or microorganism perform a shape deformation, they generate a fluid flow around them. The flow is characterized by a Reynolds number $Re = UL/\eta$, with U as the typical deformation velocity, L is the characteristic microswimmer length, and η as the kinematic viscosity of the surrounding fluid. With this parameter Re, two regimes for self propulsion exist. One way is to perform a very fast stroke such as $Re \gg 1$, it is commonly known as the inertial effect. Inertial regime can be found in nature, for instance, when insects use thin flapping wings [Michelin and Llewellyn Smith, 2009]. On the other hand, when the speed of the deformation is not high enough, the resulting Re for a

microswimmer is less than unity. The low Re regime is commonly known as Stokes regime where the fluid dynamics is dominated by viscous rather than inertial terms. In order to produce a net positive displacement in the Stokes regime, the cyclic deformation pattern must not be invariant under timereversal in confirmation with the 'scallop theorem' [Purcell, 1977]. It states that a purely reversible sequence of deformations is not associated with any net motion.

Here, we consider the microbubble as a self-deforming or shape-changing object. In the previous chapter, we saw that its deformation speed upon buckling v_d is in order of 30 mm/s; for an average size of 3 microns the Re associated is less than unity, hence it fits in the Stokes regime. We also saw that the microbubble upon a full cycle of deflation and re-inflation manifest a shape hysteresis.

We discuss in this chapter, whether this shape hysteresis can be an efficient way to swim in such regime or not.

4.2 Single shell

We use the 'floating-configuration' (Chap.3, Sec.3.2) to conduct this experiment. The goal is to measure the displacement of the shells and relating it to the buckling events. After their injection, microbubbles start to float against gravity due to the buoyancy force. Assuming a microbubble density similar to the one of air ($\rho_s = 1.225$ kg/m^3 and using the Stokes law, the sedimenting velocity is given by [Stokes, 1850]:

$$v_b = \frac{2}{9}\frac{(\rho_s - \rho_f)gR^2}{\mu}, \tag{4.1}$$

where g is the acceleration of the gravity. Considering a 3 microns shell, the velocity is estimated as: $v_b \approx -20\mu m/s$. The negative sign indicates the floating. The image captured by the camera has a size of 640×480 (pixel units). To compute the traveled distance in μm, we use the camera pixel size. It has a value of 20 μm and under a 40X microscope objective, the conversion ratio is 0.5 μm/pixel. Thus, the total traveled distance is around 300 μm. For an acquisition speed of 100 frames per second, one movie lasts about 17 seconds and with an activation frequency of 2 Hz, we got at least 30 buckling events per shell. The pressure profile used is a sinusoidal wave of amplitude $P = 20$ kPa. We varied the frequency in the experiments for $f = 1$Hz and $f = 2$Hz.

4.2.1 Measurement corrections

The chamber was designed to fully sustain relatively high pressure with no leakage or deformations. Although, in practice, having an a 100% water filled reservoir is not realistic. There will always remain some air pockets inside which might create undesired microflows when the chamber is submitted to pressure cycles. Another source of error in the measurement of the displacement is the misalignment of the camera with the vertical direction. To overcome these two above-mentioned sources of errors, we add prior to every experiment a suspension of 5 μm average

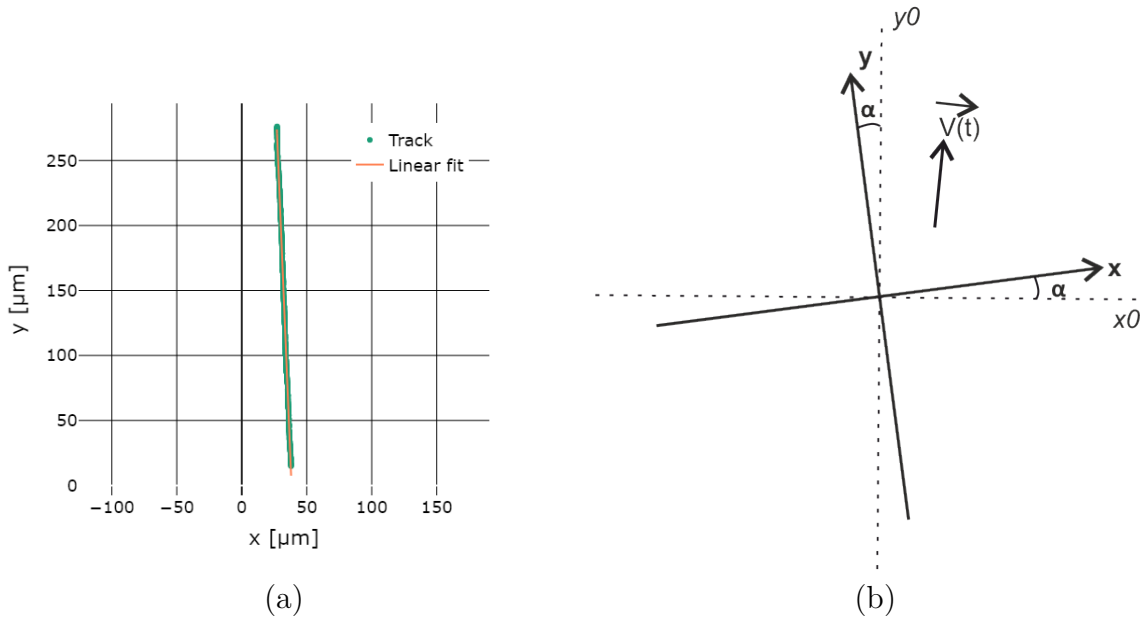

(a) (b)

Figure 4.1: a) An example of a reconstructed trajectory of a reference bead with a linear fitting with an angle b) Scheme of the reference (x_0, y_0) frame and the corrected frame (x, y).

diameter hollow glass beads (HGMS, Cospheric, USA) with a density of $0.1 - 0.7$ g/cm^3. The wide spread of the density is due to the polydispersity in size of the glass beads. They float with the microbubbles and they do not buckle when the pressure is applied owing to their hard encapsulating shell. They are thus used as reference particles due to their ability to provide the direction of gravity potentially biased by microflows, as well as the noise on the data.

4.2.2 Frames & References

We determine the direction of biased gravity α by means of the reference beads. Let us consider the fixed frame (x_0, y_0) associated to an image. Fig.4.1a) shows an example of the trajectory of a bead after tracking. It is fitted with a straight line tilted by 92.3° from the x_0 axis. We apply the same analysis on all the beads: each one has an angle α_i with $i = 1, 2...N$ and N is the number of beads per experiment. After that, we define another frame (x, y) that is rotated from the frame (x_0, y_0) by an angle $\alpha = \frac{1}{N}\sum_{i=1}^{N}\alpha_i - 90$. In this new frame, we find $\alpha = 2.09° \pm 1.047$, all the beads goes in average in the y direction.

Both references are shown in Fig.4.1b), if we consider at an instant t the velocity of a microbubble $v(t)$, it is the result of the contribution of 3 main movements.

$$\vec{v}(t) = \vec{v_b}(t) + \vec{v_p}(t) + \vec{v_s}(t) \tag{4.2}$$

where, $\vec{v_b}(t)$ is the floating speed as mentioned before, $\vec{v_p}(t)$ is the perturbative velocity due to the undesired microflows and $\vec{v_s}(t)$ is the swimming velocity.

Projecting the above equation in the x-direction of the frame (x, y) we get:

$$v_x(t) = v_{sx}(t) \tag{4.3}$$

The only speed that remains is the x component of the swimming velocity $v_{sx}(t)$. Through the x-projection, we are sure that any movement will be due to the swimming of the microbubbles only.

4.2.3 Swimming motion

The trajectory of a microbubble is represented in Fig.4.2 a) by the minimum intensity projection. The yellow line is the reconstructed trajectory thanks to the homemade tracking algorithm introduced in Chap.3, Sec.3.2.5. In the considered microbubble, we apply a loading (pressure variation) with a sinusoidal profile of amplitude 20 kPa and frequency $f = 2$Hz. For this microbubble of initial radius $R_0 = 2.7\ \mu m$, we see a clear deviation to the right for a distance $d = 7\ \mu m$ which is $\sim 2.6 \times R_0$. The buckling angle is $\theta_b = 30°$. Let us check how the velocity behaves upon every deflation and re-inflation. On the same figure c) we plot the evolution of λ (on the left vertical axis) and the x-component of the velocity (on the right vertical axis). An interesting concomitancy is worth mentioning here: the instant λ drops (ratio of σ'_x/σ'_y see Chap.3 Sec.3.2.5), the velocity v_x along x peaks to a positive value with a postbuckling oscillation as seen one the same figure d). Inversely, upon the re-inflation, v_x peaks to a negative value while λ goes back to the initial value. For a better visualization, we plot the averaged signals over 25 cycles of λ and v_x on 1 cycle ($T = 0.5s$). We clearly see an amplitude consequent to the buckling that is higher to the one we see during debuckling. We integrate the velocity signal over time and we get an average displacement of 0.83 μm/cycle which is roughly 30% its radius per cycle.

4.2.4 Swimming direction

An important question to ask is if the microbubble propels itself in the direction of the deflation or not? To answer this question, we measure the net displacement in the direction of the buckling angle. The following analysis procedure is applied for every considered microbubble that encounters N pressure cycles:

- At every cycle, we get the buckling angle $\theta_b|_i$ with $i = 1, 2, ..., N$.
- we divide v_x by $cos(\theta_b)|_i$
- we integrate the above relation on every cycle.

The motivation for the above mentioned division is to retrieve the velocity in the buckling direction, using only the information in the x direction where we expect no biases as stated earlier.

Fig.4.3a) and b) show the net displacement/cycle for SonoVue® microbubbles for an external driving frequency of 1Hz and 2Hz respectively. In In Fig.4.3 c) the

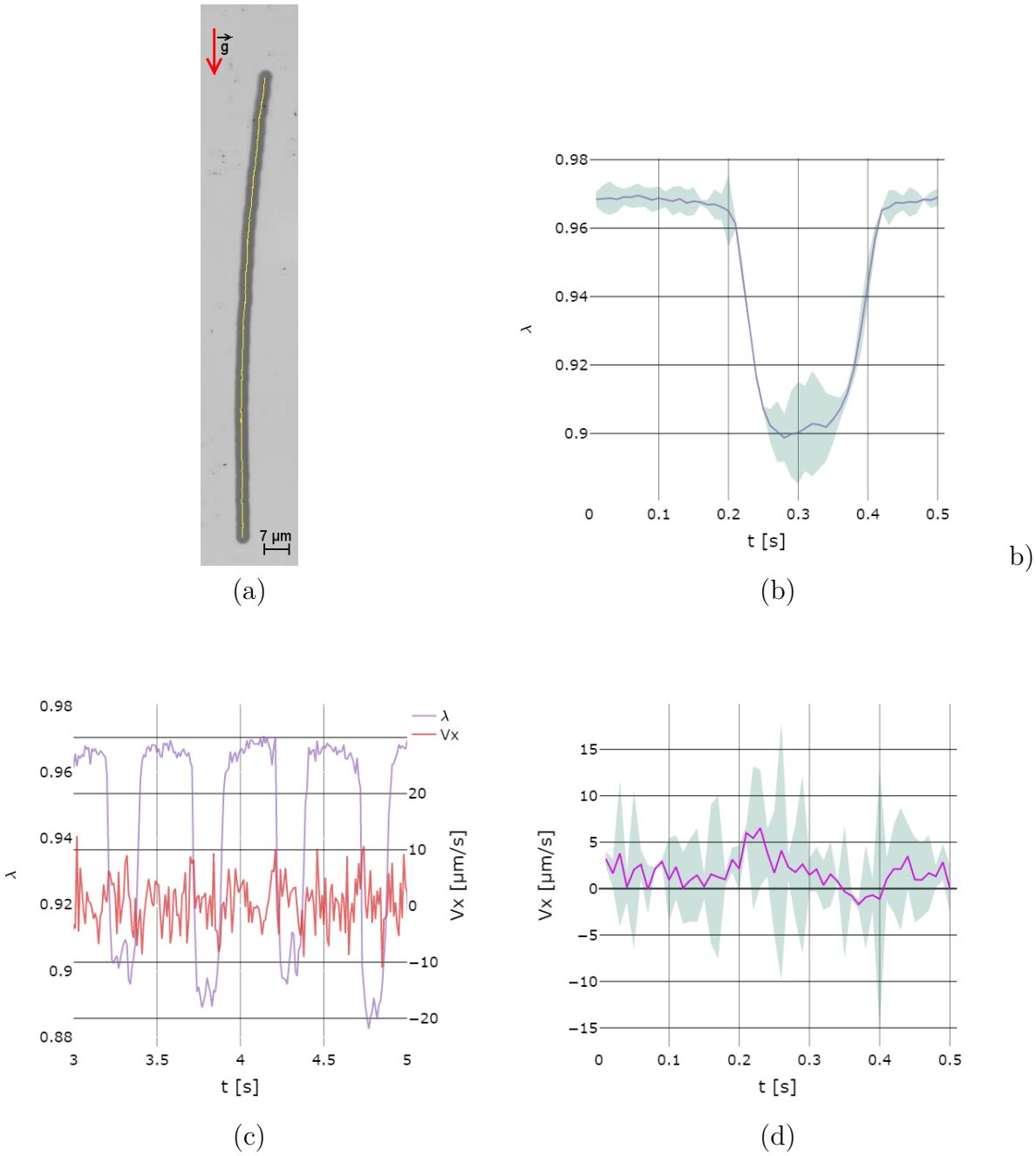

Figure 4.2: a) Example minimum intensity projection with the tracking of a microbubble b) Averaged λ on 25 cycles c) Simultaneous measurements of λ and v_x during 4 cycles and d) average v_x on 25 cycles. The gray envelope shows the standard deviation.

net displacement/cycle for the homemade microbubbles. We add on each of these plots the net displacement/cycle for the control (reference beads). The data shows the average net displacement on all the cycles (at least 7 cycles per shell) with the error bar being the standard deviation. A prominent feature in this plot is the non-zero net displacement of the microbubbles. While for the reference beads, since they do not buckle, their net displacement is negligible. If we consider a single point of the data, it has a high standard deviation that indicates a difference in the behaviour from cycle to cycle. The spread can be induced from an inaccuracy of the measurement of the swimming direction. We do not control the measurements in the 3rd direction ($\vec{z}$-axis pointing out of the paper).

We refer, in what if follows, to a "forward" propulsion when the net displacement is positive and we refer to a "backward" propulsion when the net displacement is negative. For the SonoVue® at $f = 1$Hz (Fig.4.3a)), we notice that every shell is doing a backward motion since the error bar per shell does not cross the $y = 0$ line. While for the SonoVue® at 2Hz and the homemade microbubbles, we actually have the two scenarios forward and backward motion.

The overlaid boxplot in Fig.4.3d) summarizes all the swimming experiments on SonoVue® microbubbles for two different frequencies $f = 1Hz$ and $f = 2Hz$ and for the homemade microbubbles for only one frequency $f = 1Hz$. In all experiments, reference beads with a similar density (which do not buckle) were added as a control. A statistical significance in the net displacement of microbubbles is shown through a Student T-test (exact $p - value = 2 \times 10^{-6}$). Homemade microbubbles show higher net displacement compared to SonoVue®, it can be understood by their higher elastic moduli. In fact the 2D compression modulus $\chi_{2D} = 2$ N/m for the homemade microbubbles is higher than ~ 0.5 for SonoVue®). In addition, we know that the final volume after buckling is proportional to the elastic moduli [Quilliet, 2012], as it will be estimated in the next section. A higher volume of fluid is set into motion. Note that the reason for not varying the frequency for the experiments with the homemade microbubbles is purely technical. The buckling pressure as measured in the previous chapter for the homemade microbubbles is higher than the one of SonoVue®, for a frequency above $1Hz$, the pressure inside the chamber do not have the necessary time to attain the buckling pressure. The error bars on the homemade microbubbles is considerably smaller than the errors on SonoVue® since the homemade microbubbles are monodisperse in their size.

4.3 Ballasted microswimmer

During one of the swimming experiments introduced and analyzed in this chapter, we saw a "strange body" sedimenting with the gravity. This was in contrast to what we usually see: the upstream motion of the microbubbles due to the buoyancy force. This body consists of one SonoVue® microbubble, bounded to two other smaller glass microspheres. When the pressure is applied those two spheres do not buckle. Such behavior is shown in Fig.4.4, with a sequence of spherical and buckled shape of the microbubble. In what it follows, we will refer to this body as the 'Ballasted microswimmer'. We will see in the following how to quantify such effect.

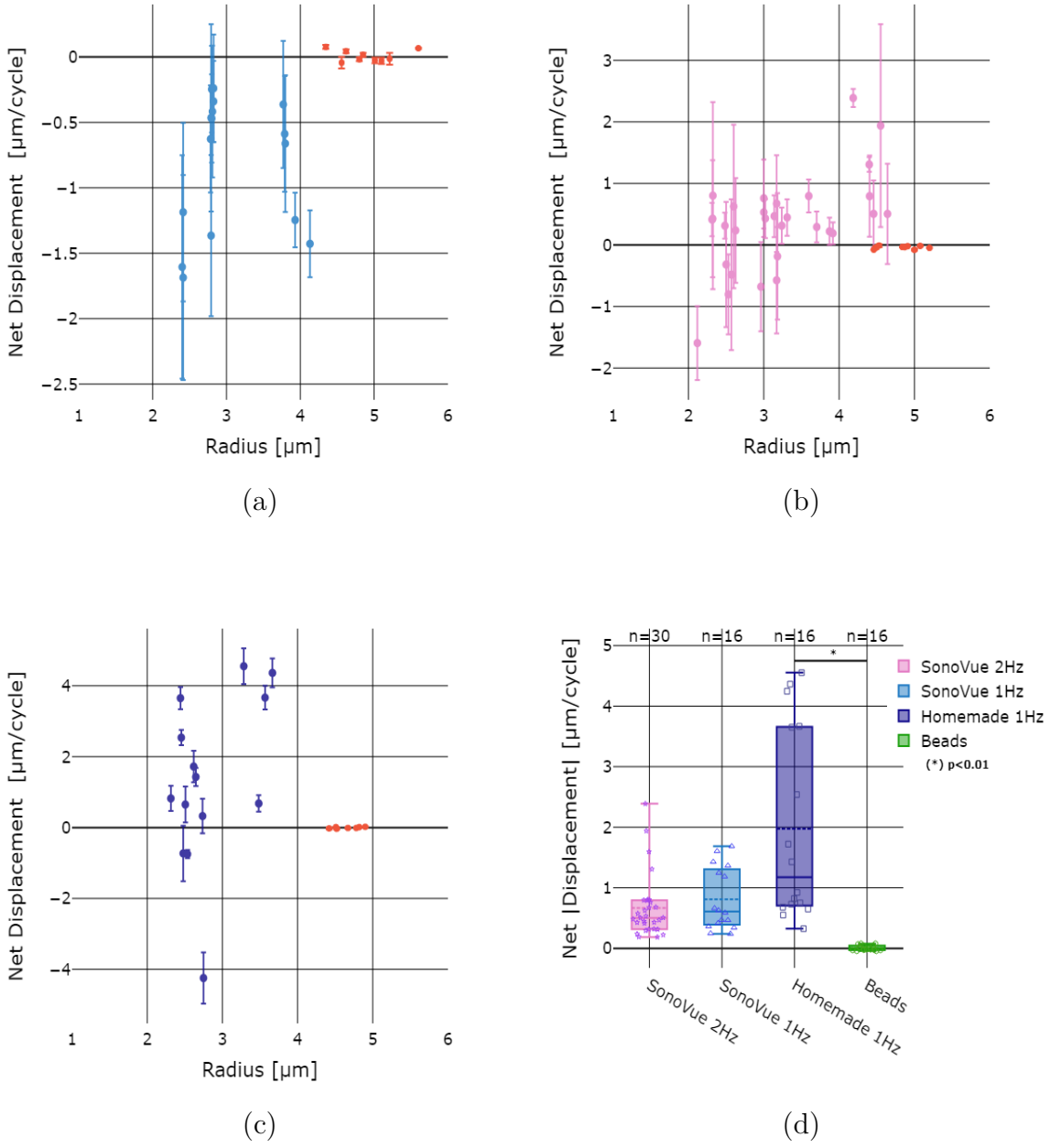

Figure 4.3: Net displacement/cycle for SonoVue® UCAs in function of the radius at a) $f = 1$Hz, b) $f = 2$Hz, c) Net displacement/cycle for homemade microbubbles at $f = 1$Hz and d) The absolute net displacement of SonoVue® UCAs (two different frequencies), homemade UCAs and control (glass beads). Each symbol represents net displacement averaged on at least 8 cycles. The overlaid boxplots show the median, interquartile range, mean, and the minimum to maximum values. Statistical significance indicated with * Student T-test ($p < 0.01$).

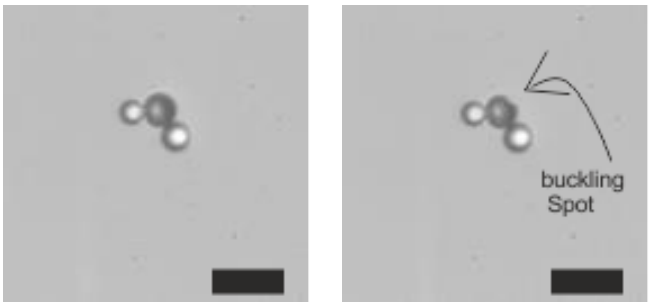

$t = 0$ ms $t = 200$ ms

Figure 4.4: Snapshot of the Ballasted microswimmer at two successive moments showing spherical shape and buckled shape. The scale bar represents 15 μm.

4.3.1 Video analysis

To track the trajectory as well as the deformation of the ballasted microswimmer, we first get rid of the two glass microspheres. This step is made by applying a high filter threshold to separate the beads from the middle shell. The remaining contour of each glass bead is filled with pixels with a grey level equal to the average grey level of the background. Second, we use the same tracking algorithm developed in this thesis to get the position and speed as function of time from the recorded and pre-processed videos of the ballasted microswimmer. We also use the same reference frame (x, y) as discussed in the previous section. We remind that the corrected frame (x, y) accounts for the misalignment of the camera with the vertical direction and for any undesired microflows encountered during the pressurization of the chamber. The frequency of the activation $f = 2Hz$ is fixed as well ass the sinusoidal loading of amplitude 20 kPa.

4.3.2 Sedimentation

A part of the trajectory of the ballasted microswimmer is shown in Fig.4.5a) to give an idea of the motion. Reader can refer to the movie online. An example of the trajectory on one cycle ($T = 0.5$s) can be visualized on Fig.4.5b). The ballasted microswimmer undergoes a buckling event and swims up against gravity for a duration τ_1 as indicated by the green arrow. After the deflation phase, the ballasted microswimmer sediments for a duration τ_2 in the buckled shape. After that, the ballasted microswimmer undergoes a debuckling phase and swims down for a duration τ_3 . Finally, after the re-inflation phase, the ballasted microswimmer sediments in a spherical shape for a duration $\tau_4 = T - (\tau_1 + \tau_2 + \tau_3)$.

In order to extract the swimming motion *i.e.* the net displacement, we need to account for the sedimentation in the spherical shape as well as in the buckled shape. In fact, when the shell buckles, it looses a certain amount of its volume, thus the buoyancy force decreases which means that it sediments faster.

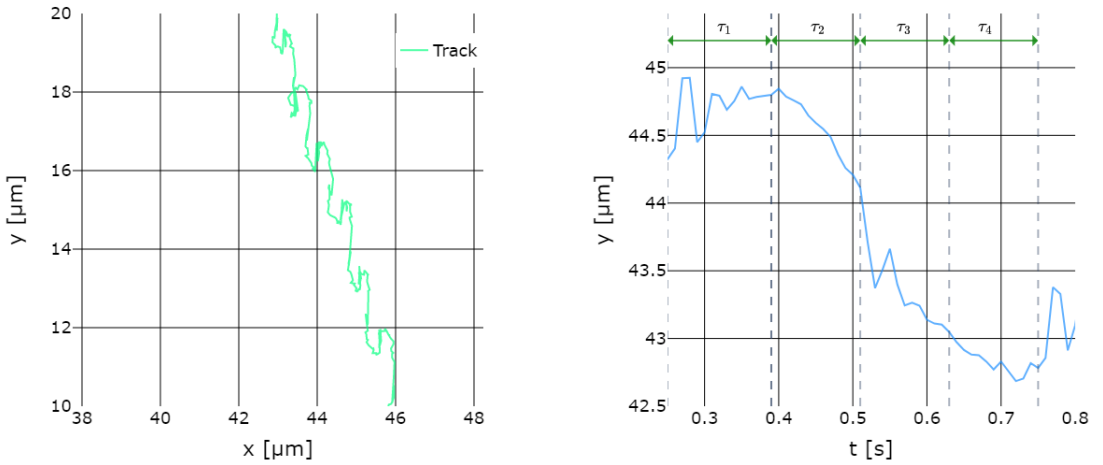

(a) (b)

Figure 4.5: a) Part of the tracking trajectory of the ballasted microswimmer under excitation (See Movie Online). b) Zoom of the trajectory on one cycle ($T = 0.5$s), τ_1 represents the buckling phase, τ_2 represents the post-buckling phase, τ_3 represents the debuckling phase and τ_4 represents the spherical phase.

Unbuckled microswimmer

Thanks to the experiments without applying a load ($P_{in} = 0$), we measured the sedimentation velocity in the spherical shape. With the relation $v_s = \sqrt{\bar{v_x}^2 + \bar{v_y}^2}$, where $\bar{v_x}$ and $\bar{v_y}$ are the time average of the velocity in the x and y direction respectively. With this we get $v_s = 1.32 \pm 0.1$ μm/s.

Estimation of the body weight

The sedimentation velocity in the spherical is shape do not vary in function of time thus, we can estimate the body weight through the classical Newton's 1^{st} law:

$$\vec{F_W} + \vec{F_D} + \vec{F_B} = \vec{0} \tag{4.4}$$

where $\vec{F}_w$, $\vec{F}_d$ and $\vec{F}_b$ are the weight of the particle, the drag force and the buoyancy force respectively. Note that there is no effect of added mass since the radial velocity is much smaller than the sedimenting velocity ($dR/dt \ll v_s$).

We assume that the drag force on the three-body microswimmer is the sum of the drag on each sphere [Stokes, 1856]:

$$\vec{F_D} = 6\pi\eta_f\gamma\vec{v}_s, \tag{4.5}$$

where η_f is the dynamic viscosity of the hosting fluid and $\gamma = (R_1 + R_2 + R_3)$. Note that the value of γ is in agreement with the experimental values reported in the literature [Lee and Leith, 1989] for the drag force on agglomerated spheres.

The buoyancy force writes:

$$\vec{F_B} = \rho_f V_0 \vec{g}, \tag{4.6}$$

where ρ_f is the fluid density, and V_0 is the volume of the unbuckled ballasted swimmer hence formed from 3 spherical shells: $V_0 = \frac{4}{3}\pi\left(R_1^3 + R_2^3 + R_3^3\right)$.

Injecting Eq.(4.3) and Eq.(4.4) in Eq.(4.2) and projecting it along $\vec{y}$ axis one gets:

$$F_W = 6\pi\eta_f(R_1 + R_2 + R_3)v_s + \frac{4}{3}\pi\left(R_1^3 + R_2^3 + R_3^3\right)\rho_f g, \tag{4.7}$$

We can deduce a value of $F_W = 5.744 \pm 0.59$ pN considering the following parameters: $\rho_f = 1000$ kg/m^3, $\eta_f = 10^{-3}$ Pa.s, $R_1 = 2.5$ μm, $R_2 = 4.5$ μm and $R_3 = 3$ μm. Note that the initial values of the radii of the spheres from left to right in Fig.4.4 are R_i with $(i = 1, 2, 3)$.

Buckled microswimmer

An estimation of the final volume of the microswimmer after buckling is made by the estimation of the of the volume of the (central) buckled shell. It can be achieved through the use of the "plateau value" ΔP_{pl} which is the minimum value of the outside-inside pressure difference ΔP. An estimation of this quantity was done in a numerical simulation study [Quilliet, 2012], and it was later extended to a wider range of d/R values by fitting it to experimental data [Coupier et al., 2019]:

$$\Delta P_{pl} = \frac{E}{(1-\nu^2)^{0.75}}\left(2.34 \times 10^{-6} + 0.9(d/R)^{2.57}\right), \tag{4.8}$$

We assume that the gas obeys a polytropic law, PV^κ is constant, where κ is the polytropic exponent of the gas. Hence the final volume fraction V_f/V_0 can be written as:

$$\frac{V_f}{V_0} = \left(\frac{P_0}{P_f}\right)^{1/\kappa} = \left(\frac{P_0}{P_0 - \Delta P_{pl}}\right)^{1/\kappa}, \tag{4.9}$$

Injecting Eq.4.8 in the above equation and applying it with the following microbubble parameters: $E = \chi_{2D} d_{eq}$, $\nu = 0.5$, $\chi_{2D} = 0.5$ N/m and $d_{eq} = 0.31$ μm, $P_0 = 101.31$ kPa and $R = 4.5$ μm. We get a final fraction volume $V_f/V_0 = 0.88 \pm 0.12$, which means that the shell looses $\sim 12\%$ of its volume when it is buckled. Note that, we use the equivalent thickness of the shell and not the actual thickness due to the increase of the bending energy for lipidic shells as discussed in the previous chapter (See Chap.3 Sec.3.5.4)

Finally, we get the sedimentation velocity in the buckled shape v_b by re-writing Eq. (4.5) for the buckled state assuming same drag force between the two states, we get:

$$v_b = \frac{F_W - \frac{4\pi}{3}\rho_f g\,(R_1^3 + R_3^3 + 0.88R_2^3)}{6\pi\eta_f(R_1 + R_2 + R_3)} \tag{4.10}$$

For the value of F_W found in the above and in the same conditions of the fluid: $v_b = 4.32 \pm 0.2$ μm/s which is $\sim 3 \times v_0$.

4.3.3 Results & discussion

Net displacement per cycle

The net displacement d_{net} is the displacement due to the sole swimming after every cycle without the sedimentation contribution $\vec{d_s}$:

$$\vec{d_{net}} = \vec{d_T} - \vec{d_s} \tag{4.11}$$

The estimation of the sedimentation traveled distance is performed on all the different phases: $d_s = d_1 + d_2 + d_3 + d_4$. During the 1^{st} phase (buckling phase), the shell is going from a spherical shape (downward velocity v_0) to a completely buckled shape (downward velocity $v_b > v_0$), the distance traveled d_1 in this phase can be bounded as:

$$v_0\tau_1 < d_1 < v_b\tau_1, \tag{4.12}$$

For the 2^{nd} phase which corresponds to the sedimentation in the buckled shape, hence the distanced traveled d_2 is bounded such as:

$$d_2 = v_b\tau_2, \tag{4.13}$$

In the debuckling phase 3, the shell goes from a buckled shape to a spherical shape, the distance d_3 traveled is :

$$v_0\tau_3 < d_3 < v_b\tau_3, \tag{4.14}$$

And finally, in the last phase, the ballasted microswimmer sediments with a spherical shape of the shell:

$$d_4 = v_0\tau_4 = v_0(T - \tau_1 - \tau_2 - \tau_3), \tag{4.15}$$

We can measure the duration of every phase by plotting the stack of the velocity in the y-direction on one cycle. Fig. 4.6a) shows a 25-cycles stack of the velocity in

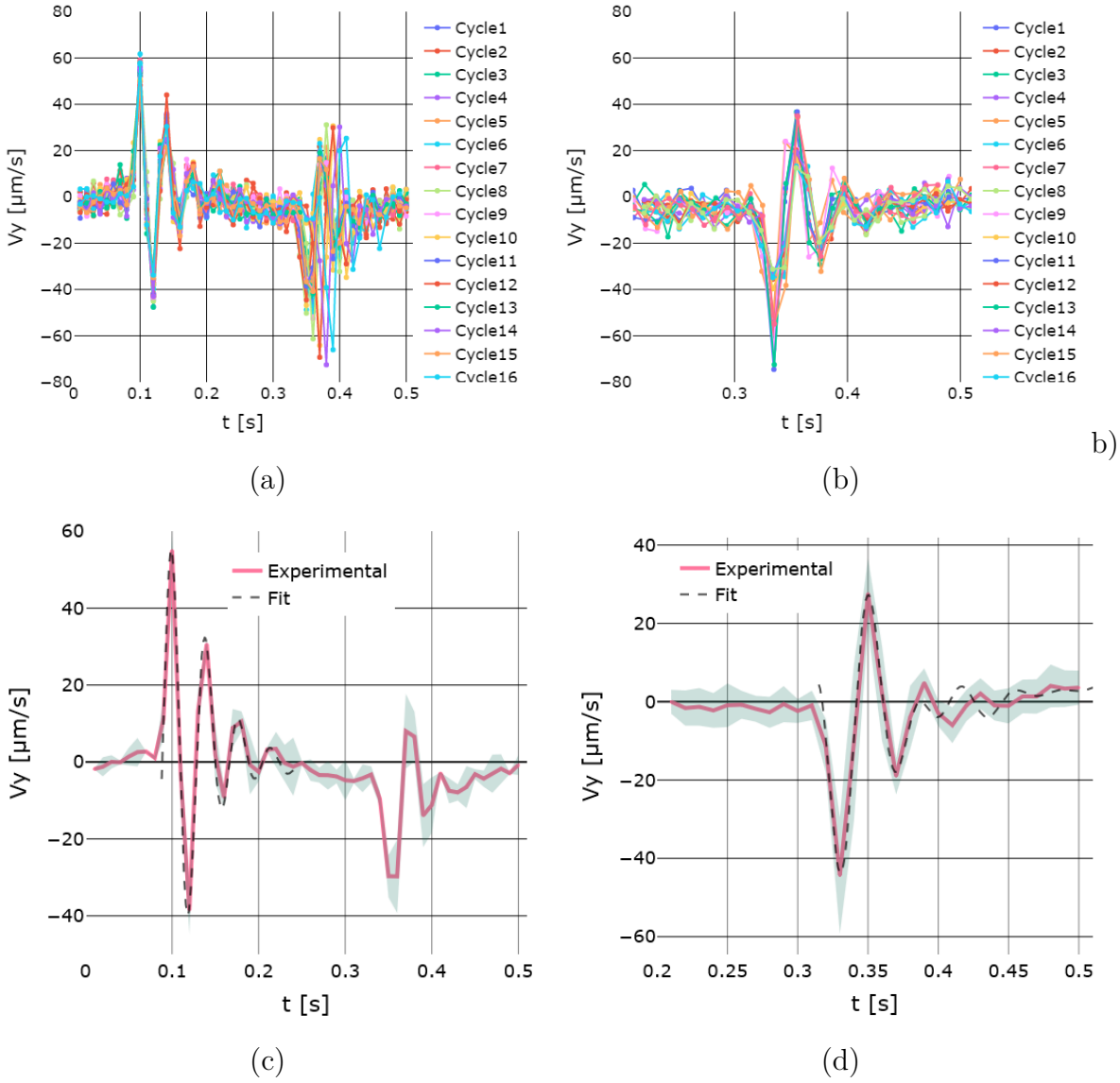

Figure 4.6: Vertical velocity of the ballasted microswimmer on one period $T = 0.5$s a) stack of 25 cycles, b) debuckling phase with shift correction c) averaged signal with a theoretical fit (dashed black line) d) averaged debuckling corrected signal with a theoretical fit (dashed black line).

y-direction on one cycle ($T = 0.5$ s). At about t=0.08s, we see the repetitive peak of the velocity. It indicates the buckling phase. It decays and then it is followed by a post-buckling oscillation for few cycles and it decays after a small duration. The shell stabilizes for about 0.1s with a constant downward velocity v_b. The second group of peaks corresponds to the debuckling phase which is also followed by an oscillation. Contrary to the buckling phase, the debuckling one does not occur exactly on the same time at each cycle. We correct this phase shift as seen in Fig. 4.6b). The correction is made such as the first minima of every cycle coincides at the same moment $t_{shift} = 0,003 \pm 0.016$s. Remarkably, by aligning only the first minima, the whole oscillations aligns as well. After that, we smooth these two curves by taking the time average over all the cycles as shown in Fig. 4.6c) and d). The gray envelop designates the error (mean ± standard deviation). The duration of every phase as well are highlighted in the following table:

Phase duration (s)	Average	Standard deviation
τ_1	0.14	0.01
τ_2	0.11	0.01
τ_3	0.14	0.02
τ_4	0.11	0.02

Table 4.1: Summary of all the duration phases

Using all the duration phases and the two sedimenting velocities v_0 and v_b, we get the bounding of the traveled sedimentation distance: $1.24\mu m/cycle < d_s < 2.08\mu m/cycle$. Finally, a bounding of the net displacement, which is the useful information that we aimed to measure: $0.55\mu m/cycle < \mathbf{d}_{net} < 1.37\mu m/cycle$ for a driving frequency $f = 2$Hz which is $\sim 1/3$ the radius of the microbubble per cycle. A mean swimming velocity can be calculated: $\underline{\bar{v}_{swim} \sim 2\ \mu\text{m/s}}$.

Post buckling and debuckling oscillations

We fit the post-buckling oscillations as well the the post-debuckling oscillations with theoretical curves as shown by the black dashed lines in Fig. 4.6c) and d). Those oscillations can be easily modeled as a free damped harmonic oscillator. The classical response of a spring and a damper under free oscillations is:

$$\xi(t) = Ae^{-\gamma t}cos(\omega t - \phi) \tag{4.16}$$

In our case, $\xi(t)$ is the vertical velocity, γ is the damping coefficient, ω is the pulsation and ϕ is the time phase. The experiment was repeated 10 times for the same frequency and amplitude, 10 movies of the ballasted microswimmer was taken and analyzed the same way. We obtain the following fitting parameters shown in Table 4.2:

The post-buckling pulsation is higher than the post-debuckling one $\omega_b > \omega_{db}$. It means that the oscillations after the re-inflation takes longer than the one after

	Buckling	Debuckling
A (μm/s)	75.34 ± 2.31	72.1 ± 6.31
ω (rad/s)	168.7 ± 2.01	159.67 ± 6.44
γ $(\mu ms)^{-1}$	23.29 ± 1.32	29.04 ± 4.81
ϕ (rad)	0.1 ± 0.01	0.1 ± 0.01

Table 4.2: Summary of the post buckling and debuckling oscillations of the ballasted microswimmer with an activation frequency $f = 2$Hz.

inflation. Interestingly, the damping has the inverse effect: $\gamma_b < \gamma_{db}$ and it means that the oscillations after buckling have higher amplitudes than the ones after debuckling. As stated in the previous chapter, only one eigenfrequency is measured which corresponds to the bending energy.

Another important remark regarding the value of the post buckling frequency is that it is higher than the one measured on a single shell in the 'near-wall' configuration. In fact, the microbubble here is confined between two spherical beads, hence the mass fluid that moves around it is smaller, which can contribute to a higher frequency while for the single microbubble, the contact is only the wall (See Chap3 Sec.3.6).

4.4 Conclusions & perspectives

We have shown throughout this chapter, how commercial UCAs (SonoVue®) as well as homemade microbubbles can swim by virtue of buckling mechanism.

We studied experimentally the effect of the elasticity of the shell material. We showed that a higher swimming effect can be produced through higher 2D compression modulus χ_{2D}.

We also studied a very rare experimental case where SonoVue® microbubble got glued to two spherical beads that do not buckle upon pressure. A swimming against gravity was shown for a net displacement of about $\sim 1/3$ the radius per cycle. Post buckling and post debuckling oscillations were also measured, and they are well fitted with a simple harmonic oscillator which provides an eigenfrequency.

It is important to note that the swimming motion is different from the translational motion than can be generated via the primary Bjerkness force [Bjerknes, 1906]. After the pioneering work of [Dayton et al., 1997] on the acoustic radiation force applied on UCAs, many studies went in this direction. In [Acconcia et al., 2018], an experimental study on the displacement of UCAs induced by these forces is done. It uses an optical tweezers to carefully select a microbubble. Ultrasonic waves are generated by a transducer that couples with the microbubbles into primary and secondary Bjerkness forces. The induced displacement is always in the same direction as the direction of propagation of the acoustic field. On the contrary, with our technique, the direction of the displacement is completely independent of the direction of the activation and it is controlled by a scalar parameter: Pressure.

5

General conclusions & Future work

Contents

5.1 Scientific contributions

The overall aim of the work described in this thesis was first to improve the characterization of ultrasound contrast agents and second to use them as microswimmers using a novel propulsion mechanism: Buckling instability.

In chapter 2, we highlighted the lack of knowledge in modeling the behaviour of UCAs through a theoretical model. The generalized model shows that including the compressibility of the shell has a huge effect on the resonance frequency and on the damping in the spherical regime. This effect provides the proposed model potentiality to understand the size dependency of the viscoelastic parameters of the shell.

In addition, the anisotropy of the lipidic nature of the shell was studied and it can contribute to a more realistic model.

In chapter 3, we successfully designed and conducted an experimental setup with a minimal material complexity to study buckling dynamics of commercial microbubbles SonoVue® as well as homemade monodisperse UCAs in two different configurations: near the wall and freely floating against gravity. We developed a triggering approach to study the intrinsic parameters of shell buckling as well as a homemade algorithm to accurately track the position of the microbubbles and their deformation in time and space.

The results validate our proposition of the anisotropy of the shell. Classical linear buckling theory fails to estimate the buckling pressure of microbubbles. We demonstrated how an apparent thickness resulting from an increase in the bending

energy can be the adequate way to describe the behaviour of bilipid membranes. Contrary to the current indirect methods, such as acoustic backscattering, buckling dynamics might be the new experimental method to study intrinsic shell properties.

Experimental results were in-line with a 3D axisymmetric numerical study which shows the robustness of the mechanism through the hysteretic shape deformation path revealed in both studies.

In chapter 4, swimming motions were studied, a net positive displacement was shown on SonoVue® UCAs and a more pronounced effect on the monodisperse microbubbles. The results suggested two populations in the swimming motion, the forward swimmers and the backward swimmers. Further research needs to be conducted to understand the reason for the formation of the two populations. Reference beads (which do not buckle) were used as a control, enabling us to show that movement through buckling was different with a statistical significance.

A fortuitous discovery of a new type of swimmer was shown, where a microbubble was glued to two other spherical beads started to sediment with gravity instead of floating. Swimming against gravity was well remarked.

In addition, we measured the rotational motion of the shells while floating through the use of a single buckling spot. Measurements of the angle difference between cycles were well understood via a Brownian rotational diffusion model.

Post-buckling oscillations were studied and well modeled with a single harmonic oscillator.

Overall, the buckling instability of UCAs can be a promising mechanism to create in-vivo friendly microswimmers for various medical use such as targeted drug and gene delivery as well as in molecular imaging.

5.2 Further work

As it was indicated at various stages throughout the thesis, there are many areas that require further investigation.

Perhaps the greatest area of uncertainty, which was discussed at several points in the thesis, is controlling the buckling direction. A way to tackle this challenge is through the fabrication of UCAs with a seeded defect, so that buckling would always arise at this spot. A second way to achieve this is by repeating the same experiment that we conducted by complete chance (the ballasted microswimmer). Attachments of several bodies show a promising way to control the buckling spot.

Exploration of different biocompatible shell materials is also essential for future work. A higher net displacement could be achieved with a material that has minimal damping. Less damping can allow faster buckling transition such as inertial effects can be expected.

Once the optimization of shell viscoelastic properties for an optimal swimming motion is done, ultrasound pressure waves can be used carefully to speed up the activation. A combination of the acoustic force radiation and the streaming effect will be added to the shell buckling which will be used in this case as extra steering in a complete 3D mode owing to its important contribution to swimming.

The ideal scenario would be to have four shells attached in a tetrahedron structure with different sizes and visco-elastic materials so that each one will buckle at a different given pressure. A full manoeuvre of this body could then be controlled with the amplitude of the medical ultrasound probe in parallel to the probe used for ultrasound imaging of the microrobot.

Appendices

A

Technical analysis

Contents

A.1 Triggering algorithm

- Step 1 : set trigger out @ 0V (to rearm the trigger first)
- Step 2 : wait 5ms
- Step 3 : if trigger in @ 5V, then go to Step 5 (if False, go to Step 4)
- Step 4 : go to Step 2 for maximum 100 times (or more)
- Step 5 : set trigger out @ 5V
- Step 6 : end

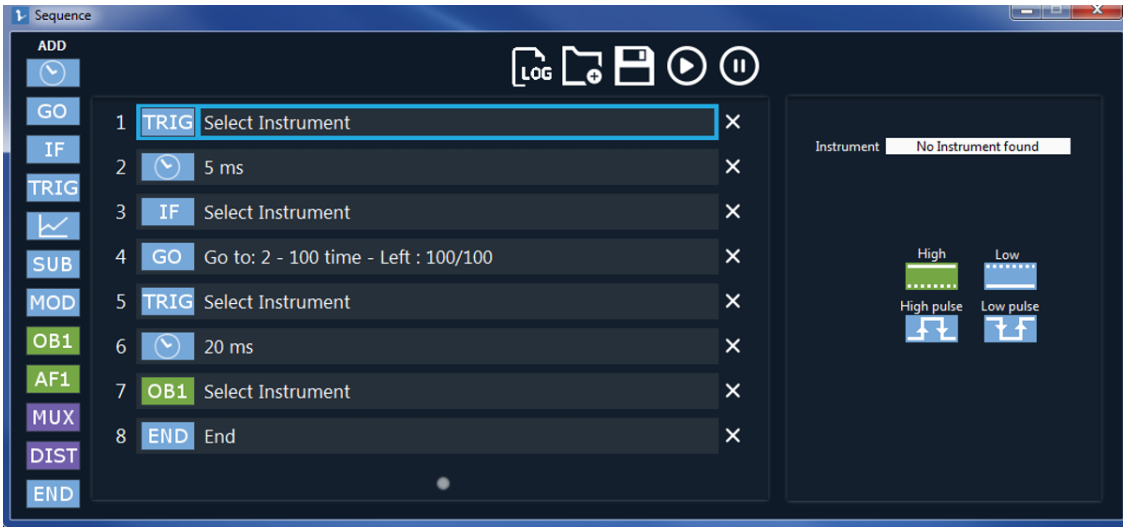

Figure A.1: Trigger algorithm on Elveflow interface

B
Theoretical model

Contents

B.1 Deformation velocities

We present here the expressions obtained for $\dot{a}$ and $\dot{b}$ by directly derivating a and b, see Sec. 2.5.1:

$$\begin{aligned}\dot{a}(t) = &\frac{R_2^2 U_2 - R_1^2 U_1}{R_3^2 - R_1^3} + \frac{U_2}{(R_2^3 - R_1^3)^2} \\ &\Big[(R_1 - R_{1e})(3R_1^2 R_2^2) - (R_2 - R_{2e})(R_2^4 + 2R_2 R_1^3)\Big] \\ &+ \frac{U_1}{(R_2^3 - R_1^3)^2} \\ &\Big[(R_2 - R_{2e})(3R_1^2 R_2^2) - (R_1 - R_{1e})(R_1^4 + 2R_1 R_2^3)\Big],\end{aligned}$$

and:

$$\begin{aligned}\dot{b}(t) = &\frac{(R_2 U_1 - R_1 U_2) R_1^2 R_2^2}{R_3^2 - R_1^3} + \frac{U_1}{(R_2^3 - R_1^3)^2} \\ &\Big[(R_1 - R_{1e})(2R_1 R_2^6 + R_1^4 R_2^3) - (R_2 - R_{2e})(3R_1^2 R_2^5)\Big] \\ &+ \frac{U_2}{(R_2^3 - R_1^3)^2} \\ &\Big[(R_2 - R_{2e})(2R_2 R_1^6 + R_2^4 R_1^3) - (R_1 - R_{1e})(3R_1^5 R_2^2)\Big].\end{aligned}$$

Bibliography

[Abou-Saleh et al., 2013] Abou-Saleh, R. H., Peyman, S. A., Critchley, K., Evans, S. D., and Thomson, N. H. (2013). Nanomechanics of lipid encapsulated microbubbles with functional coatings. *Langmuir*, 29(12):4096–4103.

[Acconcia et al., 2018] Acconcia, C. N., Wright, A., and Goertz, D. E. (2018). Translational dynamics of individual microbubbles with millisecond scale ultrasound pulses. *The Journal of the Acoustical Society of America*, 144(5):2859–2870.

[Altenbach et al., 2008] Altenbach, H., Brigadnov, I. A., and Eremeyev, V. A. (2008). Oscillations of a magneto-sensitive elastic sphere. *ZAMM-Journal of Applied Mathematics and Mechanics/Zeitschrift für Angewandte Mathematik und Mechanik: Applied Mathematics and Mechanics*, 88(6):497–506.

[Aryal et al., 2014] Aryal, M., Arvanitis, C. D., Alexander, P. M., and McDannold, N. (2014). Ultrasound-mediated blood–brain barrier disruption for targeted drug delivery in the central nervous system. *Advanced drug delivery reviews*, 72:94–109.

[Bamber, 1998] Bamber, J. C. (1998). Ultrasonic properties of tissues. *Ultrasound in medicine*, pages 57–88.

[Bao et al., 1997] Bao, S., Thrall, B. D., and Miller, D. L. (1997). Transfection of a reporter plasmid into cultured cells by sonoporation in vitro. *Ultrasound in medicine & biology*, 23(6):953–959.

[Barr et al., 2020] Barr, R. G., Huang, P., Luo, Y., Xie, X., Zheng, R., Yan, K., Jing, X., Luo, Y., Xu, H., Fei, X., et al. (2020). Contrast-enhanced ultrasound imaging of the liver: a review of the clinical evidence for sonovue and sonazoid. *Abdominal Radiology*, 45:3779–3788.

[Besant, 1859] Besant, W. H. (1859). *A Treatise on Hydrostatics and Hydrodynamics*. Deighton, Bell.

[Betzig et al., 2006] Betzig, E., Patterson, G. H., Sougrat, R., Lindwasser, O. W., Olenych, S., Bonifacino, J. S., Davidson, M. W., Lippincott-Schwartz, J., and Hess, H. F. (2006). Imaging intracellular fluorescent proteins at nanometer resolution. *Science*, 313(5793):1642–1645.

[Bjerknes, 1906] Bjerknes, V. (1906). *Fields of force: supplementary lectures, applications to meteorology; a course of lectures in mathematical physics delivered December 1 to 23, 1905*. Number 1 in 2. Columbia University Press.

[Bouakaz et al., 2005] Bouakaz, A., Versluis, M., and de Jong, N. (2005). High-speed optical observations of contrast agent destruction. *Ultrasound in medicine & biology*, 31(3):391–399.

[Brenner et al., 2002] Brenner, M. P., Hilgenfeldt, S., and Lohse, D. (2002). Single-bubble sonoluminescence. *Reviews of modern physics*, 74(2):425.

[Buchner Santos et al., 2012] Buchner Santos, E., Morris, J. K., Glynos, E., Sboros, V., and Koutsos, V. (2012). Nanomechanical properties of phospholipid microbubbles. *Langmuir*, 28(13):5753–5760.

[Budiansky and Hutchinson, 1979] Budiansky, B. and Hutchinson, J. (1979). Buckling progress and challenge, trends in solid mechanics. In *Proc. Symp. dedicated to the 65th Birthday of WT Koiter*, volume 93.

[Bunea and Taboryski, 2020] Bunea, A.-I. and Taboryski, R. (2020). Recent advances in microswimmers for biomedical applications. *Micromachines*, 11(12):1048.

[Carugo et al., 2021] Carugo, D., Browning, R. J., Iranmanesh, I., Messaoudi, W., Rademeyer, P., and Stride, E. (2021). Scaleable production of microbubbles using an ultrasound-modulated microfluidic device. *The Journal of the Acoustical Society of America*, 150(2):1577–1589.

[Caskey et al., 2011] Caskey, C. F., Hu, X., and Ferrara, K. W. (2011). Leveraging the power of ultrasound for therapeutic design and optimization. *Journal of controlled release*, 156(3):297–306.

[Chabouh et al., 2021] Chabouh, G., Dollet, B., Quilliet, C., and Coupier, G. (2021). Spherical oscillations of encapsulated microbubbles: Effect of shell compressibility and anisotropy. *The Journal of the Acoustical Society of America*, 149(2):1240–1257.

[Chatterjee and Sarkar, 2003] Chatterjee, D. and Sarkar, K. (2003). A newtonian rheological model for the interface of microbubble contrast agents. *Ultrasound Med. Biol.*, 29(12):1749–1757.

[Chavignon et al., 2021] Chavignon, A., Heiles, B., Hingot, V., Orset, C., Vivien, D., and Couture, O. (2021). 3d transcranial ultrasound localization microscopy in the rat brain with a multiplexed matrix probe. *IEEE Transactions on Biomedical Engineering*.

[Chetty et al., 2008] Chetty, K., Stride, E., Sennoga, C. A., Hajnal, J. V., and Eckersley, R. J. (2008). High-speed optical observations and simulation results of sonovue microbubbles at low-pressure insonation. *IEEE transactions on ultrasonics, ferroelectrics, and frequency control*, 55(6):1333–1342.

[Chi et al., 2020] Chi, Y., Tang, Y., Liu, H., and Yin, J. (2020). Leveraging monostable and bistable pre-curved bilayer actuators for high-performance multitask soft robots. *Advanced Materials Technologies*, 5(9):2000370.

[Chitnis et al., 2011] Chitnis, P. V., Lee, P., Mamou, J., Allen, J. S., Böhmer, M., and Ketterling, J. A. (2011). Rupture threshold characterization of polymer-shelled ultrasound contrast agents subjected to static overpressure. *Journal of applied physics*, 109(8):084906.

[Church, 1995] Church, C. C. (1995). The effects of an elastic solid surface layer on the radial pulsations of gas bubbles. *J. Ac. Soc. Am.*, 97(3):1510–1521.

[Coupier et al., 2019] Coupier, G., Djellouli, A., and Quilliet, C. (2019). Let's deflate that beach ball. *The European Physical Journal E*, 42(9):1–10.

[Coupier et al., 2008] Coupier, G., Kaoui, B., Podgorski, T., and Misbah, C. (2008). Noninertial lateral migration of vesicles in bounded poiseuille flow. *Physics of Fluids*, 20(11):111702.

[Couture et al., 2014] Couture, O., Foley, J., Kassell, N. F., Larrat, B., and Aubry, J.-F. (2014). Review of ultrasound mediated drug delivery for cancer treatment: updates from pre-clinical studies. *Transl Cancer Res*, 3(5):494–511.

[Couture et al., 2018] Couture, O., Hingot, V., Heiles, B., Muleki-Seya, P., and Tanter, M. (2018). Ultrasound localization microscopy and super-resolution: A state of the art. *IEEE transactions on ultrasonics, ferroelectrics, and frequency control*, 65(8):1304–1320.

[Crake et al., 2016] Crake, C., Owen, J., Smart, S., Coviello, C., Coussios, C.-C., Carlisle, R., and Stride, E. (2016). Enhancement and passive acoustic mapping of cavitation from fluorescently tagged magnetic resonance-visible magnetic microbubbles in vivo. *Ultrasound in medicine & biology*, 42(12):3022–3036.

[Dalenbring, 2002] Dalenbring, M. (2002). An explicit formulation of a three-dimensional material damping model with transverse isotropy. *Int. J. Sol. Struct.*, 39(1):225 – 249.

[Dash and Tamadapu, 2022] Dash, N. and Tamadapu, G. (2022). Radial dynamics of an encapsulated microbubble with interface energy. *Journal of Fluid Mechanics*, 932.

[Dayton et al., 1997] Dayton, P. A., Morgan, K. E., Klibanov, A. L., Brandenburger, G., Nightingale, K. R., and Ferrara, K. W. (1997). A preliminary evaluation of the effects of primary and secondary radiation forces on acoustic contrast agents. *IEEE transactions on ultrasonics, ferroelectrics, and frequency control*, 44(6):1264–1277.

[De Jong et al., 1994] De Jong, N., Cornet, R., and Lancee, C. (1994). Higher harmonics of vibrating gas-filled microspheres. part one: simulations. *Ultrasonics*, 32(6):447–453.

[De Jong et al., 2007] De Jong, N., Emmer, M., Chin, C. T., Bouakaz, A., Mastik, F., Lohse, D., and Versluis, M. (2007). "compression-only" behavior

of phospholipid-coated contrast bubbles. *Ultrasound in medicine & biology*, 33(4):653–656.

[De Jong et al., 2009] De Jong, N., Emmer, M., Van Wamel, A., and Versluis, M. (2009). Ultrasonic characterization of ultrasound contrast agents. *Medical & biological engineering & computing*, 47(8):861–873.

[de Jong and Hoff, 1993] de Jong, N. and Hoff, L. (1993). Ultrasound scattering properties of albunex microspheres. *Ultrasonics*, 31(3):175–181.

[de Jong et al., 1992] de Jong, N., Hoff, L., Skotland, T., and Bom, N. (1992). Absorption and scatter of encapsulated gas filled microspheres: theoretical considerations and some measurements. *Ultrasonics*, 30(2):95–103.

[Debye, 1929] Debye, P. (1929). Polar molecules dover. *Mineola, New York*.

[Degen, 2014] Degen, P. (2014). Self-propelling capsules as artificial microswimmers. *Current opinion in colloid & interface science*, 19(6):611–619.

[Desailly et al., 2013] Desailly, Y., Couture, O., Fink, M., and Tanter, M. (2013). Sono-activated ultrasound localization microscopy. *Applied Physics Letters*, 103(17):174107.

[Dijkink et al., 2006] Dijkink, R., Van Der Dennen, J., Ohl, C., and Prosperetti, A. (2006). The 'acoustic scallop': a bubble-powered actuator. *Journal of micromechanics and microengineering*, 16(8):1653.

[Djellouli et al., 2017] Djellouli, A., Marmottant, P., Djeridi, H., Quilliet, C., and Coupier, G. (2017). Buckling instability causes inertial thrust for spherical swimmers at all scales. *Physical review letters*, 119(22):224501.

[Doinikov and Dayton, 2006] Doinikov, A. A. and Dayton, P. A. (2006). Spatio-temporal dynamics of an encapsulated gas bubble in an ultrasound field. *J. Ac. Soc. Am.*, 120(2):661–669.

[Doinikov et al., 2018] Doinikov, A. A., Dollet, B., and Marmottant, P. (2018). Model for the growth and the oscillation of a cavitation bubble in a spherical liquid-filled cavity enclosed in an elastic medium. *Phys. Rev. E*, 97:013108.

[Doinikov et al., 2009] Doinikov, A. A., Haac, J. F., and Dayton, P. A. (2009). Modeling of nonlinear viscous stress in encapsulating shells of lipid-coated contrast agent microbubbles. *Ultrasonics*, 49(2):269–275.

[Doinikov and Marmottant, 2018] Doinikov, A. A. and Marmottant, P. (2018). Natural oscillations of a gas bubble in a liquid-filled cavity located in a viscoelastic medium. *J. Sound Vib.*, 420:61–72.

[Dollet et al., 2008] Dollet, B., van der Meer, S. M., Garbin, V., de Jong, N., Lohse, D., and Versluis, M. (2008). Nonspherical oscillations of ultrasound contrast agent microbubbles. *Ultrasound in medicine & biology*, 34(9):1465–1473.

[Dovstam, 1995] Dovstam, K. (1995). Augmented hooke's law in frequency domain. a three dimensional, material damping formulation. *International Journal of Solids and Structures*, 32(19):2835–2852.

[Einstein, 1906] Einstein, A. (1906). Zur theorie der brownschen bewegung. *Annalen der physik*, 324(2):371–381.

[Errico et al., 2015] Errico, C., Pierre, J., Pezet, S., Desailly, Y., Lenkei, Z., Couture, O., and Tanter, M. (2015). Ultrafast ultrasound localization microscopy for deep super-resolution vascular imaging. *Nature*, 527(7579):499–502.

[Euler, 1744] Euler, L. (1744). *Methodus inveniendi lineas curvas maximi minimive proprietate gaudentes*. apud Marcum-Michaelem Bousquet.

[Faez et al., 2011] Faez, T., Goertz, D., and De Jong, N. (2011). Characterization of definity ultrasound contrast agent at frequency range of 5-15 mhz. *Ultrasound Med. Biol.*, 37(2):338–342.

[Farutin et al., 2013] Farutin, A., Rafaï, S., Dysthe, D. K., Duperray, A., Peyla, P., and Misbah, C. (2013). Amoeboid swimming: A generic self-propulsion of cells in fluids by means of membrane deformations. *Phys. Rev. Lett.*, 111:228102.

[Fowlkes et al., 1993] Fowlkes, J., Gardner, E., Ivey, J., and Carson, P. (1993). The role of acoustic radiation force in contrast enhancement techniques using bubble-based ultrasound contrast agents. *The Journal of the Acoustical Society of America*, 93(4):2348–2348.

[Frinking et al., 2020] Frinking, P., Segers, T., Luan, Y., and Tranquart, F. (2020). Three decades of ultrasound contrast agents: a review of the past, present and future improvements. *Ultrasound in medicine & biology*, 46(4):892–908.

[Frinking et al., 2012] Frinking, P. J., Tardy, I., Théraulaz, M., Arditi, M., Powers, J., Pochon, S., and Tranquart, F. (2012). Effects of acoustic radiation force on the binding efficiency of br55, a vegfr2-specific ultrasound contrast agent. *Ultrasound in medicine & biology*, 38(8):1460–1469.

[Garbin et al., 2009] Garbin, V., Dollet, B., Overvelde, M., Cojoc, D., Di Fabrizio, E., van Wijngaarden, L., Prosperetti, A., de Jong, N., Lohse, D., and Versluis, M. (2009). History force on coated microbubbles propelled by ultrasound. *Physics of fluids*, 21(9):092003.

[Goertz et al., 2007] Goertz, D. E., de Jong, N., and van der Steen, A. F. (2007). Attenuation and size distribution measurements of definity and manipulated definity populations. *Ultrasound Med. Biol.*, 33(9):1376–1388.

[Goldberg, 1997] Goldberg, B. (1997). Ultrasound contrast agents london. *England: Dunitz*.

[Gorce et al., 2000] Gorce, J.-M., Arditi, M., and Schneider, M. (2000). Influence of bubble size distribution on the echogenicity of ultrasound contrast agents: A study of sonovue™. *Invest. Radiol.*, 35(11):661–671.

[Gramiak and Shah, 1968] Gramiak, R. and Shah, P. M. (1968). Echocardiography of the aortic root. *Invest. Radiol.*, 3(5):356–366.

[Guillot and Trivett, 2011] Guillot, F. M. and Trivett, D. H. (2011). Complete elastic characterization of viscoelastic materials by dynamic measurements of the complex bulk and young's moduli as a function of temperature and hydrostatic pressure. *J. Sound Vib.*, 330(14):3334–3351.

[Hayman, 1981] Hayman, B. (1981). Creep buckling—a general view of the phenomena. In *Creep in Structures*, pages 289–307. Springer.

[Helbert et al., 2020] Helbert, A., Gaud, E., Segers, T., Botteron, C., Frinking, P., and Jeannot, V. (2020). Monodisperse versus polydisperse ultrasound contrast agents: In vivo sensitivity and safety in rat and pig. *Ultrasound in Medicine & Biology*, 46(12):3339–3352.

[Helfield, 2019] Helfield, B. (2019). A review of phospholipid encapsulated ultrasound contrast agent microbubble physics. *Ultrasound Med. Biol.*, 45(2):282–300.

[Helfield et al., 2017] Helfield, B. L., Chen, X., Qin, B., Watkins, S. C., and Villanueva, F. S. (2017). Mechanistic insight into sonoporation with ultrasound-stimulated polymer microbubbles. *Ultrasound in medicine & biology*, 43(11):2678–2689.

[Helfield and Goertz, 2013] Helfield, B. L. and Goertz, D. E. (2013). Nonlinear resonance behavior and linear shell estimates for definity and micromarker assessed with acoustic microbubble spectroscopy. *J. Ac. Soc. Am.*, 133(2):1158–1168.

[Hell and Wichmann, 1994] Hell, S. W. and Wichmann, J. (1994). Breaking the diffraction resolution limit by stimulated emission: stimulated-emission-depletion fluorescence microscopy. *Optics letters*, 19(11):780–782.

[Hernot and Klibanov, 2008] Hernot, S. and Klibanov, A. L. (2008). Microbubbles in ultrasound-triggered drug and gene delivery. *Advanced drug delivery reviews*, 60(10):1153–1166.

[Hingot et al., 2020] Hingot, V., Brodin, C., Lebrun, F., Heiles, B., Chagnot, A., Yetim, M., Gauberti, M., Orset, C., Tanter, M., Couture, O., et al. (2020). Early ultrafast ultrasound imaging of cerebral perfusion correlates with ischemic stroke outcomes and responses to treatment in mice. *Theranostics*, 10(17):7480.

[Hoff et al., 2000] Hoff, L., Sontum, P. C., and Hovem, J. M. (2000). Oscillations of polymeric microbubbles: Effect of the encapsulating shell. *J. Ac. Soc. Am.*, 107(4):2272–2280.

[Holmes, 2019] Holmes, D. P. (2019). Elasticity and stability of shape-shifting structures. *Current opinion in colloid & interface science*, 40:118–137.

[Hutchinson, 1967] Hutchinson, J. W. (1967). Imperfection sensitivity of externally pressurized spherical shells. *ASME. J. Appl. Mech.*, 34:49–55.

[Itskov and Aksel, 2002] Itskov, M. and Aksel, N. (2002). Elastic constants and their admissible values for incompressible and slightly compressible anisotropic materials. *Acta Mech.*, 157:81–96.

[Khismatullin and Nadim, 2002] Khismatullin, D. B. and Nadim, A. (2002). Radial oscillations of encapsulated microbubbles in viscoelastic liquids. *Physics of Fluids*, 14(10):3534–3557.

[Kikuchi and Kanagawa, 2021] Kikuchi, Y. and Kanagawa, T. (2021). Nonlinear acoustic theory on ultrasound propagation in liquids containing multiple microbubbles encapsulated by a visco-elastic shell with compressibility. ***submitted***.

[Kooiman et al., 2011] Kooiman, K., Foppen-Harteveld, M., van der Steen, A. F., and de Jong, N. (2011). Sonoporation of endothelial cells by vibrating targeted microbubbles. *Journal of controlled release*, 154(1):35–41.

[Kooiman et al., 2014] Kooiman, K., Vos, H. J., Versluis, M., and de Jong, N. (2014). Acoustic behavior of microbubbles and implications for drug delivery. *Advanced drug delivery reviews*, 72:28–48.

[Koppolu et al., 2015] Koppolu, S., Chitnis, P. V., Mamou, J., Allen, J. S., and Ketterling, J. A. (2015). Correlation of rupture dynamics to the nonlinear backscatter response from polymer-shelled ultrasound contrast agents. *IEEE transactions on ultrasonics, ferroelectrics, and frequency control*, 62(3):494–501.

[Kotopoulis et al., 2013] Kotopoulis, S., Dimcevski, G., Helge Gilja, O., Hoem, D., and Postema, M. (2013). Treatment of human pancreatic cancer using combined ultrasound, microbubbles, and gemcitabine: a clinical case study. *Medical physics*, 40(7):072902.

[Kouijzer et al., 2021] Kouijzer, J. J., Lattwein, K. R., Beekers, I., Langeveld, S. A., Leon-Grooters, M., Strub, J.-M., Oliva, E., Mislin, G. L., de Jong, N., van der Steen, A. F., et al. (2021). Vancomycin-decorated microbubbles as a theranostic agent for staphylococcus aureus biofilms. *International Journal of Pharmaceutics*, 609:121154.

[Kwan and Borden, 2012] Kwan, J. J. and Borden, M. A. (2012). Lipid monolayer collapse and microbubble stability. *Advances in colloid and interface science*, 183:82–99.

[Kwan et al., 2015] Kwan, J. J., Myers, R., Coviello, C. M., Graham, S. M., Shah, A. R., Stride, E., Carlisle, R. C., and Coussios, C. C. (2015). Ultrasound-propelled nanocups for drug delivery. *small*, 11(39):5305–5314.

[Lajoinie et al., 2018] Lajoinie, G., Luan, Y., Gelderblom, E., Dollet, B., Mastik, F., Dewitte, H., Lentacker, I., de Jong, N., and Versluis, M. (2018). Non-spherical oscillations drive the ultrasound-mediated release from targeted microbubbles. *Communications Physics*, 1(1):1–9.

[Lakes and Wineman, 2006] Lakes, R. S. and Wineman, A. (2006). On poisson's ratio in linearly viscoelastic solids. *J. Elast.*, 85(1):45–63.

[Landau and Lifschitz, 1986] Landau, L. and Lifschitz, E. (1986). *Theory of Elasticity*. Elsevier Butterworth-Heinemann, Oxford, 3rd edition.

[Landau and Lifschitz, 1987] Landau, L. and Lifschitz, E. (1987). *Fluid Mechanics*. Elsevier Butterworth-Heinemann, Oxford, 2nd edition.

[Langtangen and Pedersen, 2016] Langtangen, H. P. and Pedersen, G. K. (2016). *Scaling of differential equations*. Springer International Publishing Berlin, Germany:.

[Lattwein et al., 2020] Lattwein, K. R., Shekhar, H., Kouijzer, J. J., van Wamel, W. J., Holland, C. K., and Kooiman, K. (2020). Sonobactericide: an emerging treatment strategy for bacterial infections. *Ultrasound in medicine & biology*, 46(2):193–215.

[Lee and Leith, 1989] Lee, C.-T. and Leith, D. (1989). Drag force on agglomerated spheres in creeping flow. *Journal of aerosol science*, 20(5):503–513.

[Lemaitre and Chaboche, 1994] Lemaitre, J. and Chaboche, J.-L. (1994). *Mechanics of solid materials*. Cambridge university press.

[Lempriere, 1968] Lempriere, B. M. (1968). Poisson's ratio in orthotropic materials. *AIAA Journal*, 6(11):2226–2227.

[Leong-Poi et al., 2002] Leong-Poi, H., Song, J., Rim, S.-J., Christiansen, J., Kaul, S., and Lindner, J. R. (2002). Influence of microbubble shell properties on ultrasound signal: Implications for low-power perfusion imaging. *Journal of the American Society of Echocardiography*, 15(10):1269–1276.

[Levin et al., 2016] Levin, A., Michaels, T. C., Adler-Abramovich, L., Mason, T. O., Mueller, T., Zhang, B., Mahadevan, L., Gazit, E., and Knowles, T. P. (2016). Elastic instability-mediated actuation by a supra-molecular polymer. *Nature Physics*, 12(10):926–930.

[Li et al., 2013] Li, Q., Matula, T. J., Tu, J., Guo, X., and Zhang, D. (2013). Modeling complicated rheological behaviors in encapsulating shells of lipid-coated microbubbles accounting for nonlinear changes of both shell viscosity and elasticity. *Physics Med. Biol.*, 58(4):985.

[Lighthill, 1978] Lighthill, J. (1978). Acoustic streaming. *Journal of sound and vibration*, 61(3):391–418.

[Linn et al., 2013] Linn, J., Lang, H., and Tuganov, A. (2013). Derivation of a viscoelastic constitutive model of kelvin-voigt type for cosserat rods. *Mech. Sci.*, 4:79–96.

[Llacer-Wintle et al., 2021] Llacer-Wintle, J., Rivas-Dapena, A., Chen, X.-Z., Pellicer, E., Nelson, B. J., Puigmartí-Luis, J., and Pané, S. (2021). Biodegradable small-scale swimmers for biomedical applications. *Advanced Materials*, 33(42):2102049.

[Luan et al., 2014] Luan, Y., Lajoinie, G., Gelderblom, E., Skachkov, I., van der Steen, A. F., Vos, H. J., Versluis, M., and De Jong, N. (2014). Lipid shedding from single oscillating microbubbles. *Ultrasound in medicine & biology*, 40(8):1834–1846.

[Lubarda and Chen, 2008] Lubarda, V. and Chen, M. C. (2008). On the elastic moduli and compliances of transversely isotropic and orthotropic materials. *J. Mech. Mat. Struct.*, 3:153–171.

[Lubarda and Asaro, 2014] Lubarda, V. A. and Asaro, R. J. (2014). Viscoelastic response of anisotropic biological membranes. part II: Constitutive models. *Theor. Appl. Mech.*, 41:213–231.

[Lum et al., 2016] Lum, J. S., Dove, J. D., Murray, T. W., and Borden, M. A. (2016). Single microbubble measurements of lipid monolayer viscoelastic properties for small-amplitude oscillations. *Langmuir*, 32(37):9410–9417.

[Luo and Wu, 2021] Luo, T. and Wu, M. (2021). Biologically inspired micro-robotic swimmers remotely controlled by ultrasound waves. *Lab on a Chip*, 21(21):4095–4103.

[Lytra et al., 2020] Lytra, A., Sboros, V., Giannakopoulos, A., and Pelekasis, N. (2020). Modeling atomic force microscopy and shell mechanical properties estimation of coated microbubbles. *Soft Matter*, 16(19):4661–4681.

[Mann et al., 1999] Mann, J., Ott, S., and Andersen, J. S. (1999). *Experimental study of relative, turbulent diffusion*. Risø National Laboratory.

[Marmottant et al., 2011] Marmottant, P., Bouakaz, A., Jong, N. d., and Quilliet, C. (2011). Buckling resistance of solid shell bubbles under ultrasound. *The Journal of the Acoustical Society of America*, 129(3):1231–1239.

[Marmottant and Hilgenfeldt, 2003] Marmottant, P. and Hilgenfeldt, S. (2003). Controlled vesicle deformation and lysis by single oscillating bubbles. *Nature*, 423(6936):153–156.

[Marmottant et al., 2005] Marmottant, P., van der Meer, S., Emmer, M., Versluis, M., de Jong, N., Hilgenfeldt, S., and Lohse, D. (2005). A model for large amplitude oscillations of coated bubbles accounting for buckling and rupture. *J. Ac. Soc. Am.*, 118:3499–3505.

[Memoli et al., 2018] Memoli, G., Baxter, K. O., Jones, H. G., Mingard, K. P., and Zeqiri, B. (2018). Acoustofluidic measurements on polymer-coated microbubbles: primary and secondary bjerknes forces. *Micromachines*, 9(8):404.

[Meng et al., 2021] Meng, Y., Reilly, R. M., Pezo, R. C., Trudeau, M., Sahgal, A., Singnurkar, A., Perry, J., Myrehaug, S., Pople, C. B., Davidson, B., et al. (2021). Mr-guided focused ultrasound enhances delivery of trastuzumab to her2-positive brain metastases. *Science translational medicine*, 13(615):eabj4011.

[Michelin and Llewellyn Smith, 2009] Michelin, S. and Llewellyn Smith, S. G. (2009). Resonance and propulsion performance of a heaving flexible wing. *Physics of Fluids*, 21(7):071902.

[Minnaert, 1933] Minnaert, M. (1933). Xvi. on musical air-bubbles and the sounds of running water. *The London, Edinburgh, and Dublin Philosophical Magazine and Journal of Science*, 16(104):235–248.

[Mohanty et al., 2019] Mohanty, K., Papadopoulou, V., Newsome, I. G., Shelton, S., Dayton, P. A., and Muller, M. (2019). Ultrasound multiple scattering with microbubbles can differentiate between tumor and healthy tissue in vivo. *Phys. Med. Biol.*, 64:115022.

[Mokbel et al., 2021] Mokbel, M., Djellouli, A., Quilliet, C., Aland, S., and Coupier, G. (2021). Post-buckling dynamics of spherical shells. *arXiv preprint arXiv:2104.06647*.

[Morgan et al., 2000] Morgan, K. E., Allen, J. S., Dayton, P. A., Chomas, J. E., Klibaov, A., and Ferrara, K. W. (2000). Experimental and theoretical evaluation of microbubble behavior: Effect of transmitted phase and bubble size. *IEEE trans. ultrason. ferr. frequ. control*, 47(6):1494–1509.

[Munglani et al., 2019] Munglani, G., Wittel, F. K., Vetter, R., Bianchi, F., and Herrmann, H. J. (2019). Collapse of orthotropic spherical shells. *Phys. Rev. Lett.*, 123:058002.

[Nagarkar et al., 2021] Nagarkar, A., Lee, W.-K., Preston, D. J., Nemitz, M. P., Deng, N.-N., Whitesides, G. M., and Mahadevan, L. (2021). Elastic-instability–enabled locomotion. *Proceedings of the National Academy of Sciences*, 118(8).

[Owen et al., 2021] Owen, J., Logan, K., Nesbitt, H., Able, S., Vasilyeva, A., Bluemke, E., Kersemans, V., Smart, S., Vallis, K. A., McHale, A. P., et al. (2021). Orally administered oxygen nanobubbles enhance tumor response to sonodynamic therapy. *Nano Select*.

[Owen et al., 2015] Owen, J., Rademeyer, P., Chung, D., Cheng, Q., Holroyd, D., Coussios, C., Friend, P., Pankhurst, Q. A., and Stride, E. (2015). Magnetic targeting of microbubbles against physiologically relevant flow conditions. *Interface focus*, 5(5):20150001.

[Pacia et al., 2022] Pacia, C., Yuan, J., Yue, Y., Xu, L., Nazeri, A., Desai, R., Gach, H. M., Wang, X., Talcott, M., Chaudhuri, A., et al. (2022). Sonobiopsy for minimally invasive, spatiotemporally-controlled, and sensitive detection of glioblastoma-derived circulating tumor dna. *Theranostics*.

[Pal et al., 2021] Pal, A., Restrepo, V., Goswami, D., and Martinez, R. V. (2021). Exploiting mechanical instabilities in soft robotics: Control, sensing, and actuation. *Advanced Materials*, 33(19):2006939.

[Parrales et al., 2014] Parrales, M. A., Fernandez, J. M., Perez-Saborid, M., Kopechek, J. A., and Porter, T. M. (2014). Acoustic characterization of monodisperse lipid-coated microbubbles: Relationship between size and shell viscoelastic properties. *The Journal of the Acoustical Society of America*, 136(3):1077–1084.

[Paul et al., 2010] Paul, S., Katiyar, A., Sarkar, K., Chatterjee, D., Shi, W. T., and Forsberg, F. (2010). Material characterization of the encapsulation of an ultrasound contrast microbubble and its subharmonic response: Strain-softening interfacial elasticity model. *The Journal of the Acoustical Society of America*, 127(6):3846–3857.

[Paul et al., 2013] Paul, S., Russakow, D., Rodgers, T., Sarkar, K., Cochran, M., and Wheatley, M. A. (2013). Determination of the interfacial rheological properties of a poly (DL-lactic acid)-encapsulated contrast agent using in vitro attenuation and scattering. *Ultrasound Med. Biol.*, 39(7):1277–1291.

[Pitois et al., 2015] Pitois, O., Buisson, M., and Chateau, X. (2015). On the collapse pressure of armored bubbles and drops. *Eur. Phys. J. E*, 38(5):48.

[Plesset and Prosperetti, 1977] Plesset, M. S. and Prosperetti, A. (1977). Bubble dynamics and cavitation. *Ann. Rev. Fluid Mech.*, 9(1):145–185.

[Pritz, 2009] Pritz, T. (2009). Relation of bulk to shear loss factor of solid viscoelastic materials. *Journal of sound and vibration*, 324(3-5):514–519.

[Prosperetti, 1987] Prosperetti, A. (1987). The equation of bubble dynamics in a compressible liquid. *The Physics of fluids*, 30(11):3626–3628.

[Purcell, 1977] Purcell, E. M. (1977). Life at low reynolds number. *Am. J. Phys.*, 45:3–11.

[Quemeneur et al., 2012] Quemeneur, F., Quilliet, C., Faivre, M., Viallat, A., and Pépin-Donat, B. (2012). Gel phase vesicles buckle into specific shapes. *Physical review letters*, 108(10):108303.

[Quilliet, 2012] Quilliet, C. (2012). Numerical deflation of beach balls with various poisson's ratios: from sphere to bowl's shape. *Eur. Phys. J. E*, 35:48.

[Rayleigh, 1917] Rayleigh, L. (1917). Viii. on the pressure developed in a liquid during the collapse of a spherical cavity. *The London, Edinburgh, and Dublin Philosophical Magazine and Journal of Science*, 34(200):94–98.

[Reis, 2015] Reis, P. M. (2015). A perspective on the revival of structural (in) stability with novel opportunities for function: from buckliphobia to buckliphilia. *Journal of Applied Mechanics*, 82(11):111001.

[Renaud et al., 2015] Renaud, G., Bosch, J. G., van der Steen, A. F., and de Jong, N. (2015). Dynamic acousto-elastic testing applied to a highly dispersive medium and evidence of shell buckling of lipid-coated gas microbubbles. *The Journal of the Acoustical Society of America*, 138(5):2668–2677.

[Reynolds, 1883] Reynolds, O. (1883). Xxix. an experimental investigation of the circumstances which determine whether the motion of water shall be direct or sinuous, and of the law of resistance in parallel channels. *Philosophical Transactions of the Royal society of London*, 1(174):935–982.

[Richardson, 1913] Richardson, L. F. (1913). Apparatus for warning a ship at sea of its nearness to large objects wholly or partially under water. *British Patent Specification*, 11125:27.

[Rychak et al., 2007] Rychak, J. J., Klibanov, A. L., Ley, K. F., and Hossack, J. A. (2007). Enhanced targeting of ultrasound contrast agents using acoustic radiation force. *Ultrasound in medicine & biology*, 33(7):1132–1139.

[Sarkar et al., 2005] Sarkar, K., Shi, W. T., Chatterjee, D., and Forsberg, F. (2005). Characterization of ultrasound contrast microbubbles using in vitro experiments and viscous and viscoelastic interface models for encapsulation. *J. Ac. Soc. Am.*, 118(1):539–550.

[Segers et al., 2016] Segers, T., De Rond, L., De Jong, N., Borden, M., and Versluis, M. (2016). Stability of monodisperse phospholipid-coated microbubbles formed by flow-focusing at high production rates. *Langmuir*, 32(16):3937–3944.

[Segers et al., 2020] Segers, T., Gaud, E., Casqueiro, G., Lassus, A., Versluis, M., and Frinking, P. (2020). Foam-free monodisperse lipid-coated ultrasound contrast agent synthesis by flow-focusing through multi-gas-component microbubble stabilization. *Applied physics letters*, 116(17):173701.

[Segers et al., 2018] Segers, T., Gaud, E., Versluis, M., and Frinking, P. (2018). High-precision acoustic measurements of the nonlinear dilatational elasticity of phospholipid coated monodisperse microbubbles. *Soft matter*, 14(47):9550–9561.

[Shafi et al., 2019] Shafi, A. S., McClements, J., Albaijan, I., Abou-Saleh, R. H., Moran, C., and Koutsos, V. (2019). Probing phospholipid microbubbles by atomic force microscopy to quantify bubble mechanics and nanostructural shell properties. *Colloids Surf. B″*, 181:506–515.

[Shekhar et al., 2018] Shekhar, H., Smith, N. J., Raymond, J. L., and Holland, C. K. (2018). Effect of temperature on the size distribution, shell properties, and stability of definity®. *Ultrasound in medicine & biology*, 44(2):434–446.

[Sieber et al., 2019] Sieber, J., Hutchinson, J. W., and Thompson, J. M. T. (2019). Nonlinear dynamics of spherical shells buckling under step pressure. *Proceedings of the Royal Society A*, 475(2223):20180884.

[Sijl et al., 2011] Sijl, J., Vos, H. J., Rozendal, T., de Jong, N., Lohse, D., and Versluis, M. (2011). Combined optical and acoustical detection of single microbubble dynamics. *J. Ac. Soc. Am.*, 130(5):3271–3281.

[Sojahrood et al., 2021] Sojahrood, A., Haghi, H., Porter, T., Karshafian, R., and Kolios, M. (2021). Experimental and numerical evidence of intensified nonlinearity at the micro and nano scale: The lipid coated acoustic bubble. *arXiv preprint arXiv:2102.12532*.

[Soysal et al., 2021] Soysal, U., Azevedo, P. N., Bureau, F., Aubry, A., Carvalho, M. S., Pessoa, A. C., De la Torre, L. G., Couture, O., Tourin, A., Fink, M., et al. (2021). Freeze-dried microfluidic monodisperse microbubbles as a new generation of ultrasound contrast agents. *arXiv preprint arXiv:2108.03093*.

[SP, 1969] SP, N. (1969). 8032, buckling of thin-walled doubly curved shells. *NASA MSFC library*, pages 1–32.

[Stein-Montalvo et al., 2021] Stein-Montalvo, L., Holmes, D. P., and Coupier, G. (2021). Delayed buckling of spherical shells due to viscoelastic knockdown of the critical load. *arXiv preprint arXiv:2104.02554*.

[Stokes, 1850] Stokes, G. (1850). On the effect of internal friction of fluids on the motion of pendulums. *Trans. Camb. phi1. S0c*, 9(8):106.

[Stokes, 1856] Stokes, G. (1856). Volume the ninth. *Trans. Cambridge Philos. Soc*, 9(5).

[Stride et al., 2020] Stride, E., Segers, T., Lajoinie, G., Cherkaoui, S., Bettinger, T., Versluis, M., and Borden, M. (2020). Microbubble agents: New directions. *Ultrasound in medicine & biology*, 46(6):1326–1343.

[Strutt, 1877] Strutt, J. W. (1877). *The theory of sound*, volume 1. Courier Corporation.

[Supponen et al., 2020] Supponen, O., Upadhyay, A., Lum, J., Guidi, F., Murray, T., Vos, H. J., Tortoli, P., and Borden, M. (2020). The effect of size range on ultrasound-induced translations in microbubble populations. *The Journal of the Acoustical Society of America*, 147(5):3236–3247.

[Tanter and Fink, 2014] Tanter, M. and Fink, M. (2014). Ultrafast imaging in biomedical ultrasound. *IEEE transactions on ultrasonics, ferroelectrics, and frequency control*, 61(1):102–119.

[Thomas and Borden, 2017] Thomas, A. N. and Borden, M. A. (2017). Hydrostatic pressurization of lung surfactant microbubbles: Observation of a strain-rate dependent elasticity. *Langmuir*, 33(47):13699–13707.

[Thompson and Kelvin, 1865] Thompson, W. and Kelvin, L. (1865). On the elasticity and viscosity of metals. *Proc. Roy. Soc. London A*, 14(289-297):1.

[Tschoegl et al., 2002] Tschoegl, N., Knauss, W. G., and Emri, I. (2002). Poisson's ratio in linear viscoelasticity – a critical review. *Mechanics of Time-Dependent Materials*, 6:3.

[Tsiglifis and Pelekasis, 2008] Tsiglifis, K. and Pelekasis, N. A. (2008). Nonlinear radial oscillations of encapsulated microbubbles subject to ultrasound: The effect of membrane constitutive law. *J. Ac. Soc. Am.*, 123(6):4059–4070.

[Tu et al., 2009] Tu, J., Guan, J., Qiu, Y., and Matula, T. J. (2009). Estimating the shell parameters of sonovue® microbubbles using light scattering. *J. Ac. Soc. Am.*, 126(6):2954–2962.

[Tu et al., 2011] Tu, J., Swalwell, J. E., Giraud, D., Cui, W., Chen, W., and Matula, T. J. (2011). Microbubble sizing and shell characterization using flow cytometry. *IEEE trans. ultrason. ferr. frequ. control*, 58(5):955–963.

[van der Meer et al., 2007] van der Meer, S. M., Dollet, B., Voormolen, M. M., Chin, C. T., Bouakaz, A., de Jong, N., Versluis, M., and Lohse, D. (2007). Microbubble spectroscopy of ultrasound contrast agents. *J. Ac. Soc. Am.*, 121(1):648–656.

[Van Elburg et al., 2021] Van Elburg, B., Collado-Lara, G., Bruggert, G.-W., Segers, T., Versluis, M., and Lajoinie, G. (2021). Feedback-controlled microbubble generator producing one million monodisperse bubbles per second. *Review of Scientific Instruments*, 92(3):035110.

[van Rooij et al., 2015] van Rooij, T., Luan, Y., Renaud, G., van der Steen, A. F., Versluis, M., de Jong, N., and Kooiman, K. (2015). Non-linear response and viscoelastic properties of lipid-coated microbubbles: DSPC versus DPPC. *Ultrasound in medicine & biology*, 41(5):1432–1445.

[Versluis et al., 2020] Versluis, M., Stride, E., Lajoinie, G., Dollet, B., and Segers, T. (2020). Ultrasound contrast agent modeling: a review. *Ultrasound in medicine & biology*, 46(9):2117–2144.

[Vincent and Marmottant, 2017] Vincent, O. and Marmottant, P. (2017). On the statics and dynamics of fully confined bubbles. *J. Fluid Mech.*, 827:194–224.

[Voigt, 1892] Voigt, W. (1892). Ueber innere reibung fester körper, insbesondere der metalle. *Annalen der Physik*, 283(12):671–693.

[von Ende et al., 2011] von Ende, S., Lion, A., and Lammering, R. (2011). On the thermodynamically consistent fractional wave equation for viscoelastic solids. *Acta Mech.*, 221:1–10.

[Vos et al., 2007] Vos, H. J., Guidi, F., Boni, E., and Tortoli, P. (2007). Method for microbubble characterization using primary radiation force. *IEEE transactions on ultrasonics, ferroelectrics, and frequency control*, 54(7):1333–1345.

[Wang, 2017] Wang, Q. X. (2017). Oscillation of a bubble in a liquid confined in an elastic solid. *Phys. Fluids*, 29:072101.

[Yan et al., 2021] Yan, D., Pezzulla, M., Cruveiller, L., Abbasi, A., and Reis, P. M. (2021). Magneto-active elastic shells with tunable buckling strength. *Nature communications*, 12(1):1–9.

[Yang et al., 2016] Yang, D., Verma, M. S., So, J.-H., Mosadegh, B., Keplinger, C., Lee, B., Khashai, F., Lossner, E., Suo, Z., and Whitesides, G. M. (2016). Buckling pneumatic linear actuators inspired by muscle. *Advanced Materials Technologies*, 1(3):1600055.

[Yoo et al., 2022] Yoo, J., Kim, H., Kim, Y., Lim, H. G., and Kim, H. H. (2022). Collapse pressure measurement of single hollow glass microsphere using single-beam acoustic tweezer. *Ultrasonics Sonochemistry*, 82:105844.

[Zoelly, 1915] Zoelly, R. (1915). *Ueber ein Knickungsproblem an der Kugelschale*. Buchdr. Zürcher & Furrer.